

REPORT DOCUMENTATION PAGE

Form Approved
OMB No. 0704-0188

The public reporting burden for this collection of information is estimated to average 1 hour per response, including the time for reviewing instructions, searching existing data sources, gathering and maintaining the data needed, and completing and reviewing the collection of information. Send comments regarding this burden estimate or any other aspect of this collection of information, including suggestions for reducing the burden, to Department of Defense, Washington Headquarters Services, Directorate for Information Operations and Reports (0704-0188), 1215 Jefferson Davis Highway, Suite 1204, Arlington, VA 22202-4302. Respondents should be aware that notwithstanding any other provision of law, no person shall be subject to any penalty for failing to comply with a collection of information if it does not display a currently valid OMB control number.

PLEASE DO NOT RETURN YOUR FORM TO THE ABOVE ADDRESS.

1. REPORT DATE (DD-MM-YYYY) 6/Sep/2001	2. REPORT TYPE THESIS	3. DATES COVERED (From - To)		
4. TITLE AND SUBTITLE NOVEL QUASO-PHASE-MATCHED DEVICES IN PERIODICALLY POLE LITHIUM NOBATE		5a. CONTRACT NUMBER		
		5b. GRANT NUMBER		
		5c. PROGRAM ELEMENT NUMBER		
6. AUTHOR(S) CAPT RUSSELL STEPHEN M		5d. PROJECT NUMBER		
		5e. TASK NUMBER		
		5f. WORK UNIT NUMBER		
7. PERFORMING ORGANIZATION NAME(S) AND ADDRESS(ES) UNIVERSITY OF DAYTON			8. PERFORMING ORGANIZATION REPORT NUMBER CI01-219	
9. SPONSORING/MONITORING AGENCY NAME(S) AND ADDRESS(ES) THE DEPARTMENT OF THE AIR FORCE AFIT/CIA, BLDG 125 2950 P STREET WPAFB OH 45433			10. SPONSOR/MONITOR'S ACRONYM(S)	
			11. SPONSOR/MONITOR'S REPORT NUMBER(S)	
12. DISTRIBUTION/AVAILABILITY STATEMENT Unlimited distribution In Accordance With AFI 35-205/AFIT Sup 1				
13. SUPPLEMENTARY NOTES				
14. ABSTRACT				
DISTRIBUTION STATEMENT A Approved for Public Release Distribution Unlimited			20011017 009	
15. SUBJECT TERMS				
16. SECURITY CLASSIFICATION OF: a. REPORT		17. LIMITATION OF ABSTRACT	18. NUMBER OF PAGES 93	19a. NAME OF RESPONSIBLE PERSON 19b. TELEPHONE NUMBER (Include area code)

ABSTRACT

The ability to engineer novel quasi-phase-matched (QPM) structures in bulk periodically poled ferroelectric crystals has led to the development of a wide variety of innovative QPM devices. Lithium niobate has been the material of choice in many of these devices due to its large nonlinear coefficient ($d_{33} \sim 27 \text{ pm/V}$), low cost, and wide availability. However, its large coercive field ($\sim 21 \text{ kV/mm}$) has limited fabrication of periodically poled lithium niobate (PPLN) samples to a maximum thickness of $\sim 1 \text{ mm}$. This crystal aperture limitation combined with the low damage fluence of lithium niobate has restricted pulsed PPLN systems to low energy operation. In this thesis, we circumvent these limitations through innovative QPM grating designs and pumping schemes.

In this work we report the design, fabrication, and demonstration of three novel PPLN devices. The first device generated broadband mid-infrared radiation by using highly elliptical beams to pump PPLN crystals with a fan-out grating design. The signal and idler beams were spatially and angularly chirped while covering spectral bands as large as 3900 cm^{-1} . The endfaces of the crystals were polished plane-parallel to force the system to operate in a monolithic optical parametric oscillator configuration. The second device used stacks of segmented multi-grating PPLN crystals to produce large signal energies with excellent beam quality. Signal energies as high as 33 mJ were generated in uncoated lithium niobate. In pursuit of the design for this system, we also explored several other unique QPM structures. The final device reported in this thesis is a widely tunable two-frequency injection-seeded optical parametric generator (OPG). In this two-stage system the output from the first stage was filtered to generate two narrow spectral lines. These lines were then used to seed the OPG process in the second stage. The resulting output was two narrow spectral lines that could each be tuned across the entire gain bandwidth of the system. Although this source has many potential applications, our intention is to use it for differential absorption lidar (DIAL) measurements and to drive THz-wave generation through difference frequency mixing in a nonlinear medium.

**Novel Quasi-Phase-Matched Devices in
Periodically Poled Lithium Niobate**

Thesis
Submitted to

Graduate Engineering & Research
School of Engineering

UNIVERSITY OF DAYTON

In Partial Fulfillment of the Requirements for
The Degree
Doctor of Philosophy in Electro-Optics

by
Stephen Michael Russell

UNIVERSITY OF DAYTON
Dayton, Ohio
May 2001

**THE VIEWS EXPRESSED IN THIS ARTICLE
ARE THOSE OF THE AUTHOR AND DO NOT
REFLECT THE OFFICIAL POLICY OR
POSITION OF THE UNITED STATES,
DEPARTMENT OF DEFENSE, OR THE U.S.
GOVERNMENT**

ABSTRACT

The ability to engineer novel quasi-phase-matched (QPM) structures in bulk periodically poled ferroelectric crystals has led to the development of a wide variety of innovative QPM devices. Lithium niobate has been the material of choice in many of these devices due to its large nonlinear coefficient ($d_{33} \sim 27 \text{ pm/V}$), low cost, and wide availability. However, its large coercive field ($\sim 21 \text{ kV/mm}$) has limited fabrication of periodically poled lithium niobate (PPLN) samples to a maximum thickness of $\sim 1 \text{ mm}$. This crystal aperture limitation combined with the low damage fluence of lithium niobate has restricted pulsed PPLN systems to low energy operation. In this thesis, we circumvent these limitations through innovative QPM grating designs and pumping schemes.

In this work we report the design, fabrication, and demonstration of three novel PPLN devices. The first device generated broadband mid-infrared radiation by using highly elliptical beams to pump PPLN crystals with a fan-out grating design. The signal and idler beams were spatially and angularly chirped while covering spectral bands as large as 3900 cm^{-1} . The endfaces of the crystals were polished plane-parallel to force the system to operate in a monolithic optical parametric oscillator configuration. The second device used stacks of segmented multi-grating PPLN crystals to produce large signal energies with excellent beam quality. Signal energies as high as 33 mJ were generated in uncoated lithium niobate. In pursuit of the design for this system, we also explored several other unique QPM structures. The final device reported in this thesis is a widely tunable two-frequency injection-seeded optical parametric generator (OPG). In this two-stage system the output from the first stage was filtered to generate two narrow spectral lines. These lines were then used to seed the OPG process in the second stage. The resulting output was two narrow spectral lines that could each be tuned across the entire gain bandwidth of the system. Although this source has many potential applications, our intention is to use it for differential absorption lidar (DIAL) measurements and to drive THz-wave generation through difference frequency mixing in a nonlinear medium.

ACKNOWLEDGMENTS

First and foremost, I'd like to thank God for blessing me with the opportunity to pursue my Ph.D. work here at the University of Dayton and for surrounding me with the people to make my time here a success. It probably would have been impossible to complete my research without the people listed below, and it definitely would not have been as much fun trying. For each of them I am truly thankful.

The person most responsible for getting me to graduation day is Peter Powers, who has served as my advisor and committee chair throughout my PhD studies. In addition to guiding me through three years of research and coursework, his light-hearted attitude has made this experience thoroughly enjoyable. His famous expression that "physics works" and his amazing ability to accomplish in two seconds what I've been trying to do for hours has helped me through many frustrating experiments and made the research experience all the more pleasurable. I have the utmost respect for him as an instructor, as a scientist, and as a person. I can't thank him enough for all of his time and effort.

I also owe a huge debt of gratitude to Ken Schepler from the Air Force Research Laboratory. He not only provided me with lab space, equipment, and funding to attend multiple conferences, but he also served on my advisory committee and provided invaluable guidance on the research front. Without him the experiments discussed in this thesis could not have been put together.

I'd also like to extend my thanks to Joe Haus, J. Michael O'Hare, and Leno Pedrotti for serving on my advisory committee. Despite their busy schedules, they put a lot of time and effort into reviewing my research proposal and the drafts of this manuscript. Their insightful comments and suggestions shaped the work presented in this thesis. They were even gracious enough to not bring up my conservative political views during my thesis defense!

Although Mark Missey was a PhD student when I entered the program, I learned from him just as if he was one of my professors. Despite trying to get his own thesis work completed, he took the time to teach me the poling process for lithium niobate and walked me through many theoretical discussions. Many of the experiments presented in this work were either thought of by Mark or inspired by his previous work. In addition, his friendship made life at the lab a lot of fun. The fact that he's a St. Louis Blues and St. Louis Cardinals fan merely adds to the stellar opinion I have of him.

I would be remiss not to express my deepest appreciation to the faculty and staff of the Physics and Electro-Optics Departments at the University of Dayton. Special thanks go to Karen Hardie for always making sure my paperwork was straight and turned in on time and to one of my former instructors, Vince Dominic, for sparking my interest in nonlinear optics. To the many other University of Dayton students I've had the pleasure of working with I'd also like to say thanks. Ned O'Brien, Bryce Schumm, Debra Krause, Sean Kelley, and Chris Brewer have especially helped to make this an enjoyable experience. In addition, John McCurdy and Jason McKay from the Air Force Research Lab have helped me keep my sanity.

There are a number of organizations that made it possible for me to pursue this research. Special thanks go to the Air Force Institute of Technology, the Dayton Area Graduate Studies Institute, the Air Force Research Laboratory, and the Air Force Office of Scientific Research. Without their support I wouldn't have been able to even start the program I'm about to finish.

Finally, I want to thank the most important people in my life, my family, for all of their love and support. I know they're proud of me finishing this degree, but I'm even more proud that I have the honor of calling them family. I've learned more from my parents - Charlie and Sharon, sister - Mendy, grandparents, aunts, uncles, and cousins, than I could ever learn in school. They've lived their lives in such a way that I can just watch what they do and know how I should live mine. Since June 1998 I've also had the great pleasure of coming home to my wonderful wife, Christa. My life wasn't complete until I met her. I've been in school as long as we've known each other and I can't thank her enough for tolerating the many long hours I've spent at the lab or with my nose buried in

books. I love her dearly and want her to know how much her mere presence brightens up my day. The longer I live on this earth, the more I realize how truly blessed I am to have such a wonderful family. I thank God for them every day.

Steve Russell
April 27, 2001

TABLE OF CONTENTS

APPROVAL PAGE.....	III
ABSTRACT.....	V
ACKNOWLEDGEMENTS.....	VII
TABLE OF CONTENTS.....	XI
LIST OF FIGURES	XIII
INTRODUCTION.....	1
CHAPTER 1 - THEORY OF QUASI-PHASE-MATCHING.....	5
<i>1.1 INTRODUCTION.....</i>	<i>5</i>
<i>1.2 QPM THEORY.....</i>	<i>5</i>
<i>1.3 EFFECTS OF LARGE APERTURE PUMPING SCHEMES</i>	<i>7</i>
<i>1.4 TWO-DIMENSIONAL FOURIER TRANSFORM INTERPRETATION OF QPM.....</i>	<i>11</i>
<i>1.5 SUMMARY.....</i>	<i>16</i>
CHAPTER 2 - BROADBAND MID-INFRARED GENERATION IN PPLN DEVICES.....	17
<i>2.1 INTRODUCTION.....</i>	<i>17</i>
<i>2.2 FAN GRATING CRYSTAL FABRICATION AND CHARACTERIZATION.....</i>	<i>19</i>
<i>2.3 MONOLITHICALLY POLISHED FAN GRATING PERFORMANCE</i>	<i>22</i>
<i>2.4 ELLIPTICAL PUMP EXPERIMENTAL SETUP</i>	<i>24</i>
<i>2.5 ELLIPTICALLY-PUMPED UNIFORM GRATING CRYSTAL EXPERIMENTS</i>	<i>26</i>
<i>2.6 ELLIPTICALLY-PUMPED FAN GRATING PERFORMANCE.....</i>	<i>32</i>
<i>2.7 SUMMARY.....</i>	<i>43</i>

CHAPTER 3 - ENERGY SCALING IN PPLN STACKS	45
3.1 <i>INTRODUCTION</i>	45
3.2 <i>SEGMENTED SINGLE-GRATING AND MULTI-GRATING PPLN CRYSTALS</i>	46
3.3 <i>SEEDED GRATING CRYSTALS</i>	55
3.4 <i>STACKS OF SEGMENTED MULTI-GRATING CRYSTALS</i>	59
3.5 <i>SUMMARY</i>	75
CHAPTER 4 - PPLN-BASED SOURCE FOR DIFFERENTIAL ABSORPTION LIDAR AND TUNABLE TERAHERTZ-WAVE GENERATION	77
4.1 <i>INTRODUCTION</i>	77
4.2 <i>TUNABLE TWO-FREQUENCY INJECTION-SEEDED OPG</i>	78
4.3 <i>SUMMARY</i>	84
CHAPTER 5 - CONCLUSIONS AND FUTURE DIRECTIONS	85
REFERENCES	89

LIST OF FIGURES

Figure 1.1 - Phase-matching diagram.....	8
Figure 1.2 - Illustration of signal and idler phase-matching geometries	9
Figure 1.3 - Single-pass gain vs. wavelength for optical parametric generation.....	10
Figure 1.4 - Noncollinear signal and idler angles versus signal wavelength.	11
Figure 1.5 - Area enclosed by the line integral defined in Equation 13	12
Figure 1.6 - Simple model of a 2-D HeXLN QPM structure and its Fourier transform .	14
Figure 1.7 - 2-D Fourier transform of the fan grating.	15
Figure 2.1 - Diagram of the fan grating crystal.. ..	18
Figure 2.2 - Areas of the +z and -z surfaces of the 20° fan grating after HF etch.	19
Figure 2.3 - Wavelength tuning curves for the 60-mm fan.	20
Figure 2.4 - Fan vs single grating spectral output comparisons	21
Figure 2.5 - Spectra centered at 1550 nm for fan and single grating crystals.	21
Figure 2.6 - Near field and far field signal beam produced by the fan grating crystal. ...	22
Figure 2.7 - Threshold data for 50-mm monolithic fan, 50-mm wedged fan, and 25-mm monolithic fan.....	23
Figure 2.8 - Spectral output for a 25-mm monolithic fan crystal	23
Figure 2.9 - Experimental setup for elliptical pumping experiments.....	25
Figure 2.10 - Pump beam with no crystal and after passing through PPLN crystal.....	25
Figure 2.11 - Near and far field images of the pump through a uniform grating crystal..	27
Figure 2.12 - Spectra for the two noncollinear OPG beams from an elliptically-pumped uniform grating period PPLN crystal	28
Figure 2.13 - Spectra for the collinear signal and idler OPG beams from the uniform grating crystal when the elliptical pump was apertured to less than 1 mm.	28
Figure 2.14 - Simple comparison of large aperture pumping configurations.....	29
Figure 2.15 - Visible output from elliptically-pumped uniform 29.75- μ m grating crystal	30

Figure 2.16 - Near and far field images of the pump beam through a uniform grating crystal, the signal beam for 4 mJ pump, and the signal for 12 mJ pump ...	31
Figure 2.17 - Spectral content of the two noncollinear beams from an elliptically-pumped fan grating crystal with a wedged output face.	32
Figure 2.18 - Collinear signal spectrum from an elliptically-pumped wedged fan crystal.	33
Figure 2.19 - Near and far field collinear signal beam images from the wedged fan grating crystal..	33
Figure 2.20 - Collinear signal and idler spectra for the 50-mm monolithic fan crystal ..	36
Figure 2.21 - Noncollinear output from a 50-mm monolithic fan crystal	36
Figure 2.22 - Collinear spectra from the 50-mm monolithic fan crystal at T=155°C	36
Figure 2.23 - Calculated atmospheric absorption trace.	37
Figure 2.24 - Signal output spectra for multiple pump energies	38
Figure 2.25 - Near field, far field, and far field after realignment images of the signal beam from a 50-mm monolithic fan crystal for various pump energies	39
Figure 2.26 - Near field and far field signal images from a 25-mm monolithically polished fan crystal for various pump energies.	40
Figure 2.27 - Illustration of the effect of crystal length on far field divergence properties of beams generated by parametric interactions.	41
Figure 2.28 - Output spectra of the far field signal beam versus position of a razor blade scanned across the beam.....	42
Figure 2.29 - Frequency combs generated by passing the signal through an etalon	43
Figure 3.1 - Illustration of signal propagation directions which see gain for a single grating crystal and a segmented-grating crystal	47
Figure 3.2 - Images of a segmented multi-grating crystal taken with an interferometer and with single-beam illumination.	48
Figure 3.3 - Close-up images of regions of a segmented single-grating crystal, segmented multi-grating crystal, and single grating crystal after HF etch.....	50

Figure 3.4 - Near field and far field images of the pump beam with no crystal present, through a single grating crystal, through a segmented single-grating crystal, and through a segmented multi-grating crystal.....	51
Figure 3.5 - Signal energy vs pump energy for single-grating, segmented single-grating, and segmented multi-grating crystals.	51
Figure 3.6 - Near field and far field images of the signal beam generated by a single-grating crystal, segmented single-grating crystal, and a segmented multi-grating crystal.....	52
Figure 3.7 - Near field and far field images of the signal beam generated by the segmented single-grating crystal with one grating illuminated and with multiple gratings illuminated.....	54
Figure 3.8 - Illustration of signal propagation directions which see gain for a seeded grating crystal.....	55
Figure 3.9 - Close-up images of a seeded-grating crystal with 450- μm seeder spacing and a seeded-grating crystal with 50- μm seeder spacing after HF etch.....	56
Figure 3.10 - Near field and far field images of the pump beam after propagation through a seeded grating crystal with 450- μm spaced seeders and a seeded grating crystal with 50- μm spaced seeders	56
Figure 3.11 - Near field and far field images of the signal beam produced by a seeded grating crystal with 450- μm spaced	57
Figure 3.12 - Near and far field images of the signal produced by a seeded grating crystal with the pump beam apertured to illuminate one seeder and two seeders... ..	58
Figure 3.13 - Near field and far field images of the signal beam produced by a seeded grating crystal with 50- μm spaced seeders	59
Figure 3.14 - Interferographic images of diffusion bonded and waxed PPLN stacks....	61
Figure 3.15 - Pumping schemes for PPLN stacks.	62
Figure 3.16 - Initial setup for PPLN stack experiments	63
Figure 3.17 - Picture of the initial experimental setup for the PPLN stack experiments	64
Figure 3.18 - Close-up picture of the lens array and PPLN stack	64

Figure 3.19 - Images of the pump beam at the focal plane of the cylindrical lens array and after passing through a PPLN.....	65
Figure 3.20 - Signal spectrum and idler spectrum generated by the PPLN.....	66
Figure 3.21 - Output signal energy versus pump energy for the PPLN stack in the initial experimental setup.....	66
Figure 3.22 - Near field and far field signal images produced by the stack of eight 1/2-mm thick PPLN crystals.	67
Figure 3.23 - Schematic and picture of the revised setup for PPLN stack experiments .	68
Figure 3.24 - Images from the revised setup of the pump beam at the focal plane of the cylindrical lens array and after passing through a PPLN stack	69
Figure 3.25 - Output signal energy versus pump energy for the PPLN stack for the revised experimental setup.....	69
Figure 3.26 - Picture of the SFG beam at the exit face of the crystal stack.	70
Figure 3.27 - Close-up images of the damage on the input and exit faces of the stack ..	71
Figure 3.28 - Near field signal images generated by the stack of eight 1/2-mm thick PPLN crystals when pumped in the revised setup	71
Figure 3.29 - Image of the pump beam at the location in the experimental setup where the crystal stack is placed.	72
Figure 3.30 - Output signal energy versus pump energy for the stack of five 1-mm PPLN multi-grating crystals.....	73
Figure 3.31 - Close-up images of the crystal damage on the input and exit faces of the stack of five 1-mm thick PPLN crystals.....	73
Figure 3.32 - Near field images of the signal output generated by the stack of five 1-mm thick PPLN crystals	74
Figure 4.1 - Experimental setup for the two-stage injection-seeded OPG system.....	79
Figure 4.2 - Seeded and unseeded OPG output from the injection-seeded system	80
Figure 4.3 - Modified experimental setup for the double-seeded OPG system.	80
Figure 4.4 - Spectral traces of the signal output from the double-seeded OPG.	81
Figure 4.5 - Spectral traces of the same data displayed in Figure 4.5, but re-plotted using a log scale for the spectral energy.....	83

INTRODUCTION

The use of electro-optic systems for scientific, commercial, and military applications has seen a dramatic increase in recent years. Electro-optic components already play critical roles in everything from fundamental scientific research to high-speed communications to space-based reconnaissance, and their use will likely expand throughout the foreseeable future. One high priority area for military research is the development of mid-infrared (IR) ($\sim 1\text{-}5 \mu\text{m}$) coherent radiation sources for remote sensing functions such as target designation and identification, IR countermeasures, and laser radar. These sources must be compact, efficient, high-energy, inexpensive, and in some cases broadly tunable. Solid-state lasers can meet these requirements and would seem like an obvious solution, but they are not readily available at mid-IR wavelengths. For this reason, devices based on nonlinear frequency conversion processes, quasi-phase-matched (QPM) devices in particular, present an attractive alternative.

One of the fundamental problems encountered with nonlinear optical processes is that interacting waves propagate through the nonlinear material with differing phase velocities. This phase-mismatch prevents the interacting fields from maintaining the proper relative phase relationship for efficient energy transfer. In the early 1960s, QPM was proposed as a method to phase-match nonlinear processes by periodically correcting the relative phase with a periodic modification built into the nonlinear material.^{1,2} One of the most effective modifications is to periodically invert the crystal optic axis (usually the "z"-axis), which results in a periodic change in sign for the second-order nonlinear susceptibility ($\chi^{(2)}$). For example, the earliest QPM demonstrations involved polishing individual plates of a nonlinear crystal to a precise thickness, then stacking them together with the crystal axis of each plate flipped 180° with respect to the previous plate.³⁻⁶ Although it was a successful demonstration of QPM, polishing and stacking individual

crystal plates is a time-consuming process and the resulting crystals suffer from variations in plate thickness as well as losses at the internal interfaces. These problems make crystal stacking difficult to scale to larger interaction lengths and led experimenters to prefer birefringent phase-matching⁷ over QPM until the mid-1990s. However, QPM has seen a resurgence in recent years, largely due to the development of an efficient method to fabricate bulk periodically poled nonlinear materials.

Electric field poling of lithium niobate (LiNbO_3) waveguides was first reported by Yamada *et al.* in 1994.⁸ Shortly thereafter Burns *et al.* and Myers *et al.* successfully applied the technique to bulk LiNbO_3 .^{9,10} Myers *et al.* fabricated periodically poled lithium niobate (PPLN) crystals by patterning electrodes onto single-domain lithium niobate substrates, then using the electrodes to apply a periodic electric field across the thickness of the crystal. Under the proper conditions, this field causes periodic 180° reversals of the crystal optic axis. Crystals fabricated by this method show orders of magnitude improvement in performance over those formed by polishing and stacking crystal plates. Of even greater importance, however, is that this bulk method permits large interaction lengths (>70 mm) and virtually unlimited electrode patterning options. The benefits of this fabrication method led to a late 1990s explosion of research in the area of QPM-based devices.

Lithium niobate, and specifically PPLN, has been the nonlinear material of choice for much of the recent research. Its high nonlinear coefficient ($d_{33} \sim 27 \text{ pm/V}$) makes it suitable for low threshold devices, yet it is widely available and inexpensive when compared to other nonlinear materials. Its large nonlinear coefficient is particularly significant because it allows PPLN devices to work with low power or low energy sources that would be too weak to pump birefringently phase-matched crystals. As a result, a wide variety of continuous-wave (cw) and pulsed PPLN systems have been demonstrated. Just a few examples of these systems include: widely tunable optical parametric oscillators (OPO)¹¹ and optical parametric generators (OPG),¹² efficient generation of cw green and blue light from diode-pumped solid state lasers,^{13,14} femtosecond pulse compression in chirped PPLN structures,^{15,16} and two-stage OPG/optical parametric amplifier (OPA) systems for high resolution spectroscopy.¹⁷

Although experiments with other nonlinear materials have been fewer in number than those with LiNbO_3 , QPM devices have also been demonstrated in MgO:LiNbO_3 ,¹⁸ LiTaO_3 ,¹⁹ RbTiOAsO_4 (RTA),^{20,21} KTiOPO_4 (KTP),^{22,23} KNbO_3 ,²⁴ and GaAs.²⁵

QPM devices based on PPLN show promise for remote sensing applications because they are compact, inexpensive, and have been shown to be both highly efficient²⁶ and broadly tunable¹¹ at mid-IR wavelengths. However, scaling up the energy in PPLN systems presents a problem. First, the high coercive field (21 kV/mm) for lithium niobate has limited the thickness of periodically poled samples to 1 mm, which thereby limits the PPLN crystal aperture and the dimensions of a pump beam that can pass through the crystal cleanly. Since PPLN has a low damage fluence of $\sim 3 \text{ J/cm}^2$, this has restricted pump energies for nanosecond pulses to a few millijoules for circular pump beams. Attempts to scale up pump energy by using elliptical pump beams, stacks of diffusion-bonded crystals, and special crystal coatings²⁷ have shown moderate success, but have achieved neither the energies nor beam quality desired for remote sensing applications. The primary focus of the first three chapters in this thesis is development of potential solutions to these inadequacies.

In Chapter 1, we briefly review basic QPM theory and address, from a theoretical perspective, the challenges of pumping QPM devices with large aperture beams. We also present a powerful new tool for modeling the phase-matching characteristics of two-dimensional QPM structures. Chapter 2 discusses the fabrication and demonstration of novel PPLN sources with broad spectral output, good beam quality, and relatively high (mJ level) output energies. These devices use high-energy, elliptical pump beams to exploit the phase-matching properties of PPLN crystals with a continuous fan-out grating design. The demonstration of a PPLN-based source with good beam quality and high output energy (potentially scaleable to the 100 mJ level) in the mid-IR wavelength region is the focus of Chapter 3. In this chapter we discuss the fabrication of stacks of multi-grating PPLN crystals and the use of a novel pumping scheme to illuminate the stacks.

The research covered in Chapter 4 deviates slightly from the central theme (i.e., high-energy sources) of the previous chapters, but is a logical spin-off of that research with potentially powerful civilian and military applications. This chapter addresses the

development of a PPLN-based source for generation of widely tunable terahertz-wave radiation. A tunable two-frequency injection-seeded PPLN OPG was the major focus of this effort.

Finally, Chapter 5 summarizes the work presented in this thesis and presents one of the most exciting aspects of this research - the many promising areas of research that are direct follow-ons to the work presented here. In this chapter we set the table for what we hope will be many successful research efforts in the future.

Chapter 1

Theory of Quasi-Phase-Matching

1.1 Introduction

The theory of QPM interactions in one-dimensional (1-D) periodic structures is well established and excellent discussions of QPM have previously been reported in the literature^{10,28}. In addition, several recent publications discussing 2-D QPM structures indicate the growing interest in 2-D optical parametric interactions.²⁹⁻³² In this chapter we briefly review the key aspects of 1-D and 2-D QPM theory, present the effects of pumping with large aperture beams, and introduce a method involving 2-D Fourier transforms to interpret phase-matching characteristics of complicated 2-D QPM structures such as the fan-out grating design. It should be noted that although the experimental results reported in Chapters 2 and 3 were performed specifically with PPLN, the theory discussed in this chapter applies to QPM interactions in other materials as well.

1.2 QPM Theory

For three-wave mixing in QPM devices, a pump wave of frequency ω_p propagates through a nonlinear medium and generates two waves (the signal and idler) at frequencies ω_s and ω_i according to the energy conservation relation

$$\omega_p = \omega_s + \omega_i. \quad \text{Equation 1.1}$$

Conservation of momentum similarly defines the phase-matching condition for the three waves as

$$\Delta\mathbf{k} = \mathbf{k}_p - \mathbf{k}_s - \mathbf{k}_i = 0 \quad \text{Equation 1.2}$$

where \mathbf{k}_p , \mathbf{k}_s , and \mathbf{k}_i are the wave vectors for the pump, signal, and idler, and $\Delta\mathbf{k}$ is known as the wave vector mismatch. For QPM interactions a grating vector \mathbf{k}_g plays a role in the phase-matching process and makes the phase-matching condition

$$\Delta\mathbf{k}' = \mathbf{k}_p - \mathbf{k}_s - \mathbf{k}_i - \mathbf{k}_g = \Delta\mathbf{k} - \mathbf{k}_g = 0. \quad \text{Equation 1.3}$$

The grating vector for a periodic structure is typically derived by replacing the periodic modulation of the nonlinear coefficient $d(r)$ with the phase-matched component of its Fourier series representation

$$d(\mathbf{r}) = d_{\text{eff}} \sum_{n=-\infty}^{\infty} D_n e^{i\mathbf{k}_n \cdot \mathbf{r}} \approx d_{\text{QPM}} e^{i\mathbf{k}_g \cdot \mathbf{r}} \quad \text{Equation 1.4}$$

where d_{eff} is the effective nonlinear coefficient for the same parametric process in bulk material, D_n is the amplitude of the n^{th} Fourier component of the periodic modulation, and \mathbf{k}_n is the grating vector of the n^{th} Fourier component.¹⁰ For a first order QPM interaction in a periodically poled crystal with a 50/50 duty cycle,

$$d_{\text{QPM}} = \frac{2}{\pi} d_{\text{eff}}. \quad \text{Equation 1.5}$$

To describe the evolution of the three fields as they interact, Maxwell's equations are used to derive the wave equation in nonlinear media

$$\nabla^2 \mathbf{E} - \mu_0 \epsilon \frac{\partial^2 \mathbf{E}}{\partial t^2} = \mu_0 \frac{\partial^2 \mathbf{P}^{\text{NL}}}{\partial t^2} \quad \text{Equation 1.6}$$

where \mathbf{P}^{NL} is the nonlinear polarization. We then define the total electric field as

$$\mathbf{E} = \frac{1}{2} \left(\sum_{\ell} E_{\ell} e^{i(\mathbf{k} \cdot \mathbf{r} - \omega_{\ell} t)} + c.c. \right), \quad \ell = p, s, i \quad \text{Equation 1.7}$$

where the subscripts p , s , and i correspond to the pump, signal, and idler fields respectively. Typically, the problem is reduced to one dimension at this point by assuming electric field amplitudes with no radial dependence (i.e., plane waves with amplitudes that vary only in the direction of propagation). For example, by assuming propagation in only the x-direction we can set $\partial E / \partial y = \partial E / \partial z = 0$. Then by substituting the electric fields into the wave equation and making the slowly varying amplitude approximation, the coupled wave equations for 1-D interactions are derived to be³³

$$\begin{aligned}
 \frac{\partial E_s}{\partial x} &= i \frac{\omega_s d_{QPM}}{2n_s c} E_p E_i^* e^{i\Delta k' x} \\
 \frac{\partial E_i}{\partial x} &= i \frac{\omega_i d_{QPM}}{2n_i c} E_p E_s^* e^{i\Delta k' x} \\
 \frac{\partial E_p}{\partial x} &= i \frac{\omega_p d_{QPM}}{2n_p c} E_s E_i e^{i\Delta k' x}
 \end{aligned} \tag{Equation 1.8}$$

where c is the speed of light and n is the refractive index. Note that these equations differ by a factor of 1/2 from those presented in reference 33 due to the way we initially defined the electric fields. These coupled equations are adequate to describe most 1-D QPM processes and to approximate some 2-D processes with little variation in the second dimension (e.g., slightly noncollinear processes); however, more complicated 2-D QPM structures require retention of the 2-D spatial dependence of the electric fields. In that case, we again substitute the electric fields described in Equation 1.7 into the wave equation and derive the coupled wave relations³¹

$$\begin{aligned}
 i\mathbf{k}_s \bullet \nabla E_s &= -\frac{\omega_s^2 d(r)}{2c^2} E_p E_i^* e^{i\Delta \mathbf{k} \cdot \mathbf{r}} \\
 i\mathbf{k}_i \bullet \nabla E_i &= -\frac{\omega_i^2 d(r)}{2c^2} E_p E_s^* e^{i\Delta \mathbf{k} \cdot \mathbf{r}} \\
 i\mathbf{k}_p \bullet \nabla E_p &= -\frac{\omega_p^2 d(r)}{2c^2} E_s E_i e^{i\Delta \mathbf{k} \cdot \mathbf{r}}
 \end{aligned} \tag{Equation 1.9}$$

where we have once again made the slowly varying amplitude approximation. Although these equations maintain the full three-dimensional nature of the fields, they can be simplified to consider the fields in only two dimensions for 2-D QPM structures.

1.3 Effects of Large Aperture Pumping Schemes

To examine the effects of pumping QPM devices with large aperture beams, we first consider flood illumination of a uniform grating PPLN crystal in an OPG configuration. For a given pump wavelength and grating period, there are many signal and idler pairs that can satisfy the phase-matching relationship. This is easily illustrated by drawing the wave vectors for multiple signal and idler pairs in a phase-matching diagram as shown in Figure 1.1. To satisfy the phase-matching condition, the vector addition of the signal, idler, and grating wave vectors must equal the pump wave vector.

As shown in Figure 1.1, many \mathbf{k}_s and \mathbf{k}_i geometries can satisfy this condition for a given \mathbf{k}_p and \mathbf{k}_g .

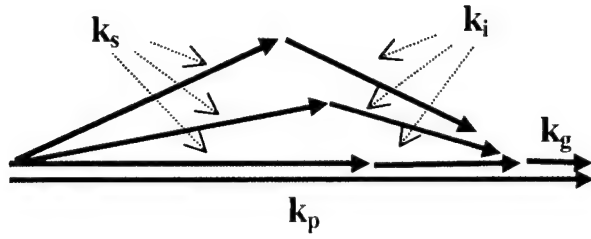


Figure 1.1 - Phase-matching diagram for collinear and various noncollinear signal and idler pairs.

Since the pump, signal, and idler waves must overlap within the crystal to interact, the transverse dimensions of the pump beam define a gain channel in the material and determine an effective interaction length for noncollinear OPG processes. For OPO operation the OPO resonator modes also play a role in defining the gain channel. For typical small diameter pump beams, this channel is small enough to permit only collinear or slightly noncollinear signal and idler pairs to see significant gain throughout the length of the crystal (see Figure 1.2). Any larger noncollinear directions would quickly propagate out of the gain channel and no longer interact with the pump beam (i.e., the effective length of the noncollinear interactions would be reduced). On the other hand, Figure 1.2 shows that pump beams with larger transverse dimensions permit both collinear processes and interactions at larger noncollinear angles to see gain for the full length of the crystal. Since the large aperture pump will allow phase-matching at multiple noncollinear angles and hence multiple wavelengths, we rely on the gain characteristics of the OPG process to predict OPG performance.

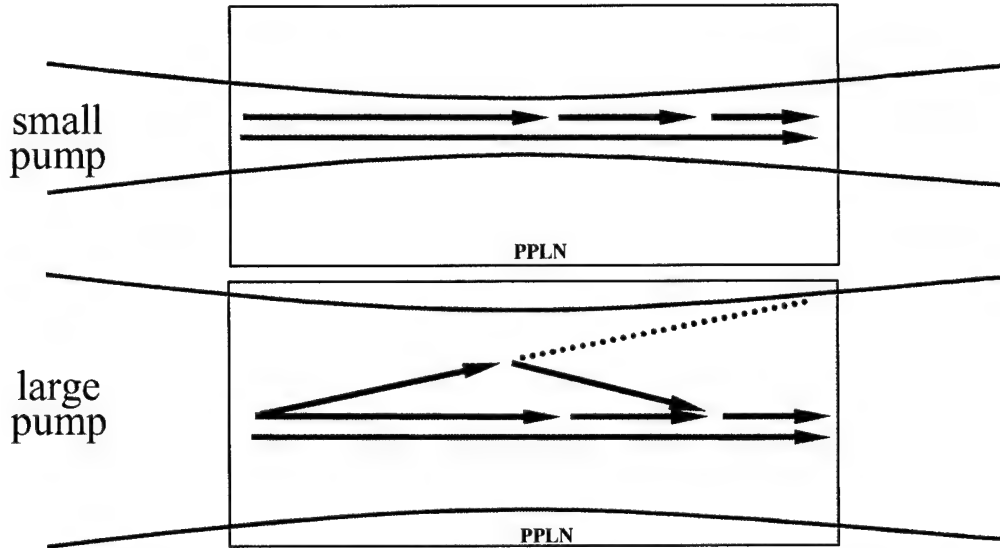


Figure 1.2 - Illustration of signal and idler phase-matching geometries allowed by pump beams with small cross sections (top) and large cross sections (bottom).

If we assume the pump and signal fields are incident on the crystal with no incident idler field, the single-pass parametric gain for the signal field in the low gain limit is given by³³

$$G(L) = \frac{|E_s(L)|^2}{|E_s(0)|^2} - 1 \approx \frac{\omega_s \omega_i d_{QPM}^2 |E_p|^2}{4n_s n_i c^2} L^2 \text{sinc}^2\left(\frac{|\Delta k'| L}{2}\right) \quad \text{Equation 1.10}$$

where L is the nonlinear interaction length. Again, due to the way we initially defined the electric fields the equation differs by a factor of 1/4 from the result presented in reference 33. This equation shows that since the signal-idler frequency product is a maximum at degeneracy (i.e., when $\omega_s = \omega_i$), the single-pass parametric gain is largest for wavelengths near degeneracy. This is illustrated in Figure 1.3. Thus, if the aperture of the pump beam is large enough not to reduce the effective length of the crystal for noncollinear processes, we expect the noncollinear directions corresponding to wavelengths near degeneracy to see the most gain and be the first to reach OPG threshold. For our purposes throughout this thesis we define OPG threshold as the point where the output energy at the signal wavelength reaches an easily detectable level of 1 μJ .

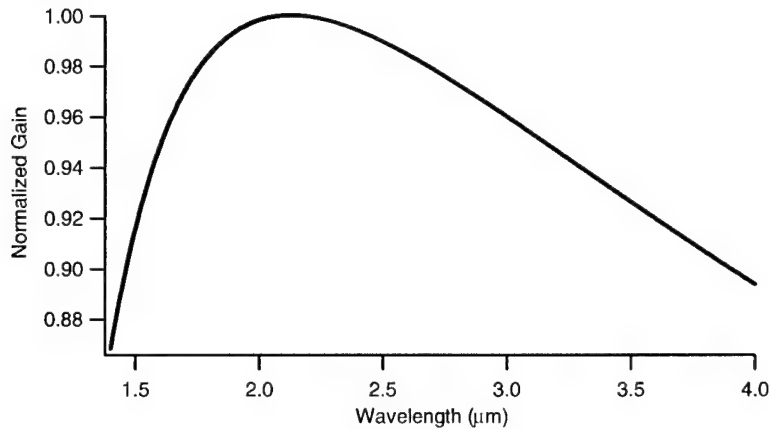


Figure 1.3 - Single-pass gain vs. wavelength for optical parametric generation.

As an example, a PPLN crystal with a grating period of 29.75 μm will phase-match in a collinear geometry for a signal wavelength of 1.525 μm when pumped at 1.064 μm with the crystal at 30°C. To make a comparison to noncollinear processes, the noncollinear phase-matching angles for other signal wavelengths are plotted in Figure 1.4. From Figure 1.4, the largest noncollinear signal direction that will phase-match (assuming no grating rotation) is $\sim 2.6^\circ$ with respect to the pump and occurs at degeneracy (2.128 μm). The largest noncollinear idler angle is $\sim 2.9^\circ$ and occurs for an idler wavelength of 2.6 μm (corresponding to a signal of 1.8 μm). Such noncollinear processes will quickly steer off of a small diameter (on the order of 300 μm or less) pump beam and thereby reduce the effective interaction length. Thus, the OPG for a small diameter pump beam is collinear and limited to a small bandwidth around the collinear signal wavelength. However, a pump beam with a large cross section will permit all wavelengths from 1.525 μm (collinear) through degeneracy to see gain for the full length of the crystal. Since the noncollinear wavelengths near degeneracy have the largest single-pass gain, we expect those wavelengths to reach OPG threshold first. This result is observed experimentally and is discussed in Chapter 2.

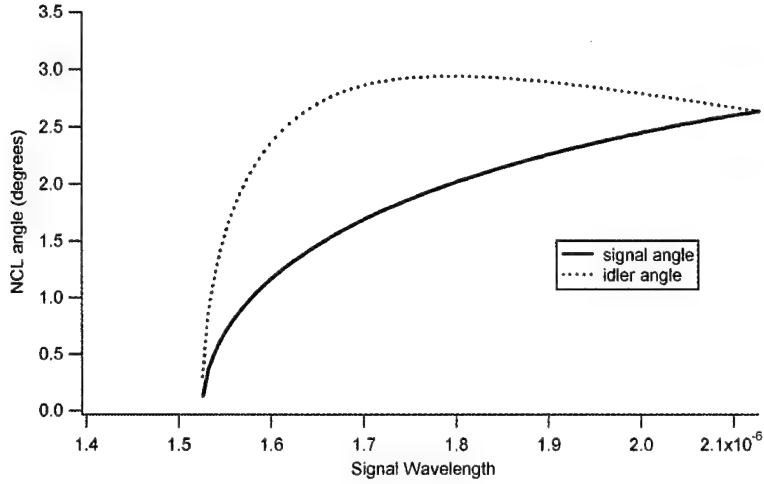


Figure 1.4 - Noncollinear signal and idler angles versus signal wavelength when phase-matched for a 1.064- μm pump and 29.75- μm grating period. Note that the maximum idler angle does not occur at the same wavelength as the maximum signal angle.

1.4 Two-dimensional Fourier Transform Interpretation of QPM

Although the single periodicity crystal considered above has a clear phase-matching picture, other more complex structures do not have such a straightforward phase-matching interpretation. To help describe the phase-matching of more general 2-D structures (e.g., the fan-out grating) we present a technique that is useful for modeling the phase-matching characteristics of 2-D QPM structures. For difference frequency generation (DFG), Equation 1.9 can be used to calculate the small-signal gain for the signal in the following way. Assuming a two-dimensional spatial dependence of the interacting fields (in the x and y directions), integrating both sides of the first part of Equation 1.9 gives

$$\iint_A \mathbf{i}\mathbf{k}_s \bullet \nabla E_s dx dy = \iint_A -\frac{\omega_s^2 d(x, y)}{2c^2} E_p E_i^* e^{i\Delta\mathbf{k}\cdot\mathbf{r}} dx dy \quad \text{Equation 1.11}$$

where $d(x, y)$ is the spatial variation of the nonlinear coefficient and A is the area over which we are integrating. Equation 1.11 can be rewritten and simplified for the two-dimensional case to give

$$\iint_A \left[ik_{s_x} \frac{\partial E_s}{\partial x} + ik_{s_y} \frac{\partial E_s}{\partial y} \right] dx dy = -\frac{\omega_s^2 E_p E_i^*}{2c^2} \iint_A d(x, y) e^{i(\Delta k_x x + \Delta k_y y)} dx dy \quad \text{Equation 1.12}$$

where the pump and idler fields are assumed to be undepleted so E_p and E_i^* can be brought outside the integral. Applying Green's theorem to convert the left side of the equation to a line integral then gives

$$\iint_A \left[ik_{s_x} \frac{\partial E_s}{\partial x} + ik_{s_y} \frac{\partial E_s}{\partial y} \right] dx dy = \oint i \left[-k_{s_y} E_s dx + k_{s_x} E_s dy \right]. \quad \text{Equation 1.13}$$

The line integral is a path that bounds the area of the integrals in Equation 1.12. A sample path for a noncollinear interaction is illustrated in Figure 1.5. The path is chosen to describe the growth of E_s in a noncollinear direction. The line integral can be evaluated by first assuming there is no signal field present along path 1 (at the input to the crystal) in Figure 1.5.

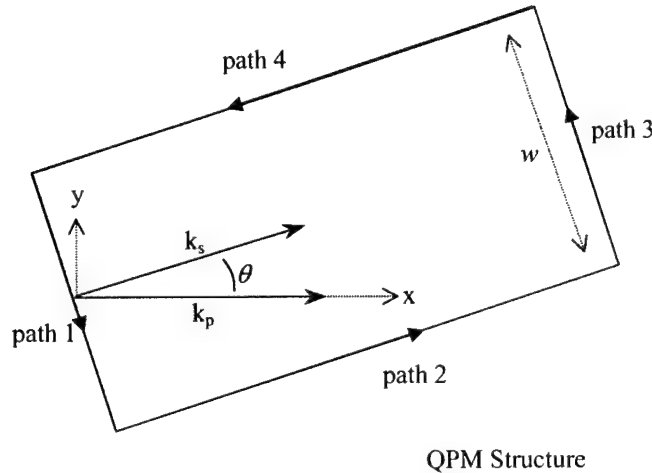


Figure 1.5 - Area enclosed by the line integral defined in Equation 1.13 for an arbitrary noncollinear signal propagation angle θ .

Assuming a plane wave interaction, the line integrals along paths 2 and 4 are equal and opposite, so they cancel each other. Hence, the line integral is reduced to evaluation along path 3. Assuming that along path 3 the amplitude of a plane wave for this noncollinear interaction is constant, the line integral then gives

$$\oint i \left[-k_{s_y} E_s dx + k_{s_x} E_s dy \right] = i w k_s E_s \quad \text{Equation 1.14}$$

where w is the width of the area bounded by the line integral for a given signal propagation direction (see Figure 1.5). Combining Equation 1.14 with Equation 1.12 gives

$$E_s(\Delta k_x, \Delta k_y) = \frac{i\omega_s E_p E_i^*}{2n_s w} \iint_A d(x, y) e^{i(\Delta k_x x + \Delta k_y y)} dx dy. \quad \text{Equation 1.15}$$

Although this integral can be directly integrated using numerical methods for any $d(x, y)$ (even aperiodic structures), the form of the integral is a 2-D Fourier transform of $d(x, y)$ into Δk -space. This is very similar to the treatment described by Fejer *et al.* for second harmonic generation (SHG) in periodic 1-D QPM devices.²⁸ By simply taking the Fourier transform of any 2-D QPM pattern, we can determine which points in Δk -space produce the largest signal field amplitudes. Unlike a single periodicity structure whose Fourier transform produces a single point in Δk -space, an arbitrary structure can have multiple points or large regions where the Fourier amplitude is appreciable. From Equation 1.3 the optimum phase-matching condition is $\Delta k = \mathbf{k}_g$. Thus, the vectors from the origin to these points or regions in Δk -space define which \mathbf{k}_g vectors are available for efficient phase-matching. This method is particularly useful for aperiodic structures where other techniques, such as those utilizing reciprocal lattice vectors,³⁰⁻³² are difficult to implement.

To validate this approach, we first looked to repeat results reported in the literature. We note that Broderick *et al.* recently demonstrated SHG in 2-D hexagonally poled lithium niobate (HeXLN) crystals with 18.05- μm periods.²⁹ Although our discussion above dealt specifically with DFG, a similar argument can be made for SHG in 2-D QPM devices. We made a simple model of the HeXLN structure (using square poled regions instead of hexagons for ease in modeling), then calculated its 2-D Fourier transform (see Figure 1.6). The Fourier transform clearly shows two strong peaks for grating vectors at angles of $\pm 30^\circ$ and two weaker peaks at $\pm 60^\circ$ with respect to the Δk_x -axis, which corresponds to the \hat{x} direction in the crystal. The \mathbf{k}_g values are the vector lengths to these peaks, which can then be used to determine the propagation directions for SHG beams. For a 1.531 μm pump beam propagating along the Δk_x -axis (as demonstrated in reference 29), this approach predicts that the grating vectors at $\pm 30^\circ$ will produce SHG beams at $\pm 1.4^\circ$ (outside the crystal) with respect to the pump beam and the grating vectors at $\pm 60^\circ$ will produce SHG beams at $\pm 4.1^\circ$. This agrees well with the

values of $\pm 1.4^\circ$ and $\pm 4.2^\circ$ that can be calculated using the reciprocal lattice vectors for the HeXLN structure.²⁹⁻³²

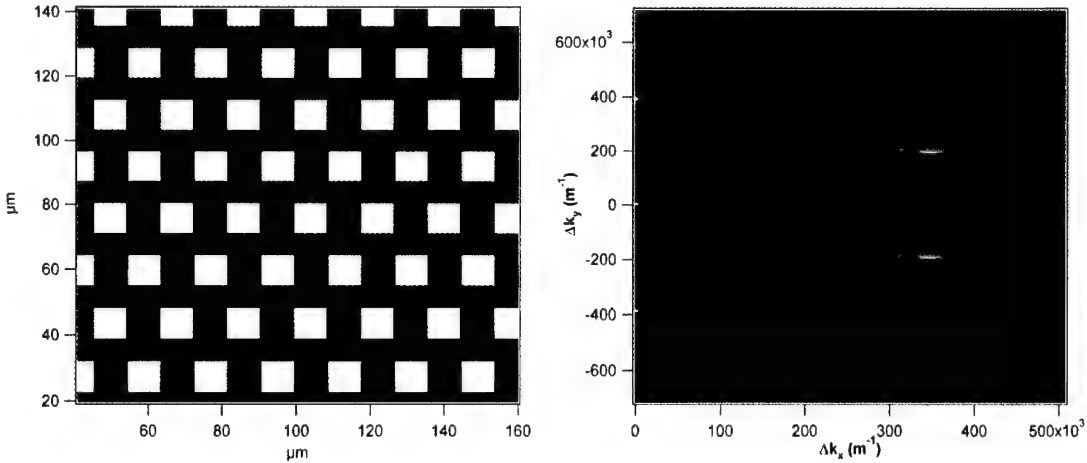


Figure 1.6 - Simple model of a 2-D HeXLN QPM structure (left) and its Fourier transform (right). In the top image, the white areas represent poled regions and the dark areas are unpoled regions. For the bottom image, the white areas are points in Δk -space with large Fourier amplitudes.

By combining the phase-matching information provided by the Fourier transform method and the effects of pumping with large aperture beams discussed above, we can develop a qualitative picture to describe the performance of 2-D QPM structures pumped by large aperture beams. We used this technique to predict the phase-matching characteristics of a fan-out grating pattern when pumped with elliptical beams. Unlike the HeXLN crystals, the reciprocal lattice picture for the fan pattern is not immediately obvious due to the lack of a clear 2-D periodicity throughout the fan. Thus, we applied the 2-D Fourier transform approach to the fan-out PPLN crystals by modeling the variation of the nonlinear coefficient in the grating structure and taking its 2-D Fourier transform (see Figure 1.7). It is immediately obvious from the Fourier transform that many \mathbf{k}_g give rise to efficient phase-matching. This is in stark contrast to the 2-D Fourier transform of a uniform grating crystal, which consists of a single peak (thus a single \mathbf{k}_g) on the Δk_x -axis.

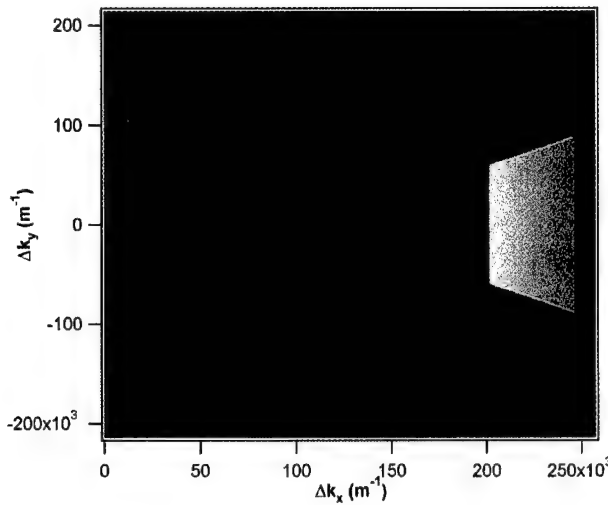


Figure 1.7 - 2-D Fourier transform of the nonlinear coefficient in a fan grating crystal with continuously varying grating periods from 25.5 μm to 31.2 μm across a 15-mm width. The white areas represent the largest Fourier amplitudes.

We can use the information provided by the Fourier transform of the fan structure to make both qualitative and specific predictions about its performance. For example, collinear interactions in the fan-out crystal can be understood by recognizing that $\Delta\mathbf{k}$ for these processes lies on the $\Delta\mathbf{k}_x$ -axis. Thus, the allowed collinear interactions are those which access \mathbf{k}_g values on this axis. From a qualitative perspective, since there is a continuous range of \mathbf{k}_g on the $\Delta\mathbf{k}_x$ -axis in Figure 1.7 we expect to be able to generate a continuous range of collinear signal and idler wavelengths. Specifically, by substituting these \mathbf{k}_g values into Equation 1.3 and solving for the signal wavelength, we predict the ability to generate collinear signal wavelengths from 1.37 μm to 2.128 μm (degeneracy) for a 1.064 μm pump at 155°C. This corresponds to idler wavelengths of 4.76 μm through degeneracy (again assuming collinear operation). These qualitative and specific predictions for the fan grating crystal are confirmed experimentally for a small diameter pump and elliptical pump operation Chapter 2.

Noncollinear interactions in the fan structure are more complex since even \mathbf{k}_g points on the $\Delta\mathbf{k}_x$ -axis can be accessed by multiple noncollinear processes (see Figure 1.1). Hence, the phase-matching efficiency is the same for both collinear and noncollinear interactions accessing the same \mathbf{k}_g . Furthermore, because there is a continuous range of noncollinear \mathbf{k}_g vectors with strong Fourier amplitudes, other noncollinear interactions

will have similar phase-matching efficiencies. For these reasons, if collinear operation is preferred by the user, a method to encourage the desired collinear operation must be employed. One obvious way to accomplish this is to set up an OPO cavity that will encourage collinear oscillation. Results presented in Chapter 2 confirm this qualitative description.

The 2-D Fourier transform method is most useful for complicated 2-D QPM structures that are not easily analyzed with standard techniques. Although both the fan-out grating PPLN crystals and the HeXLN crystals discussed above can be largely evaluated by other methods, they provide examples of the utility of the Fourier transform technique.

1.5 Summary

We have provided a brief review of basic QPM theory and expanded the theory to include the effects of pumping single-pass OPG devices with large aperture beams. The expanded theory predicts that such devices prefer to operate at wavelengths near degeneracy when pumped with large diameter beams. Therefore, for crystals not designed to phase-match at degeneracy in a collinear geometry, noncollinear signal and idler propagation directions will be preferred. If collinear operation is desired in such cases, a method to encourage collinear signal and idler generation must be employed.

We have also presented a method to analyze the phase-matching characteristics of 2-D QPM structures by taking the 2-D Fourier transform of the variation in the nonlinear coefficient traced out by the grating pattern. The Fourier transform generates a 2-D map of available grating vectors in $\Delta\mathbf{k}$ (wave vector mismatch) space. These grating vectors can then be used to determine the phase-matching characteristics of various signal and idler pairs for a given pump beam. The phase-matching conditions predicted by this method agree with those predicted by other techniques and are consistent with experimental results reported in the literature. This method should be particularly effective for complicated aperiodic 2-D structures that would be difficult to analyze using other techniques.

Chapter 2

Broadband Mid-Infrared Generation in PPLN Devices

2.1 Introduction

The ability to engineer novel quasi-phase-matched (QPM) structures in periodically poled ferroelectric crystals has led to the development of a wide variety of innovative QPM devices. During PPLN fabrication, the optic axis of the crystal is periodically flipped 180° to set up a structure of alternating positive and negative values of the nonlinear coefficient. The period of this structure, called the grating period, determines the phase-matching characteristics for the crystal. The pattern that defines the grating structure is mapped onto the crystal using standard photolithographic techniques, which opens the door for virtually unlimited patterning options. Since the first demonstrations of electric field poling in periodically poled lithium niobate (PPLN),⁸⁻¹⁰ QPM structures have been fabricated for use in a number of pulsed and continuous-wave (cw) optical parametric devices. Just a few examples include multi-grating crystals,¹¹ chirped grating structures,¹⁶ asymmetric duty cycle gratings,³⁴ crystals with continuously varying grating periods ("fan-out" designs),³⁵ and two-dimensional (2-D) nonlinear photonic structures.²⁹

The fan-out grating design, or fan grating, is a logical extension of the multi-grating crystal (see Figure 2.1). Multi-grating devices are single crystals that contain multiple, discrete grating periods in the transverse direction. Such devices can be tuned in discrete wavelength steps by simply translating the crystal to change which grating the pump beam illuminates. The wavelength gaps between the discrete steps can usually be filled by changing the temperature of the crystal (i.e., temperature tuning). The fan grating is similar, but replaces the multiple discrete gratings with a single grating whose period varies continuously across the crystal. This allows continuous wavelength tuning over a broad spectral range by simple crystal translation without the need for temperature tuning.

We proposed an interesting variation on the continuously tunable PPLN fan system in which we flood illuminate the entire fan crystal to simultaneously generate broadband radiation over the full tuning range. This system could be thought of as an IR "white light" source. This concept seems straightforward enough, but aperture scaling in QPM devices presents some challenges. The fan grating is typically thought of as a continuously varying 1-D structure, but illuminating the full width of a fan makes it necessary to consider its full 2-D QPM characteristics. Most aperture scaling efforts to date have been driven by the desire for high-energy pulsed systems, but our efforts and recent demonstrations of 2-D QPM structures in PPLN²⁹ highlight the potential benefits of using larger pump beams to access the full 2-D nonlinear qualities of such devices.

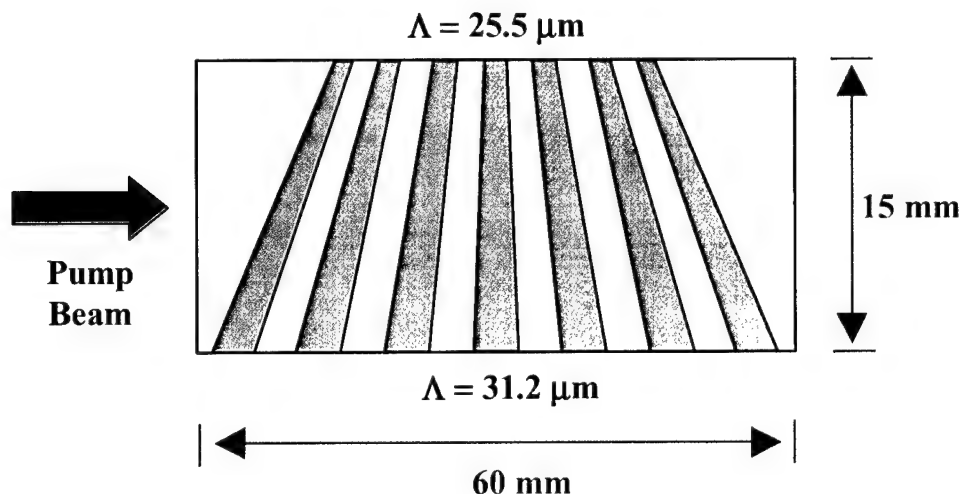


Figure 2.1 - Diagram of the fan grating crystal. Λ is the grating period (not drawn to scale) and varies continuously across the crystal.

In flood illuminated 2-D QPM devices, both the 2-D phasematching characteristics of the QPM material and the effects of large aperture pump beams will affect device performance. Thus, both effects must be considered when designing and evaluating these devices. The theoretical considerations for such systems were presented in Chapter 1. In this chapter we report the experimental results of pumping 2-D fan-out grating PPLN crystals with both small and large aperture beams. These novel PPLN devices can be used to produce extreme broadband tunability or to generate broadband IR radiation (i.e., can be used as an IR "white light" source). We also present results of

elliptical pumping in uniform grating PPLN and use those results to highlight some general theoretical and modeling considerations for large-aperture pumped or flood illuminated 2-D QPM structures.

2.2 Fan Grating Crystal Fabrication and Characterization

We used standard electric field poling techniques^{10,36} to fabricate 0.5-mm thick PPLN crystals with grating periods that vary continuously from 25.5 μm to 31.2 μm over a 15-mm width. First demonstrated by Powers *et al.*,³⁷ we commonly refer to crystals with this fan-out grating pattern as "fan" or "fan grating" crystals. The grating periods were chosen to generate signal and idler pairs in the 1.4- μm to 4.7- μm range by three-wave mixing with a pump beam of 1.064 μm at a temperature of 155°C. The large variation in grating period is significant because it causes domains at the edges of the fan to form greater than a 20° angle with respect to the standard domain orientation (standard orientation is parallel to the crystal y-axis). The crystals exhibited good poling fidelity throughout the length and width of the fan pattern. Since previous experiments have shown poor poling quality for angles corresponding to 30° with respect to the y-axis,³⁸ the fact that we achieved good domain quality is noteworthy (see Figure 2.2).¹²

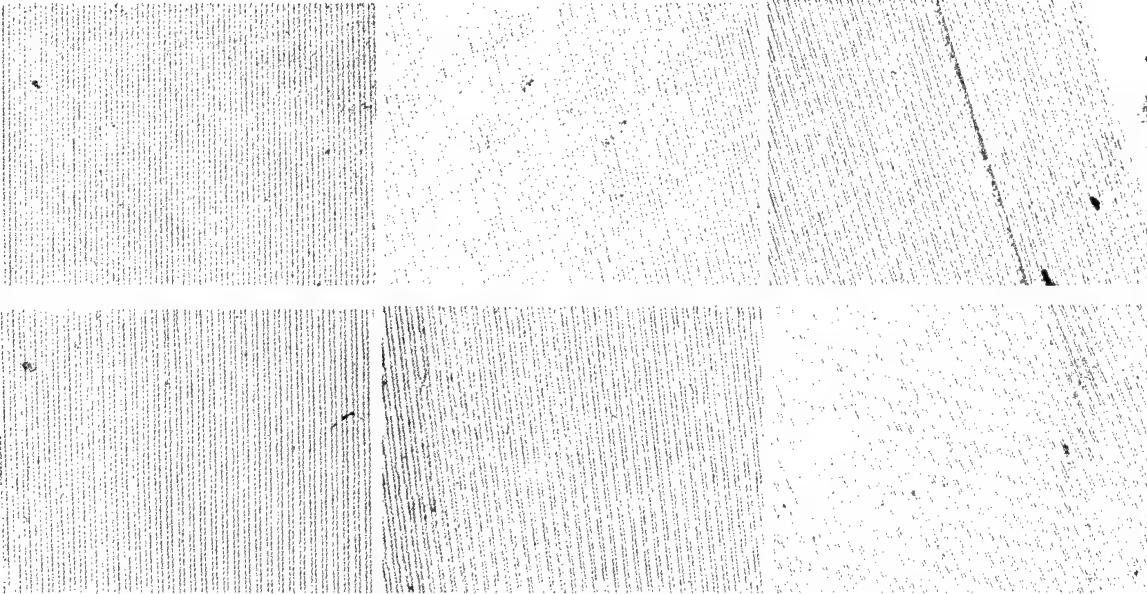


Figure 2.2 - Areas of the +z (top) and -z (bottom) surfaces of the 20° fan grating after HF etch.²⁷

In addition to the fan crystals, we fabricated several 0.5-mm thick PPLN crystals with a uniform grating period of 29.75 μm . After poling we cut and polished the crystals to 25-mm, 50-mm, and 60-mm lengths with widths of \sim 17 mm. We polished some crystals with wedged output faces to prevent back reflections from oscillating and polished the rest with plane-parallel endfaces such that the Fresnel reflections would set up a low-finesse, monolithic cavity in the crystals themselves.

To characterize the properties of the fan grating crystals, we first demonstrated broadband continuous tuning by pumping a 60-mm long fan grating crystal with a 120- μm diameter tophat profile beam. The crystal had wedged output faces and was pumped in an OPG (single-pass) configuration. The pump beam was supplied by a Coherent Infinity Nd:YAG laser operating at a wavelength of 1.064 μm and a repetition rate 30 Hz with pulsed widths of 3.5 ns. We also heated the crystal to 155 $^{\circ}\text{C}$ so that the longest period grating (31.2 μm) would be phase-matched at degeneracy. We then simply translated the crystal and recorded the spectral output using a monochromator. Our results, presented in Figure 2.3, show continuous tuning from \sim 1.38 μm to \sim 4.7 μm .

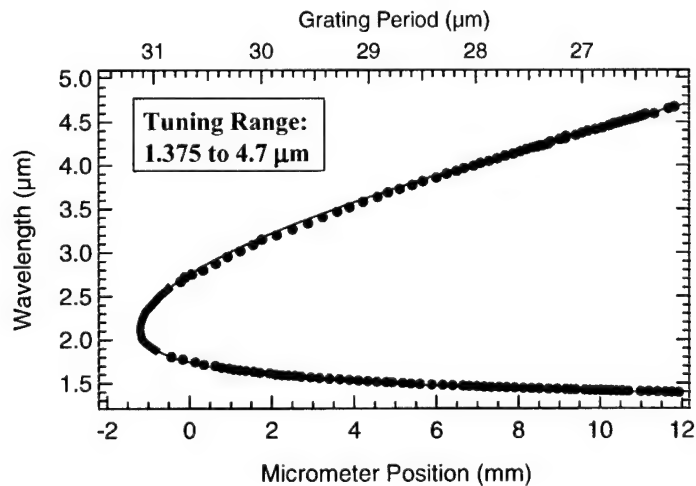


Figure 2.3 - Calculated (blue line) and measured (red markers) wavelength tuning curves for the 60-mm fan.²⁷ The large data point at degeneracy (2.128 μm) indicates that the bandwidth broadens considerably in this region.

After our initial tuning experiments, we compared the output spectra from the small diameter pumped fan grating to that of a small diameter pumped single grating for various grating periods. Both crystals were 50-mm long and had wedged output faces to prevent oscillation. We pumped the crystals with a 300- μm diameter gaussian beam from

the Coherent Infinity laser running at 10 Hz with 2.5 ns pulses. The pump energy was 500 μJ and the crystal was kept at room temperature ($\sim 30^\circ\text{C}$). The results, presented in Figure 2.4, show similar performance between single grating and fan grating structures; however, there is slightly more energy in longer wavelengths for the fan structures. This behavior is predicted by adapting the theory of spectral broadening in OPOs^{33,39} to accommodate the change in grating period across the pump beam in fan crystals (see Figure 2.5). The method we followed to make this calculation is outlined by Missey on page 31 of reference 27.

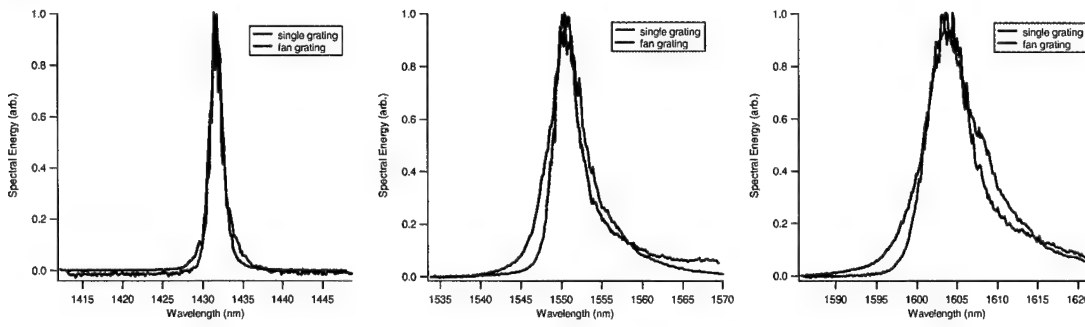


Figure 2.4 - Fan vs single grating spectral output comparisons for spectra centered at 1.432 μm (top left), 1.455 μm (top right), 1.550 μm (bottom left), and 1.605 μm (bottom right).

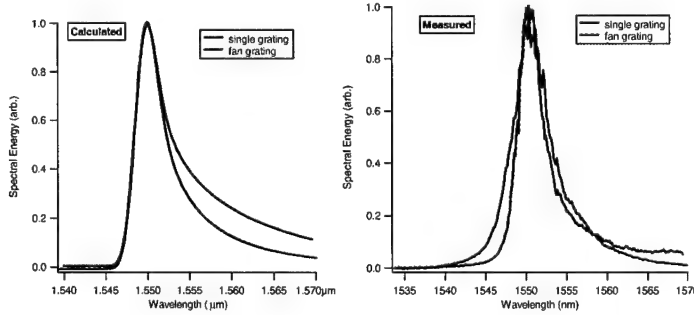


Figure 2.5 - Calculated (left) vs. measured (right) spectra centered at 1.550 μm for fan and single grating crystals.

In addition to output spectra, we looked at signal beam quality for the fan grating device. Again using a gaussian pump beam with $1/e^2$ diameter of 300 μm and pump energy of 500 μJ , we observed excellent beam quality ($M^2 \sim 1.2$ to 1.3 for a pump M^2 of 1.1) and good far field divergence properties (< 10 mrad). Our results indicate that fan grating devices operate with similar characteristics to single grating devices when pumped with small diameter beams.

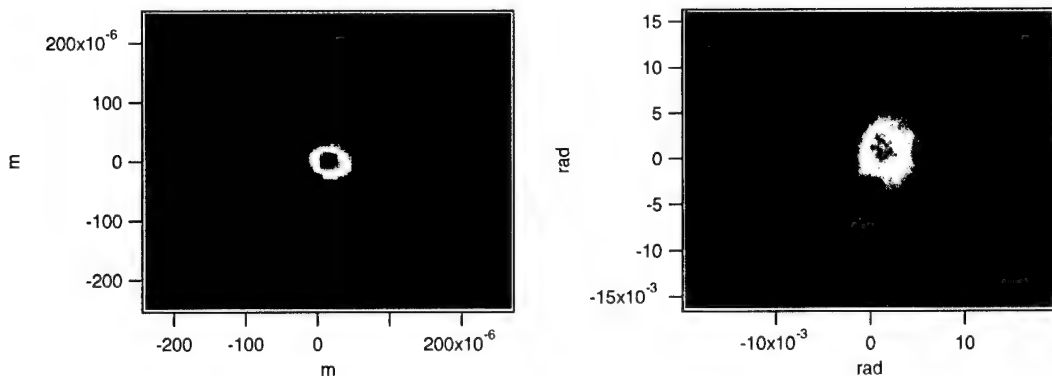


Figure 2.6 - Near field (left) and far field (right) signal beam produced by the fan grating crystal.

2.3 Monolithically Polished Fan Grating Performance

We polished several 50-mm and 25-mm fan crystals with monolithic endfaces such that the input and output surfaces were parallel to within less than 1 mrad. The reflections from these uncoated endfaces set up a low-finesse resonator within the crystal itself. To test these monolithic fan crystals we again used a gaussian pump beam with $1/e^2$ diameter of 300 μm and kept the crystals at 30 $^{\circ}\text{C}$. We measured output signal and idler energy as a function of input pump energy for a 50-mm long monolithic fan, then compared the results to those of a 50-mm fan with wedged output faces. We found that the monolithic crystal had a threshold of $\sim 215 \mu\text{J}$ versus a threshold of $\sim 300 \mu\text{J}$ for the wedged crystal. We also tested a 25-mm monolithic fan and found its threshold to be $\sim 300 \mu\text{J}$. For each measurement we translated the crystals to positions corresponding to an output signal wavelength of 1.55 μm . See Figure 2.7 for plots of these results. The plots also show the slope efficiency for the signal was 46 percent in the 50-mm monolithic fan versus 29 percent for the 50-mm wedged fan. The total conversion efficiency (i.e., pump energy into signal and idler energy) was 40 percent for the 50-mm monolithic fan versus 21 percent for the 50-mm wedged fan at a pump energy of 500 μJ . We did not pump the crystals at higher energies to ensure we kept fluence levels well below the damage threshold.

The lower thresholds and higher efficiencies for the monolithic crystals indicated that they were operating as low finesse OPO devices as opposed to operating in an OPG mode. This was further confirmed by looking at the spectral output of the monolithic

devices. The spectra show modulation behavior consistent with what is expected from a low-finesse etalon cavity of length equal to the length of the crystal (see Figure 2.8).

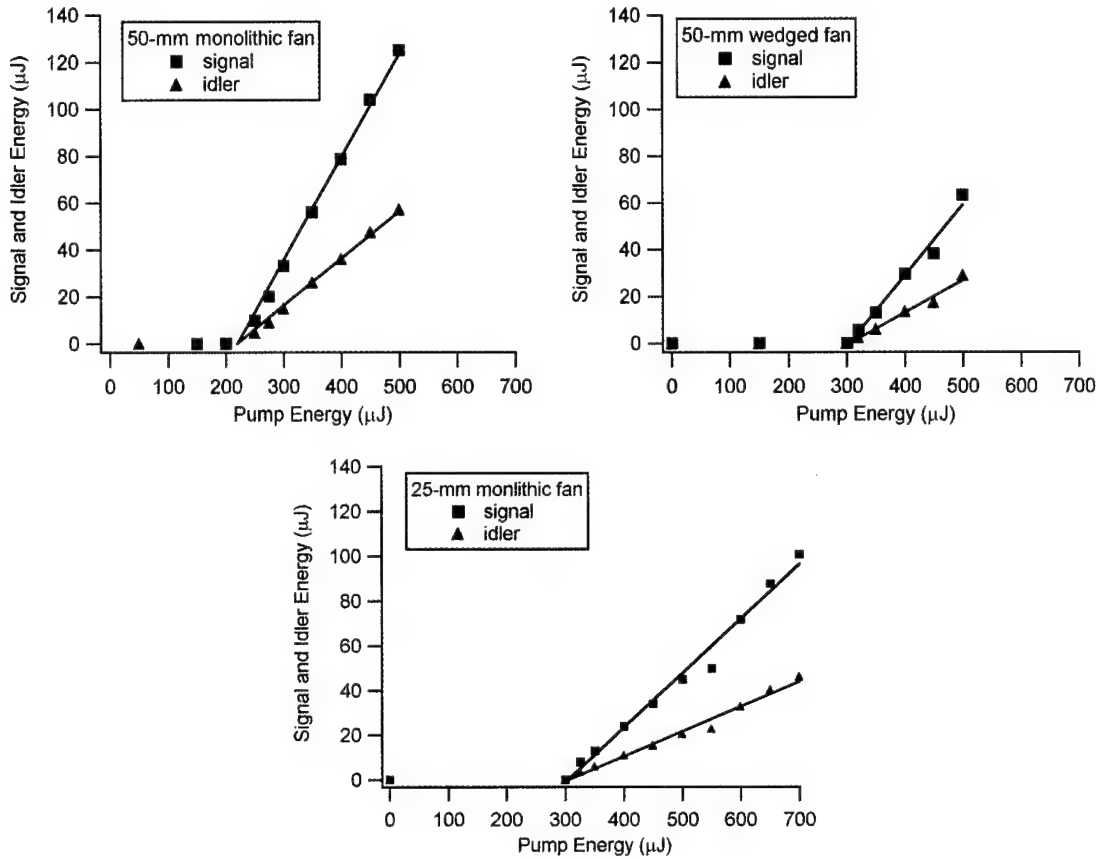


Figure 2.7 - Measured (markers) and linear fit (lines) threshold data for 50-mm monolithic fan (top left), 50-mm wedged fan (top right), and 25-mm monolithic fan (bottom).

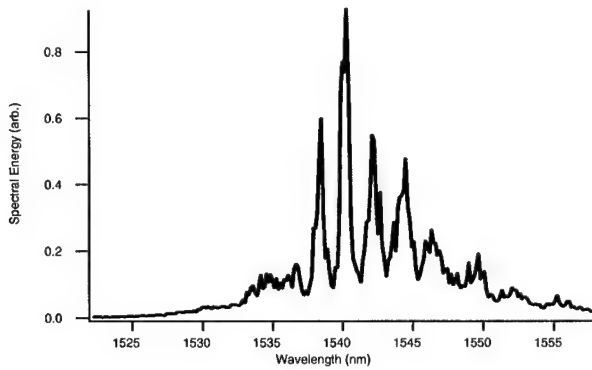


Figure 2.8 - Spectral output for a 25-mm monolithic fan crystal at $T=30^{\circ}\text{C}$ and pump energy of $500 \mu\text{J}$. The modulation spacing corresponds to a resonator length of 27.6 mm. Since our crystals had 25-mm active lengths plus a small dead zone, the 27.6 mm number is very close to our actual crystal length.

2.4 Elliptical Pump Experimental Setup

The initial motivation for designing the 20° fan crystal was to produce a broadband IR source, or IR "white light" source, to cover the 1.4 μm to 5.0 μm wavelength range. Our theory was that by illuminating the entire fan grating with an elliptical pump beam we could, in a single-pass, generate the entire spectrum (shown in Figure 2.3) produced by scanning the small diameter pump across the crystal. To experimentally investigate this theory and the theoretical concepts discussed in Chapter 1, we pumped both uniform grating and fan grating PPLN crystals with highly elliptical beams. We first tested the uniform grating crystals to confirm that large aperture beams would cause a preferred noncollinear OPG operation at wavelengths near degeneracy, then used fan grating crystals to perform both OPG and monolithic OPO experiments.

For all of our elliptical pumping experiments the pump beam was supplied by a Coherent Infinity Q-switched Nd:YAG laser operating at 10 Hz with 3.5-ns pulses. The operating wavelength was 1.064 μm and the output from the laser was a tophat beam profile. In our experimental setup (see Figure 2.9), we first magnified and imaged the tophat beam profile to a spot \sim 10 mm in diameter, then focused the beam in one dimension using a 100-mm cylindrical lens. Since the 100-mm cylindrical lens focused the beam too tightly in the vertical dimension, a second cylindrical lens ($f=50$ mm) was used to magnify and image the focus into the PPLN crystals. The result was a pump beam with a 0.310-mm $1/e^2$ diameter in the vertical dimension and an 8.6-mm $1/e^2$ diameter in the horizontal dimension (see Figure 2.10). Unless otherwise noted, all of our elliptical pumping experiments were conducted at room temperature. The low repetition rate of the pump laser allowed us to operate at room temperature without photorefractive effects.

Spectral measurements were made by placing a liquid nitrogen cooled HgCdTe detector in the exit plane of a monochromator, then scanning the monochromator grating across the wavelength range of interest. A large diameter (dia=82 mm), short focal length ($f=60$ mm) aluminum mirror was used to collect and focus the output from each crystal to a tight spot on a surface coated with a Spectrareflect diffuse reflectance coating. The spot was then imaged onto the input slit of the monochromator. Because broadband signal and idler beams were simultaneously generated in collinear and multiple noncollinear

directions, special care was taken to ensure all output light was collected and focused onto the diffuse surface. Long pass filters were used as necessary to prevent higher monochromator grating diffraction orders of the pump and signal from interfering with direct measurement of the idler. Beam quality (M^2) measurements were made by passing the output beam through a lens and measuring the beam's waist at the focus. We then compared the beam's propagation characteristics to those of a diffraction limited beam with the same waist by imaging the beam at multiple positions beyond the focus.

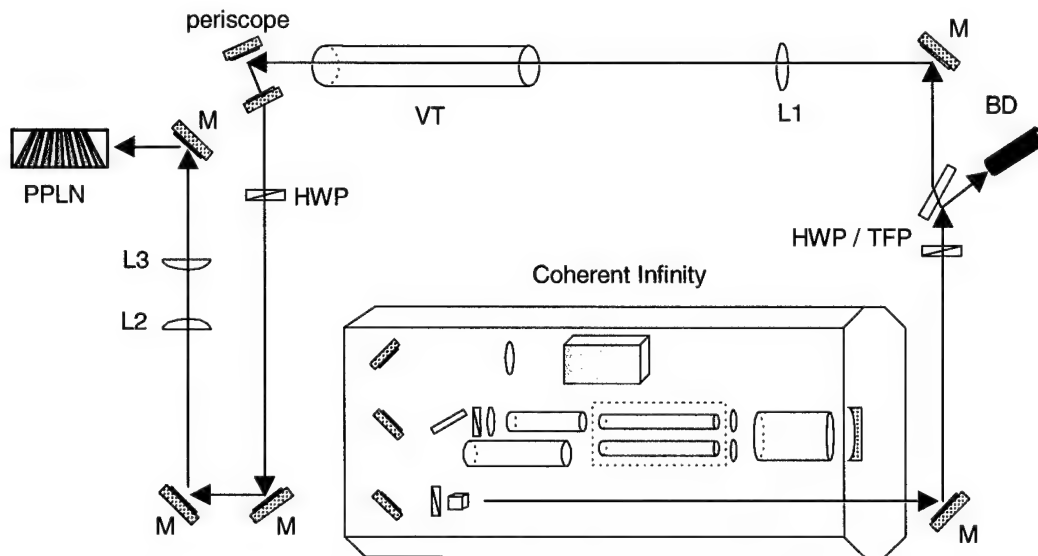


Figure 2.9 - Experimental setup for elliptical pumping experiments. The vacuum tube is required because the pump beam contains enough energy to ionize the air when it comes to a focus. M = mirror coated for high reflectivity at $1.064 \mu\text{m}$, HWP = half wave plate, TFP = thin film polarizer, BD = beam dump, VT = vacuum tube, L1 = 1000mm focal length lens, L2 = 100 mm focal length cylindrical lens, L3 = 50 mm focal length cylindrical lens.

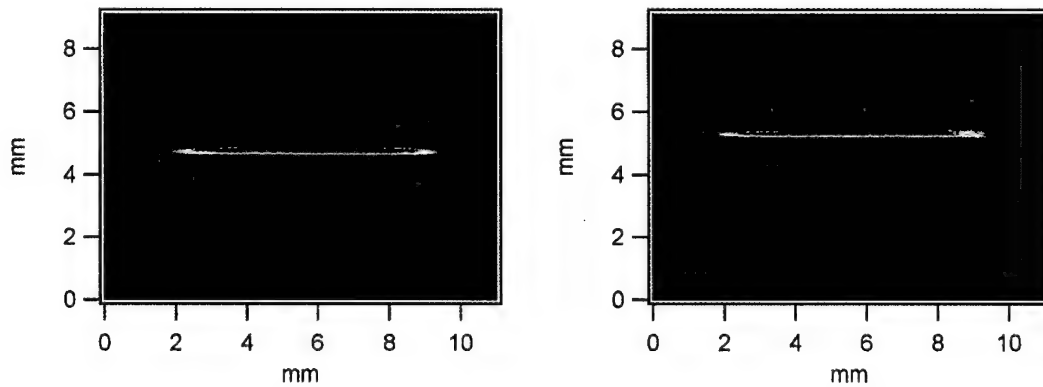


Figure 2.10 - Pump beam with no crystal present (left) and pump beam after passing through a 50-mm long, 0.5-mm thick PPLN crystal (right).

2.5 Elliptically-Pumped Uniform Grating Crystal Experiments

To demonstrate the effects of large aperture pump beams in a uniform grating crystal, we used the experimental configuration described in Figure 2.9 to pump a 0.5-mm x 10-mm x 25-mm (thickness x width x length) PPLN crystal with a 29.75- μm grating period. The output face was wedged to prevent Fresnel reflections from oscillating. Figure 2.11 shows near and far field images of the pump beam after passing through the crystal. Note that the far field image shows that the pump has been split into two distinct beams propagating in slightly different directions. The pump beam is split due to the optical phenomenon of double refraction. Since lithium niobate is a uniaxial (i.e., birefringent) crystal the pump beam is separated into two orthogonal polarization components, the extraordinary (\hat{e}) and ordinary (\hat{o}) polarizations, as it propagates through the PPLN crystal. The \hat{e} and \hat{o} components see different indices of refraction within the crystal and since the crystal output face is wedged, the two components refract by different amounts as they exit the crystal (i.e., they undergo double refraction). If both the \hat{e} and \hat{o} components struck the output face at normal incidence (as they would if the endfaces of the crystal were not wedged), the two components would pass straight through the crystal-air interface and would not be spatially separated.

In PPLN, the preferred polarization for the pump beam is \hat{e} and we attempted to linearly polarize the pump beam in the \hat{e} direction. However, the fact that we saw double refraction indicates our pump beam was not purely \hat{e} polarized. We were able to greatly reduce the amount of energy in the \hat{o} beam, but were unable to completely eliminate it. Since the polarization of the beam exiting the laser should be very pure, this slight deviation from linear polarization was probably caused by a slight misalignment of the mirrors in our periscope. If these mirrors were not perfectly orthogonal to the pump beam, they would generate a slight ellipticity in the beam polarization in addition to changing the height of the beam. Thus, since the QPM interaction is most efficient for a purely \hat{e} polarized pump beam, our pump polarization was slightly less than optimal. Although the fraction of total pump energy contained in each polarization was not measured directly, we estimate that greater than 95 percent of the energy was in the \hat{e} polarization.

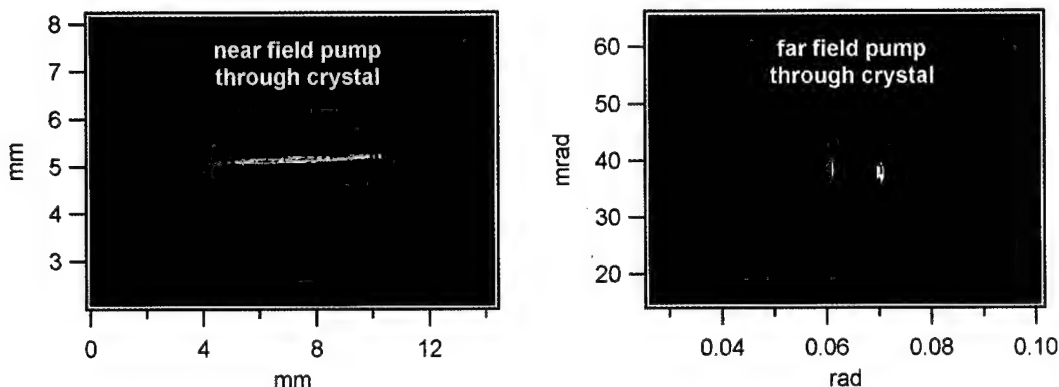


Figure 2.11 - Near field (left) and far field (right) images of the pump beam through a 0.5-mm thick, 25-mm long uniform grating crystal. The two far field beams are the ordinary and extraordinary polarizations.

The crystal was aligned such that the gratings were perpendicular to the direction of the pump (i.e., the grating vector was parallel to the pump wave-vector) and pumped in a single-pass OPG configuration. As we increased the pump energy, the first significant OPG output occurred at a pump energy of ~ 6 mJ and appeared simultaneously on both sides of the pump beam at noncollinear angles of $\pm \sim 2.6^\circ$. The signal and idler wavelengths were centered near degeneracy ($2.128 \mu\text{m}$), and the bandwidth broadened as pump energy was increased. Figure 2.12 shows the spectral content of the two noncollinear beams for a pump energy of 18 mJ.

We did not observe collinear OPG output until the pump energy reached ~ 9 mJ, at which point both noncollinear and collinear processes were observed to operate simultaneously. By reducing the horizontal aperture of the pump beam to less than 1 mm we were able to eliminate the noncollinear beams and force collinear operation at lower energies (~ 6.5 mJ); however, as the aperture was opened at these lower energy levels the noncollinear processes quickly took over again and eliminated collinear operation. This indicates that for large pump apertures the noncollinear beams were depleting the pump below OPG threshold for collinear operation. When pumped at 9.5 mJ, the overall pump depletion was 37 percent, with the noncollinear beams containing ~ 1.25 mJ each and the collinear beam containing ~ 1 mJ. These results agree well with the qualitative performance predicted by the theory in §1.3 for large aperture pump beams.

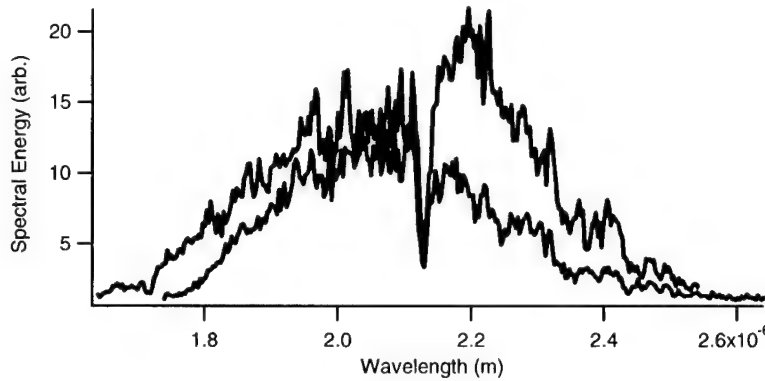


Figure 2.12 - Spectra for the two noncollinear OPG beams from an elliptically-pumped 25-mm PPLN crystal with a uniform grating period of 29.75 μm . The absorption notch at degeneracy is likely due to a coated reflecting element in the beam path.

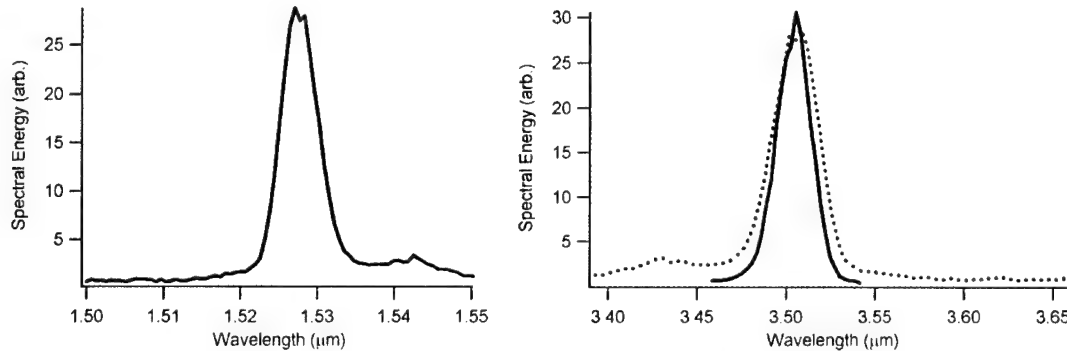


Figure 2.13 - Spectra for the collinear signal (left) and idler (right) OPG beams from the 25-mm PPLN crystal with a uniform grating period of 29.75 μm when the elliptical pump beam was apertured to less than 1 mm. For the idler spectra, the solid blue line represents the actual measured spectrum and the dotted red line is the idler spectrum calculated from the signal.

The results from the elliptically-pumped uniform grating crystal confirmed our theoretical predictions from §1.3. As expected, degenerate, noncollinear OPG processes were preferred when the crystal was illuminated by a large aperture pump beam. This may be fine if the desired signal-idler output is at degeneracy, but it presents an obvious problem if other signal and idler wavelengths are desired. In addition, the broad bandwidth at degeneracy may be too large for many applications. For example, the 29.75- μm grating period crystal used for this experiment was designed to produce a signal at 1.525 μm and idler at 3.520 μm when operated in a collinear geometry. However, the large aperture pump beam allowed other noncollinear processes to dominate the QPM interaction and steal gain from the desired signal-idler pair. For this reason we sought a

method to enhance the desired collinear operation and suppress the parasitic noncollinear processes.

One obvious solution to this problem is to set up an OPO resonator cavity to encourage oscillation in a particular direction. A simple linear cavity that resonates the signal, for example, could be used to choose a collinear or specific noncollinear direction for the QPM process (see Figure 2.14). Although this method is effective, setting up a resonator adds complication to the system. A less complex solution is to use the Fresnel reflections from the PPLN crystal endfaces to set up a monolithic cavity in the crystals themselves. Lithium niobate's index of refraction causes large Fresnel reflections (~14%) for mid-IR wavelengths at air-crystal interfaces. These reflections are large enough to set up a low-finesse monolithic cavity (see Figure 2.14).²⁷

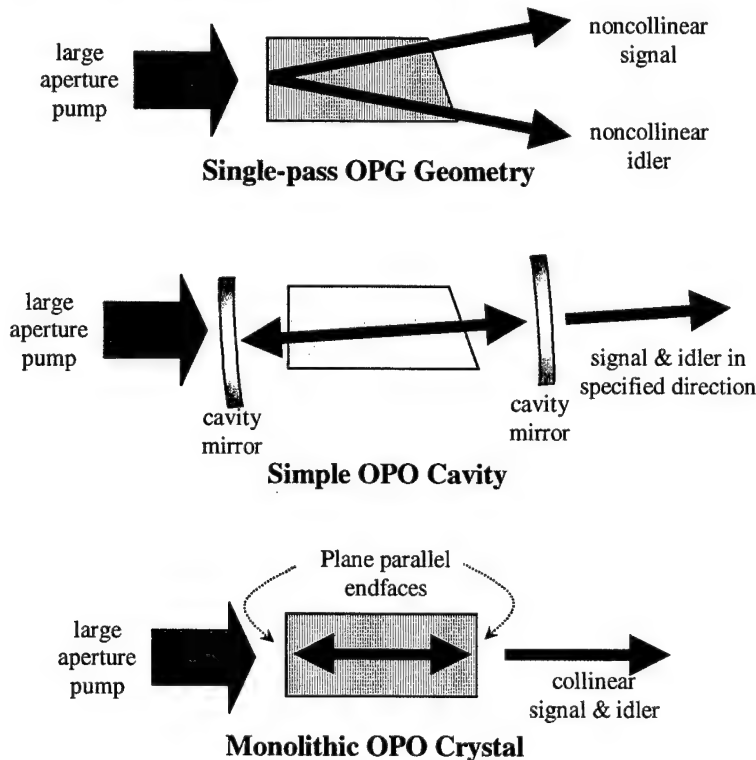


Figure 2.14 - Simple comparison of large aperture pumping configurations. A single-pass OPG geometry (top) produces degenerate noncollinear signal and idler beams. An OPO cavity (middle) allows the experimenter to choose the direction for the resonated wavelength. A monolithic OPO crystal (bottom) also forces oscillation in a specified direction with less complication than a typical OPO cavity.

To experimentally test the monolithic crystal design, we polished plane-parallel endfaces on a 0.5-mm x 10-mm x 50-mm (thickness x width x length) PPLN crystal with

a uniform 29.75- μm grating period. We then used the setup in Figure 2.9 to elliptically-pump the device. The crystal reached threshold at a pump energy of ~ 2 mJ with signal output in the collinear direction centered at a wavelength of 1.53 μm . As we increased the pump energy, the collinear signal-idler beam was the sole output up to ~ 6 mJ of pump, at which point degenerate noncollinear output began to appear. We pumped the crystal with pump energies as high as 32 mJ without crystal damage. The signal energy was 6.3 mJ at this pump level and we achieved a maximum conversion efficiency of 27 percent for the collinear signal-idler beam. This conversion efficiency was lower than those achievable in small diameter pumped systems because the noncollinear processes began to compete for gain at higher energies. The number and variety of noncollinear QPM interactions allowed by the elliptical pump beam is obvious from the multiple visible output beams observed at high pump energies. As seen in Figure 2.15, the visible output included a large variety of colors. These beams are indicative of parasitic sum frequency generation and second harmonic generation processes occurring between various combinations of the pump and/or multiple signal and idler beams.

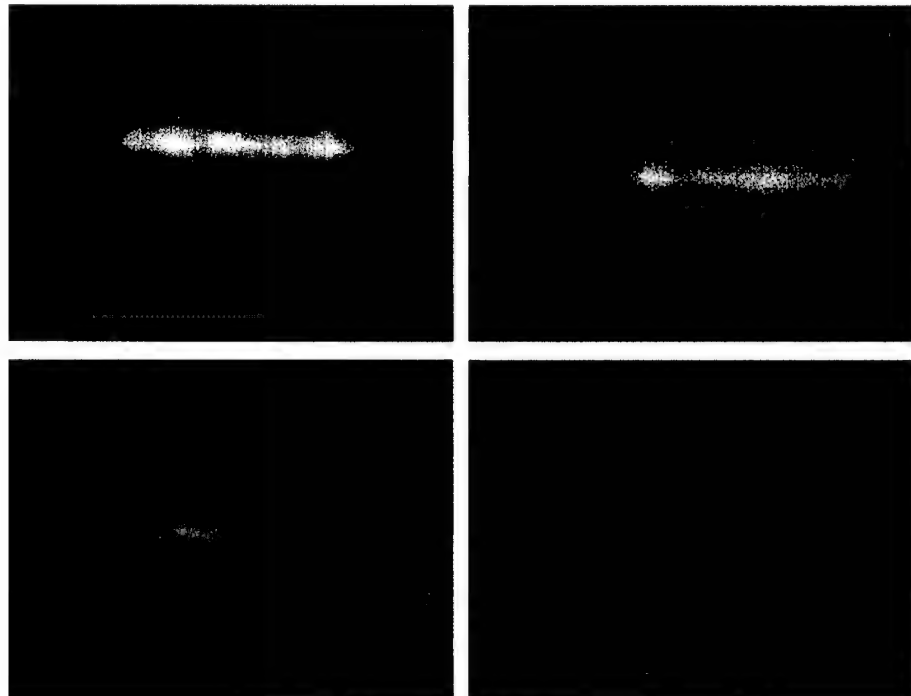


Figure 2.15 - Visible output from elliptically-pumped uniform 29.75- μm grating period PPLN crystal when pumped at 20 mJ. Images were taken using different filters to highlight the variety of colors produced. Since the SHG process is very strong, the 0.532 μm green SHG output was completely filtered out for all images.

The signal output from the monolithic crystals exhibited good beam quality at all pump energies. At 12 mJ of pump, the collinear signal energy was ~ 2.5 mJ and the beam had an M^2 of ~ 2.2 compared to an M^2 of 1.2 for the pump. Figure 2.16 shows near field and far field images of the pump and signal beams. Note that the far field pump image shows only one beam (i.e., there is no double refraction) because both the \hat{e} and \hat{o} components of the pump strike the monolithic faces of the crystal at normal incidence.

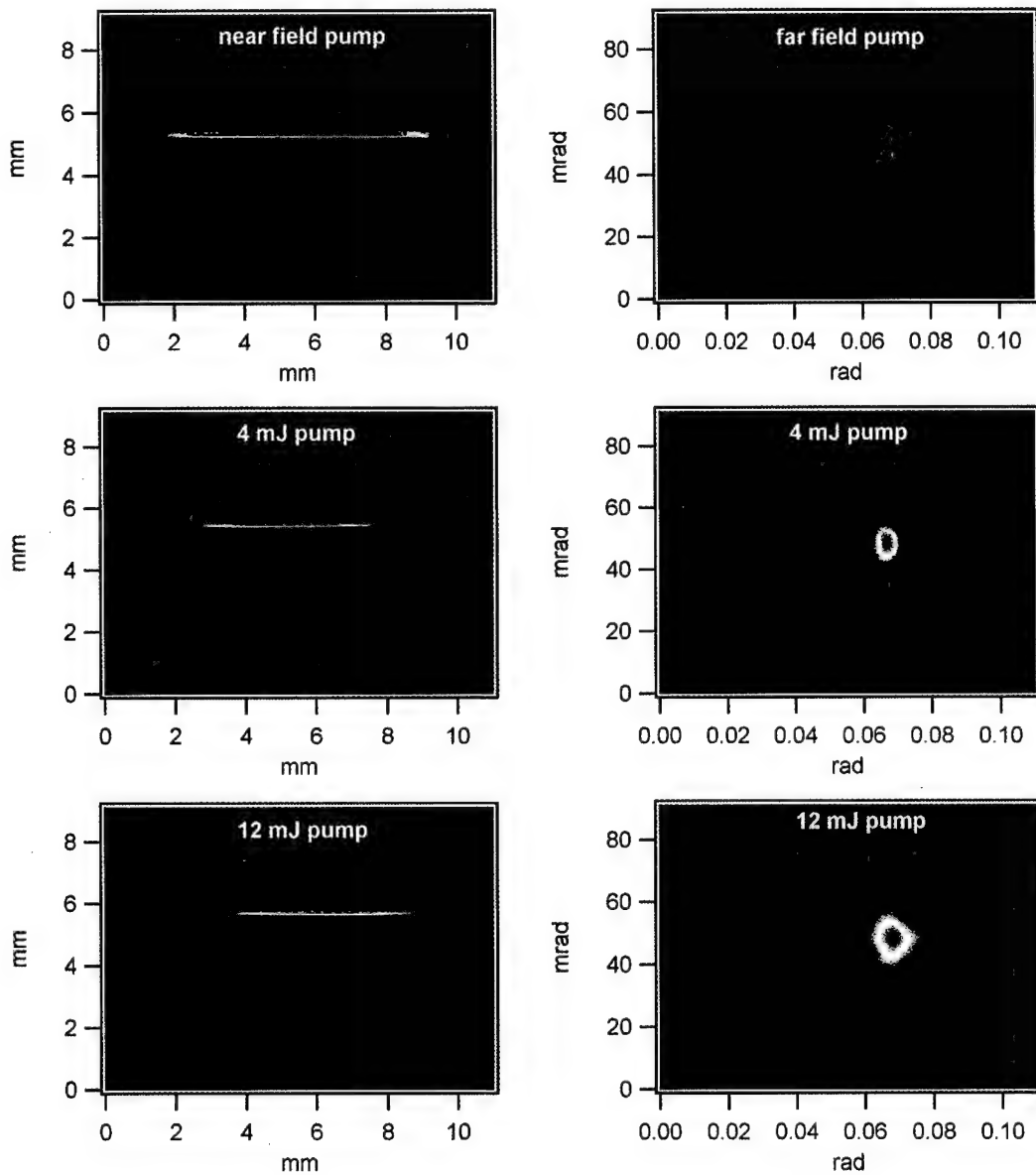


Figure 2.16 - Near field (left column) and far field (right column) images of the pump beam through a 0.5-mm x 10-mm x 50-mm uniform grating crystal (top), the signal beam generated at 4 mJ of pump energy (middle), and the signal for a 12 mJ pump (bottom).

The fact that the collinear QPM interaction was the first to reach threshold and continued to be the dominant process was confirmation that the monolithic OPO configuration is a viable way to force collinear operation in large aperture pumped systems. Although we simply used Fresnel reflections from the crystal endfaces to generate feedback, Missey demonstrated that high reflectivity coatings can be used to enhance the feedback process in monolithic devices.²⁷

2.6 Elliptically-pumped Fan Grating Performance

We used the same pumping scheme (see Figure 2.9) to illuminate 25-mm and 50-mm long fan grating crystals with 0.5-mm x ~17-mm endfaces that were wedged to prevent oscillation from Fresnel reflections. Although the 50-mm fan crystals reached OPG threshold at significantly lower pump energies (~4 mJ) than the 25-mm fan crystals (~12 mJ), both the 50-mm and 25-mm fans exhibited similar QPM characteristics and produced similar spectral output. As with the uniform grating crystals, noncollinear propagation directions corresponding to degenerate wavelengths were the first to reach OPG threshold, but we were able to force collinear operation at low energies by closing the aperture of the pump to less than 1 mm. The noncollinear propagation directions were $\pm \sim 2.6^\circ$ with respect to the propagation direction of the pump beam. An example of the spectral content of the noncollinear beams is provided in Figure 2.17.

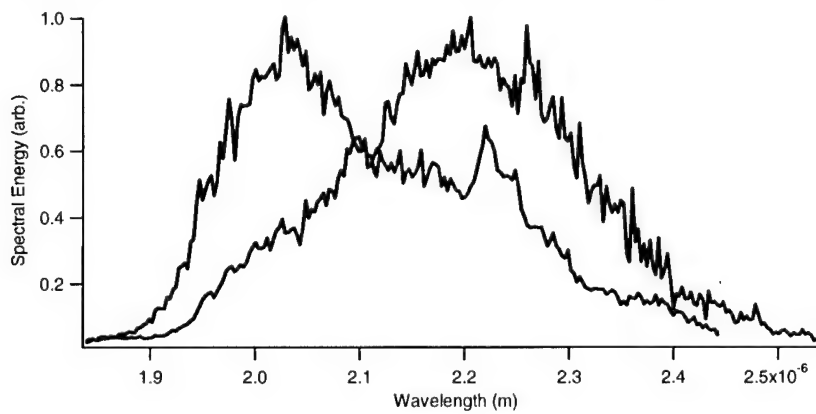


Figure 2.17 - Spectral content of the two noncollinear beams from an elliptically-pumped 50-mm long fan grating crystal with a wedged output face. The pump energy was 8 mJ and the pump wavelength was 1.064 μm . The fact that the peaks do not occur right at degeneracy indicates slight crystal rotation (misalignment).

Collinear signal output was not generated in the 50-mm fan until the pump energy was increased to ~ 9 mJ and was not observed with the 25-mm wedged fan even for pump energies as high as 20 mJ (we did not pump with higher energies to avoid crystal damage). At a pump energy of 10 mJ, the collinear signal energy for the 50-mm fan was 200 μ J and the measured bandwidth spanned from 1.52 μ m to 1.69 μ m (see Figure 2.18). This entire spectral band shifted as the crystal was translated in the transverse direction because the pump beam did not illuminate the entire fan grating. Thus, crystal translation changed the range of grating periods filled by the pump beam. The overall bandwidth also expanded with translation to longer grating periods (toward degeneracy) and contracted with moves to shorter grating periods. Near and far field signal beam images are provided in Figure 2.19.

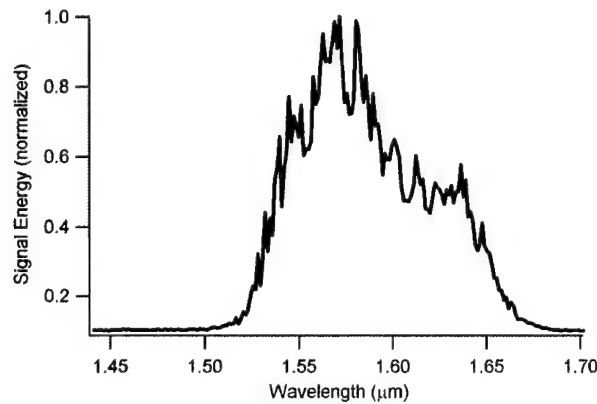


Figure 2.18 - Collinear signal spectrum from a wedged fan crystal elliptically-pumped at 10 mJ.

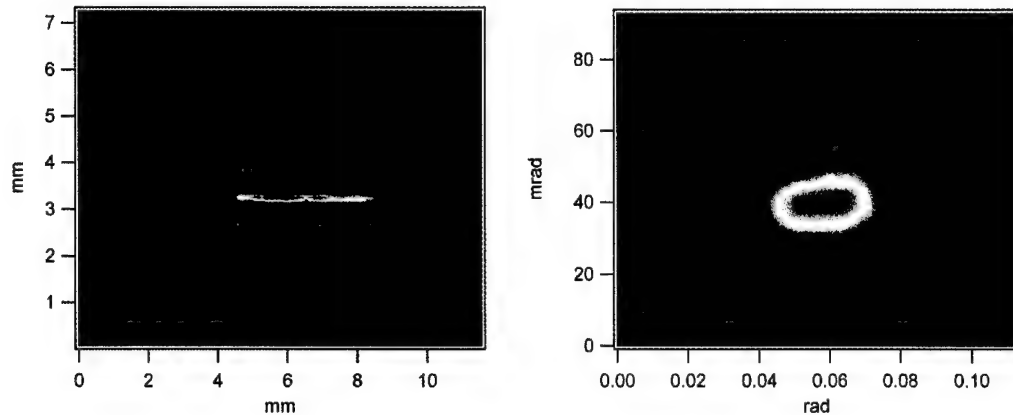


Figure 2.19 - Near field (left) and far field (right) collinear signal beam images from the wedged fan grating crystal. Pump energy was 10 mJ and the crystal was at room temperature (~ 30 $^{\circ}$ C).

Our initial motivation for elliptically pumping the fan crystals was to efficiently generate broadband mid-IR output. The fan crystals were designed to produce collinear signal and idler beams that cover the entire bandwidth shown in Figure 2.3. However, since the fan crystals with wedged output faces prefer to operate at wavelengths near degeneracy, the most efficient QPM interactions were in noncollinear directions when elliptically-pumped. Although Figure 2.17 shows that these noncollinear beams were still extremely broadband, covering spectral ranges on the order of 800 nm ($\sim 1700 \text{ cm}^{-1}$), they were centered at degeneracy and did not efficiently generate collinear output in the other wavelength ranges that the fan grating periods were designed to produce. Furthermore, the traces in Figure 2.12 show that a uniform grating crystal produces similar degenerate output for the same pumping scheme. Therefore, we needed a different method that would force operation in the collinear direction and take full advantage of the fan structure. Note that this requirement was predicted by the Fourier transform of the fan in §1.4. We showed in §2.5 that polishing plane-parallel endfaces on uniform grating crystals results in collinear monolithic OPO resonator modes with higher gain than the noncollinear OPG gain. Thus, we attempted to encourage similar behavior in the fan crystals by monolithically polishing their endfaces.

We tested both 25-mm and 50-mm long monolithic fan grating crystals using the elliptical pumping setup described above. The improvement in performance over the wedged fan crystals was immediately obvious in the form of lower thresholds and better signal beam quality. The 50-mm monolithic fan reached threshold in the collinear direction at just 2 mJ, and well before any noncollinear beams were observed. Recall that the thresholds for the 50-mm wedged fan were 4 mJ (noncollinear) and $\sim 9 \text{ mJ}$ (collinear). As we continued to increase the pump energy, the collinear signal beam also increased in energy and the noncollinear beams began to appear at $\sim 8 \text{ mJ}$ of pump. The collinear signal beam could also be operated in a noncollinear geometry through crystal rotation. We measured 4 mJ of collinear signal energy for an input pump energy of 20 mJ, but did not go to higher pump energies. Higher signal energies should be easily achievable, but we kept the pump energy well below the crystal damage threshold to preserve the crystal for future experiments. The 25-mm monolithic fans exhibited similar performance to the

50-mm monoliths, but with higher threshold values. The 25-mm fan reached OPG threshold for collinear operation at ~ 4 mJ and well before any noncollinear beams were observed. This is also much improved over the 25-mm wedged fan, which did not generate a collinear beam even at 20 mJ of pump and had threshold of ~ 12 mJ for noncollinear signal-idler pairs.

Typical collinear and noncollinear spectral output from the elliptically-pumped monolithic fans is presented in Figure 2.20 and Figure 2.21 respectively. The noncollinear output is very similar to that of the wedged fan crystals, but the collinear spectra from the monolithic crystals continuously spans sections of the wavelength range shown in Figure 2.3 and predicted by the 2-D Fourier transform in §1.4. The collinear signal and idler bandwidths were ~ 1200 cm^{-1} ; however, it should be noted that since the transverse width of the pump beam is only 8.6 mm and the width of the fan crystal is 15 mm, we were not fully illuminating the entire fan at any one time. The size of the pump beam was limited by our optics, but illumination of the entire fan is easily possible with the proper optics and should show an even larger spectral range for the collinear signal and idler waves. Since the diameter of the pump beam was smaller than that of the fan, we could tune the collinear signal and idler wavelength ranges by crystal translation to cover the entire spectral range demonstrated by the small pump in Figure 2.3. In addition, data taken at both room temperature and 155°C showed that the elliptically-pumped crystals can still be temperature tuned.

The longest grating period of the fan (31.2 μm) was designed to phase-match at degeneracy in a collinear geometry at $T=155^\circ\text{C}$. The fact that the collinear signal and idler spectra in Figure 2.20 do not extend through degeneracy indicated that the longest grating period was not illuminated when the data was taken. So we translated the crystal until the pump beam illuminated the 31.2 μm grating and took spectral measurements of the collinear beam. As the results in Figure 2.22 show, the collinear beam continuously spans from 1.5 μm through 3.66 μm (over 3900 cm^{-1}). To our knowledge, this is by far the broadest bandwidth ever produced in a QPM material on a pulse-to-pulse basis (i.e., without tuning). Again it is worthy of note that we are only illuminating a little over half

of the fan crystal with our pump beam. Thus, this bandwidth can easily be expanded even further by using a pump beam with a larger transverse dimension.

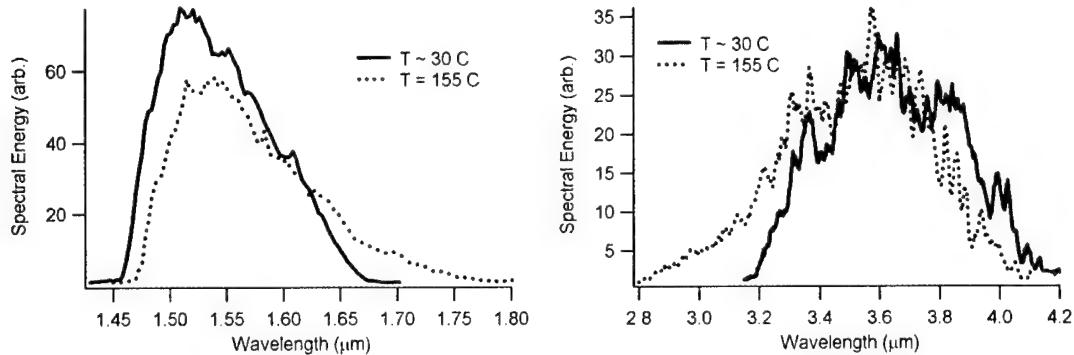


Figure 2.20 - Collinear signal (left) and idler (right) spectra for the 50-mm monolithic fan crystal pumped at 10 mJ. The solid red lines are spectra taken at room temperature and the dotted blue lines are spectra taken at $T=155^{\circ}\text{C}$.

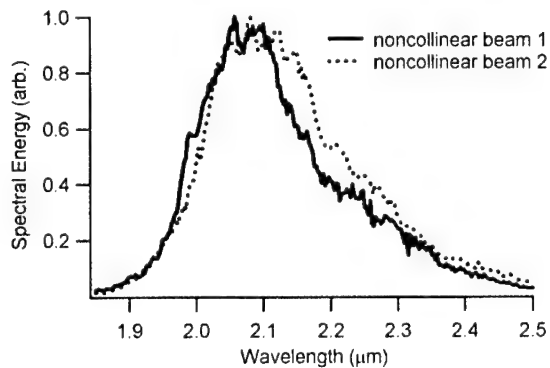


Figure 2.21 - Noncollinear output from a 50-mm monolithic fan crystal pumped at 10 mJ. The two beams were a noncollinear signal-idler pair propagating at angles symmetric about the pump beam.

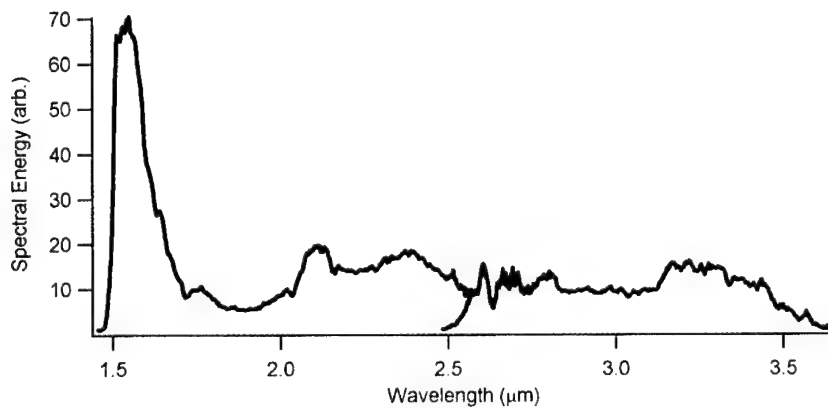


Figure 2.22 - Collinear spectra from the 50-mm monolithic fan crystal at $T=155^{\circ}\text{C}$. The scan was taken in two sections, wavelengths less than $2.5\text{ }\mu\text{m}$ and wavelengths greater than $2.5\text{ }\mu\text{m}$. A long-pass ($2.5\text{ }\mu\text{m}$) filter was placed in the beam for the long wavelength scan to ensure higher diffraction orders of shorter wavelengths did not corrupt the measurement.

At first glance, the energy distribution across the wavelengths in Figure 2.22 seems uncharacteristic; however, there are several explanations for this seemingly strange distribution. First, the pump beam has a roughly gaussian profile, so it illuminates some grating periods with greater intensity than others. For the measurements in Figure 2.22, the 30.5- μm grating period (corresponding to a collinear signal wavelength of 1.6 μm) was illuminated by the peak intensity of the pump beam. This leads to more signal energy in the 1.6 μm range and the corresponding 3.2 μm idler range. Second, the substrates of the various filters used to reduce the overall beam energy to safe levels for the detector tend to absorb longer wavelengths more than shorter wavelengths. Moreover, the addition of a long-pass filter for the long wavelength scan changed the energy distribution characteristics from the first scan to the second. Finally, as shown in Figure 2.23, there is strong atmospheric absorption in the 1.8 μm to 2.0 μm range. Although the resolution of our scan was not fine enough to resolve individual absorption features, this is likely the cause of the lower energy levels measured in that range.

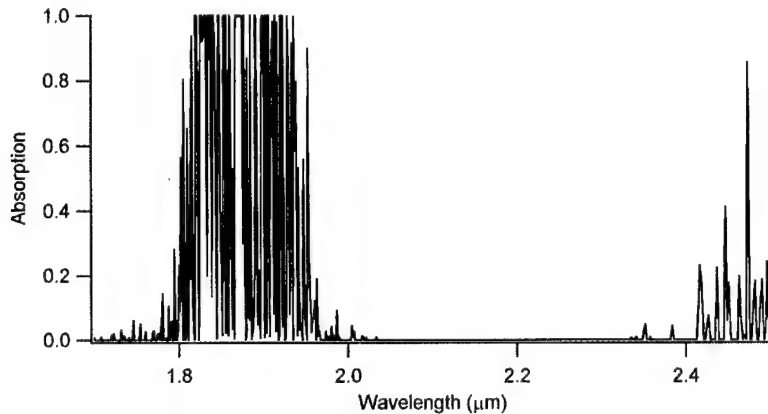


Figure 2.23 - Atmospheric absorption trace generated by the high-resolution transmission (HITRAN) molecular absorption database.⁴⁰

As mentioned above, since the pump beam has a roughly gaussian profile it does not illuminate the fan with equal intensity. For this reason, the area illuminated by the center of the pump beam (the area with highest intensity) should turn on the OPG interaction at a lower pump energy than the areas illuminated by the wings of the pump. As the pump energy is increased, we expect more of the fan grating to turn on. This should in turn cause the output spectrum to broaden since a larger range of grating

periods would then be illuminated above threshold. To test this we pumped a 50-mm monolithically polished fan at room temperature and various energy levels, then measured the output spectra for each energy level using a monochromator and a linear array. The results, shown in Figure 2.24, confirm that the bandwidth of the signal beam broadens as the pump energy is increased. Although they are not shown, there are corresponding idler bandwidths in the ~ 3 to 4.7 μm range for each signal bandwidth measured.

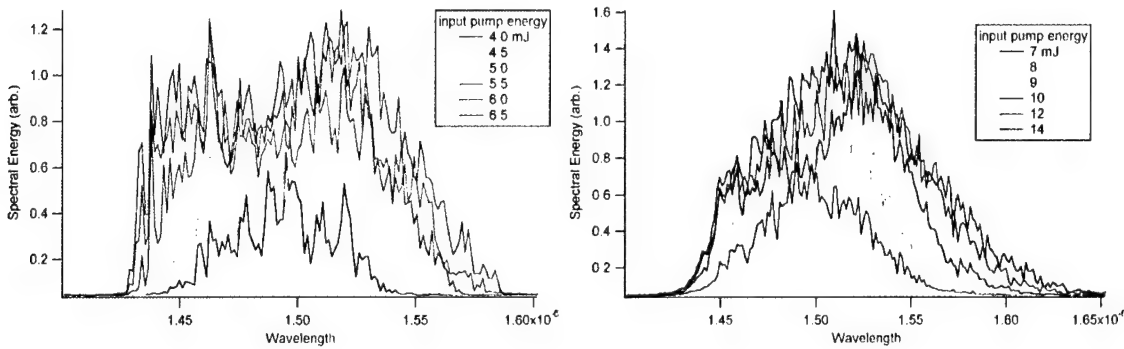


Figure 2.24 - Signal output spectra for pump energies from 4 to 6.5 mJ (left) and 7 to 14 mJ (right).

In addition to the spectral measurements, we imaged the near and far field signal beams of both the 25-mm and 50-mm monolithic fans for different pump energies. The signal images from the 50-mm monolithic fan are provided in Figure 2.25, and they provide further insight into device performance. The near field images confirm the results of Figure 2.24 that more of the grating is turning on as pump energy increases, but the far field images present an interesting result. We see from our first set of far field images for the 50-mm monolithic fan (middle column in Figure 2.25) that the far field image spreads out in one direction as pump energy is increased (Note: the color scheme is autoscaled for each image, so red in one image is not necessarily equal in energy to red in other images). This is significant because it implies that different wavelengths are propagating in slightly different directions. We initially aligned the crystal by observing the near field pump and signal beams at the crystal output face, but by realigning with the far field image as our reference we were able to reduce the effect considerably (right column of Figure 2.25) and greatly improve the overall beam quality. This illustrates that proper alignment is critical in the fan crystals. We also used the far field images to align the 25-mm monolithic fan crystals for the signal images in Figure 2.26.

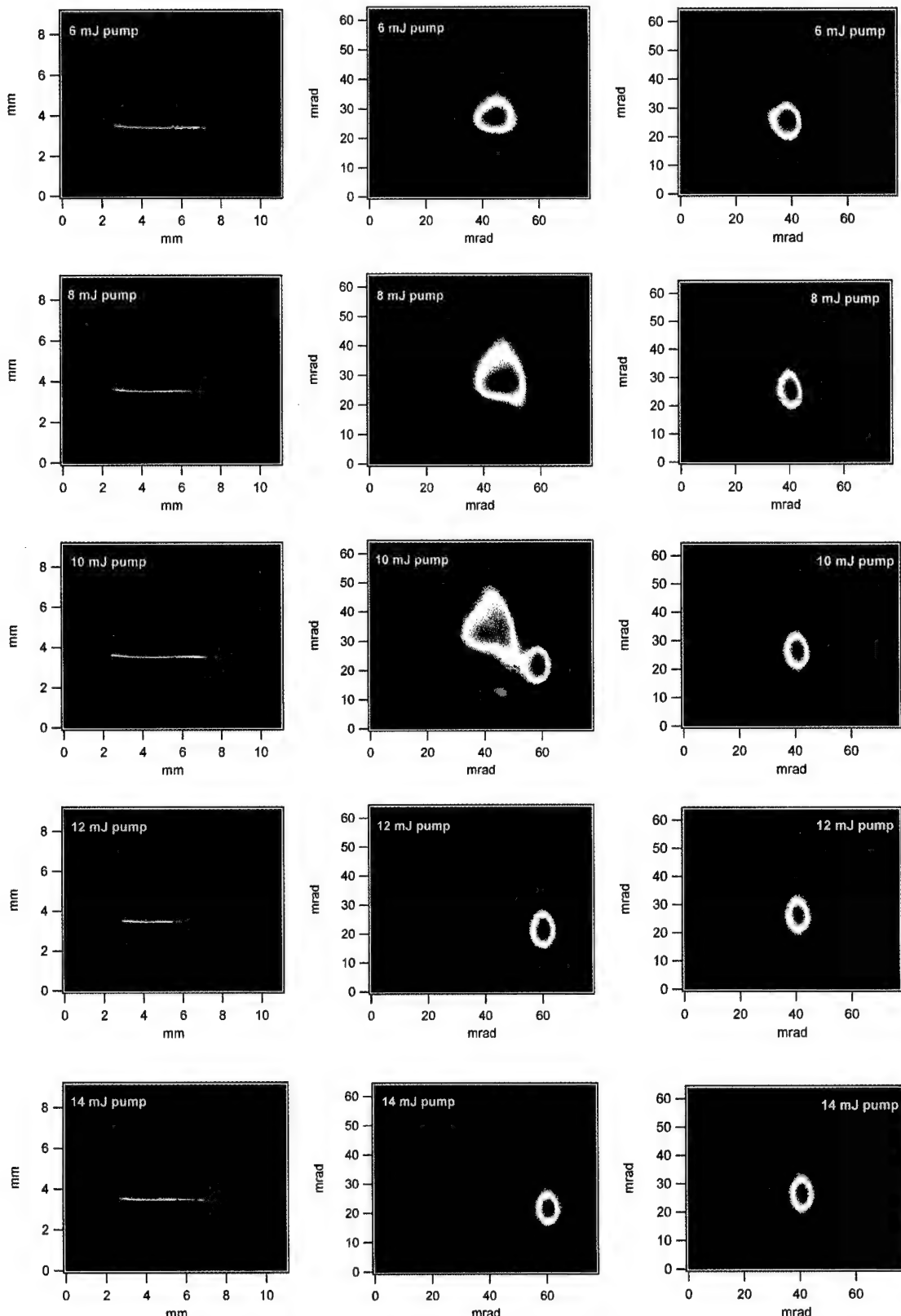


Figure 2.25 - Near field (left column), far field (middle column), and far field after realignment (right column) images of the signal beam from a 50-mm monolithic fan crystal for various pump energies.

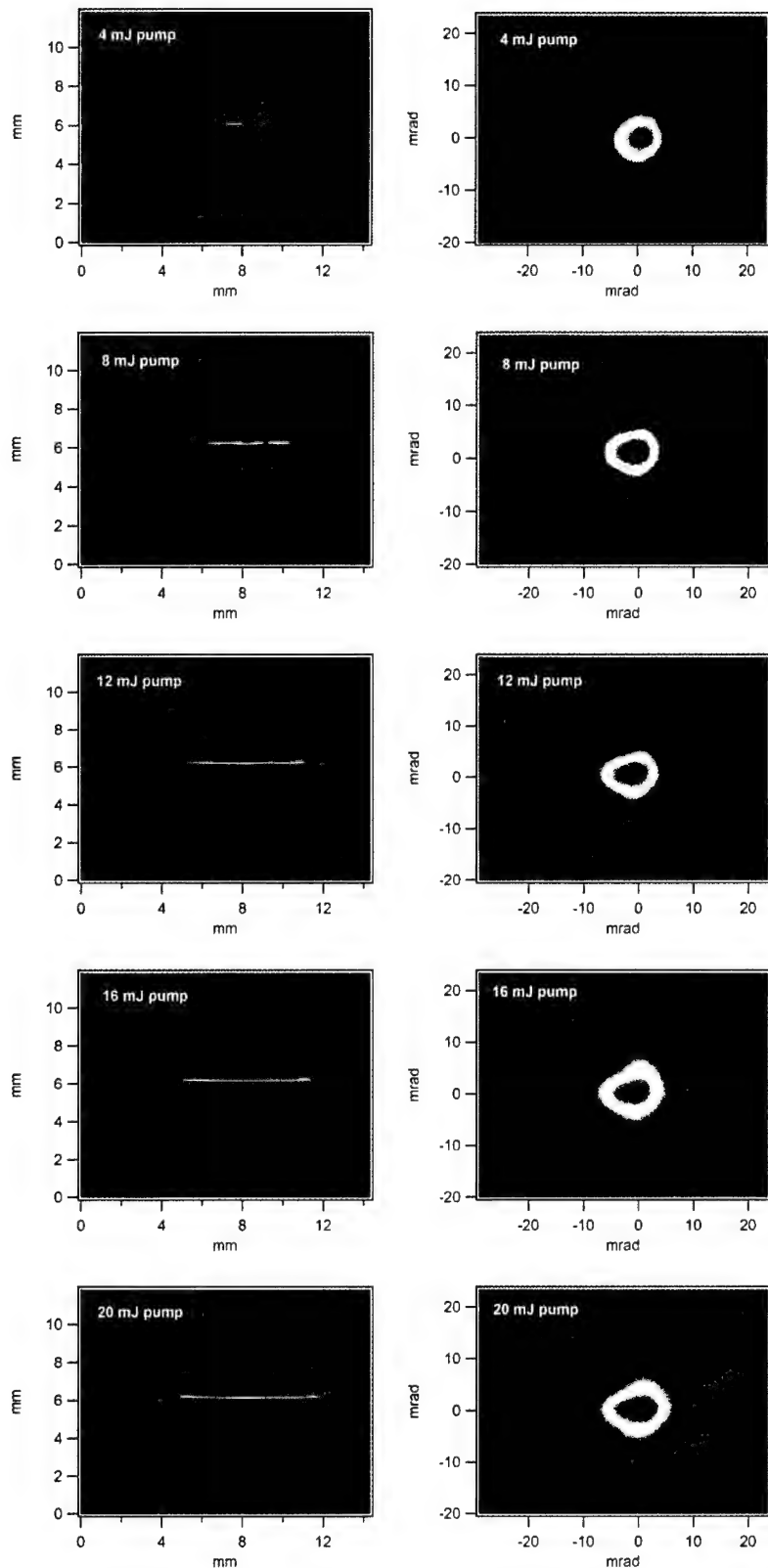


Figure 2.26 - Near field (left column) and far field (right column) signal images from a 25-mm monolithically polished fan crystal for various pump energies.

M^2 values for the 50-mm monolithic fans ranged from ~ 1.3 at 4 mJ of pump energy to ~ 4.2 at 14 mJ of pump for a pump M^2 of 1.1. For the 25-mm monolithic fans, M^2 values ranged from ~ 8 for an 8 mJ pump to just over 9 for 20 mJ of pump energy. The 50-mm crystals exhibit better beam quality (i.e., better M^2 values) than the 25-mm crystals for two primary reasons. First, as illustrated in Figure 2.27, for a fixed gain width in the PPLN crystal (defined by the pump beam), decreasing crystal length increases the range of noncollinear signal and idler angles that can see gain for the full length of the crystal. This, in turn, leads to an increase in the beam's overall far field divergence. Second, as pointed out by Missey in reference 27, decreasing the ratio of cavity length to gain width in a flat-flat cavity (such as the monolithic OPO) allows higher order modes to oscillate. The high off-axis angular content of these higher order modes leads directly to spectral broadening and an increase in far field divergence.²⁷

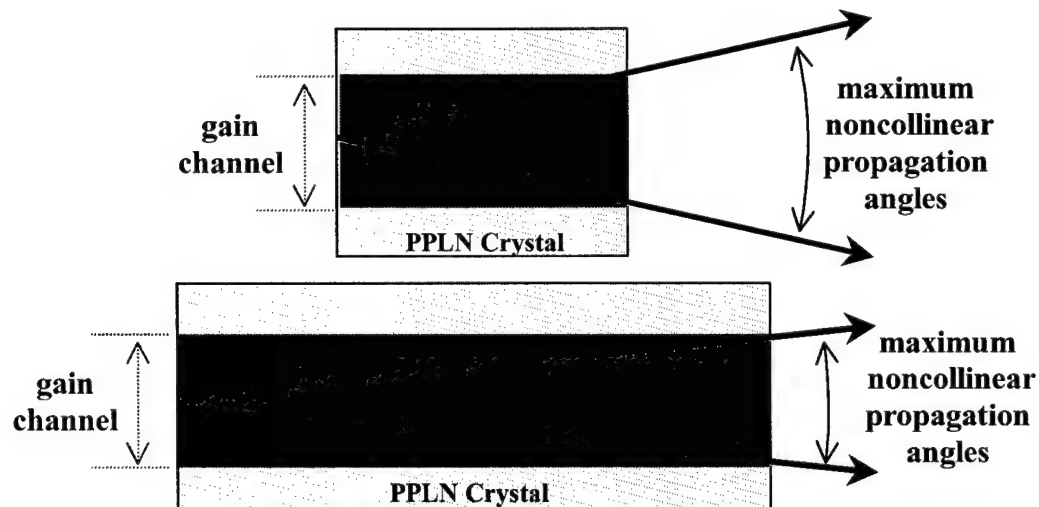


Figure 2.27 - Illustration of the effect of crystal length on far field divergence properties of beams generated by parametric interactions. The blue shaded area represents the gain channel in the crystal that is defined by the dimensions of the pump beam.

Figure 2.25 shows that the far field signal beam can be greatly improved by proper crystal alignment. However, it is of interest to note that even after optimizing the far field alignment the signal beam remains spatially chirped in the near field and angularly chirped in the far field. We confirmed this by scanning a razor blade across the signal beam at various positions and measuring the spectral output for each razor blade position.

The results from a scan of the far field signal are shown in Figure 2.28, and from this data the angular chirp was measured to be ~ 18 nm/mrad in the far field. Although the chirp may be useful for applications in which spatial separation of wavelengths is desired, it also offers a method to decrease the overall far field divergence of the beam. The fact that each wavelength is propagating in a slightly different direction leads to an increase in the far field divergence. By using an appropriate grating or set of prisms, it should be possible to reduce or remove the angular chirp and thereby greatly improve the divergence properties of the far field beam.

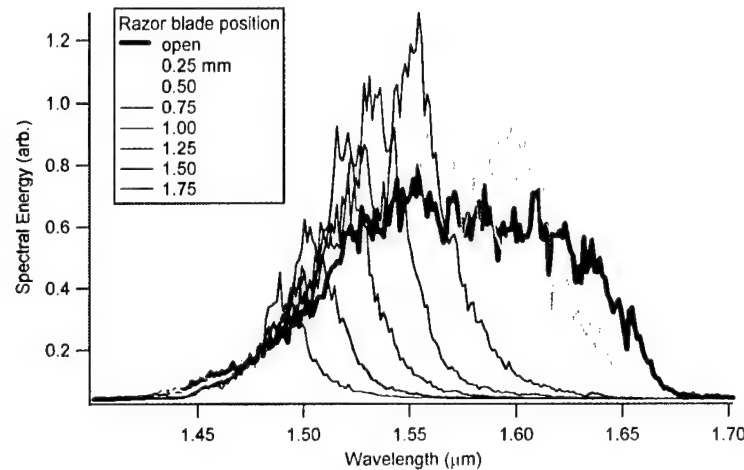


Figure 2.28 - Output spectra of the far field signal beam versus position of a razor blade scanned across the beam.

Finally, by simply placing an etalon in the beam path it is possible to generate broadband frequency combs in the mid-IR. The spacing between channels in the comb is easily adjusted by varying the spacing of the etalon. Furthermore, the frequency comb retains the same spatial and angular chirp characteristics as the original beam. We demonstrated this using two different etalon spacings. The results presented in Figure 2.29 show a 48 cm^{-1} (~ 11 nm or 1.4 THz) frequency separation between channels of the comb for an etalon spacing of 0.1 mm, and a channel separation of 9.6 cm^{-1} (~ 2.18 nm or 288 GHz) for an etalon spacing of 0.5 mm.

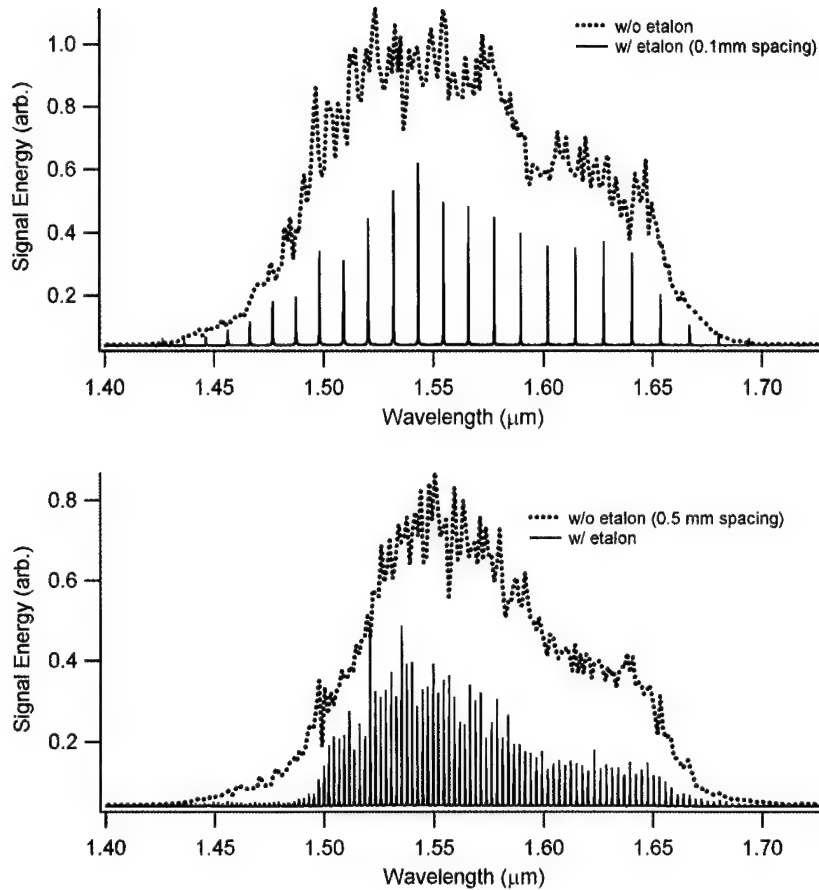


Figure 2.29 - Frequency combs generated by passing the signal beam through an etalon with 0.1-mm spacing (top) and an etalon with 0.5-mm spacing (bottom). The dotted black lines are the spectra taken without the etalon and the solid red lines are the spectra taken with the etalon in the beam.

2.7 Summary

We have demonstrated the use of highly elliptical pump beams to generate broadband, spatially-chirped mid-IR light in PPLN. The device is both simple, with no external cavity mirrors to align, and robust, able to withstand large pump energies. We fabricated uniform grating PPLN crystals and crystals with a fan-out grating period varying continuously from 25.5 μm to 31.2 μm across a 15-mm width and pumped them in both optical parametric generator and monolithic optical parametric oscillator configurations. We first verified that, in agreement with the theory discussed in §1.3, the phase-matching and gain characteristics of the crystals prefer noncollinear OPG operation for elliptical pump beams. However, collinear operation was achieved by polishing plane-

parallel crystal endfaces such that the Fresnel reflections set up a low-finesse monolithic cavity in the crystals themselves.

The signal and idler beams generated by the monolithic fan crystals were spatially chirped in the near field and angularly chirped in the far field while covering spectral bands as large as 3900 cm^{-1} . M^2 values for the 50-mm monolithic fans ranged from ~ 1.3 to ~ 4.2 for a pump M^2 of 1.1, and from ~ 8 to just over 9 for the 25-mm monolithic fans. By simply placing an etalon in the beam path, the system also offered an easy way to generate broadband optical frequency combs across the signal and idler spectral bands while maintaining the same spatial and angular chirp characteristics as the original beam.

Chapter 3

Energy Scaling in PPLN Stacks

3.1 *Introduction*

Scaling up the output energy of PPLN systems without significantly degrading beam quality is critical if they are to be used for remote sensing applications. These systems require energies on the order of 100 mJ at a specified wavelength or wavelength range and beam quality relatively close to diffraction limited ($M^2 < 10$). Unfortunately, the low damage fluence limit for lithium niobate ($\sim 3 \text{ J/cm}^2$) constrains the energy output for PPLN devices to well below these values for typical pump beams. Recent experiments have shown the damage fluence limit can be increased by about a factor of three by coating the crystal surfaces with SiO_2 ,²⁷ but this increase alone is still not sufficient to support such high energies. For this reason, aperture scaling may be the most promising method to achieve higher energies in PPLN.

Increasing the size of the pump beam is a seemingly obvious way to lower fluence levels while allowing higher pump energies. However, the crystal aperture limits pump beam dimensions and attempts to fabricate PPLN crystals thicker than 1 mm have been unsuccessful. While not a problem for cw devices which typically focus the pump beam tightly to enhance nonlinear gain, this aperture limitation and the low damage fluence of lithium niobate has restricted pulsed PPLN devices to low-energy operation. The failure to fabricate thicker samples is primarily due to the large coercive field (21 kV/mm) required to pole congruently-grown lithium niobate. Applying the necessary coercive field to samples thicker than 1 mm causes dielectric breakdown of the crystal before poling can begin. Recent efforts to overcome the aperture limitation in pulsed PPLN systems have included pumping with elliptical beams^{27,41} and diffusion bonding stacks of PPLN crystals.⁴² In addition, 3-mm thick crystals of periodically poled RbTiOAsO_4 (PPRTA) and periodically poled KTiOPO_4 (PPKTP) have been successfully fabricated for

use in large aperture OPOs.^{43,44} The ability to pole thicker samples as well as the higher damage thresholds of periodically poled KTP isomorphs make them attractive for large pulse energies.

While increasing the aperture of QPM devices allows higher energy pulsed operation, it presents some challenges as well. Aperture and energy scaling experiments in pulsed monolithic PPLN OPOs have shown spectral broadening and serious beam quality degradation for pump beams greater than 300 μm in diameter.^{41,45} Similar effects were reported for large aperture OPOs in PPKTP.⁴⁴ For example, signal energies approaching 30 mJ have been demonstrated in PPLN systems by using elliptical pump beams. The elliptical beam takes advantage of the full aperture of the 1-mm thick crystal, but these systems suffered severe far field beam quality degradation with M^2 values on the order of 300.²⁷ While these signal energies are promising, the beam quality is much too poor for remote sensing applications.

One reason these problems arise is that, as discussed in §1.3, increasing the dimensions of the pump beam also increases the size of the gain volume in the nonlinear crystal for a given OPO cavity length (or a given interaction length for OPG). This, in turn, allows more noncollinear processes to see gain throughout the length of the material. Since each noncollinear process phase-matches at a different wavelength and propagates in a slightly different direction, this leads to spectral broadening and an increase in the overall far field divergence of the beam. As apertures are scaled to even larger dimensions, these effects will become more pronounced. In this chapter we demonstrate a method to achieve high signal energies while maintaining good beam quality.

3.2 Segmented Single-Grating and Multi-Grating PPLN Crystals

One method to combat the beam quality degradation that occurs due to aperture and energy scaling in OPG devices is the use of crystals with segmented gratings (see Figure 3.1). Recent experiments²⁷ have shown that such crystals have significantly better far field signal and idler beam properties than uniform grating crystals when pumped with large aperture beams. In a typical uniform grating crystal, increasing the size of the pump beam increases the size of the gain channel in the material. This, in turn, increases both the size of the near field signal and the number of signal propagation angles that overlap

field divergence of the signal increases and overall beam quality is degraded. By segmenting the grating of the crystal, the number of propagation angles that see gain is limited by the size of the grating segment as opposed to the size of the pump. This concept is illustrated in Figure 3.1. The segmentation of the grating essentially changes the near field output of an elliptically-pumped crystal from a single broadly divergent signal beam to multiple beams with low divergence. These multiple near field beams overlap in the far field to form a single beam with low overall divergence. This concept has only recently been demonstrated, but in that experiment the far field divergence of segmented grating crystals was almost five times smaller than that of uniform grating crystals.²⁷

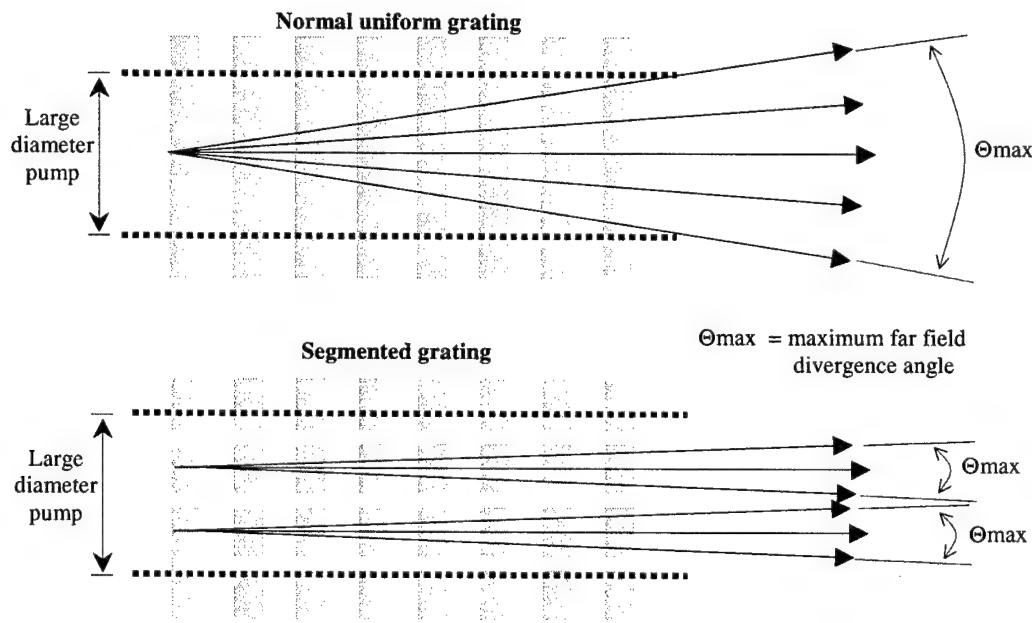


Figure 3.1 - Illustration of signal propagation directions which see gain for a single grating crystal (top) and a segmented-grating crystal (bottom). The illustration is for a single-pass OPG configuration.

As discussed by Missey in reference 27, there are two possible explanations for why segmenting the grating structure reduces parametric generation at large noncollinear angles for large aperture pump beams. The first explanation is that the spectral gain profiles of adjacent gratings do not overlap (i.e., wavelengths phase-matched in one grating are not phase-matched in adjacent gratings). Thus, photons generated in one segment no longer see gain if they propagate into adjacent gratings. This results in

maximum gain for photons (i.e., wavelengths) confined to one segment. In such cases, the maximum divergence angle is defined by the size of the grating (see Figure 3.1 bottom).

This explanation seems adequate for segmented multi-grating crystals where adjacent gratings are phase-matched for different signal-idler pairs, but beam quality improvement has been observed even in segmented single-grating crystals where adjacent gratings have identical periods (all gratings were in phase as well).²⁷ For these crystals, the spectral gain profiles of adjacent gratings were identical. Therefore, although spectral gain mismatch may play a role in the performance of multi-grating crystals, there must be some other mechanism contributing to the enhanced beam quality. The second possible mechanism outlined by Missey addresses this question.

The second explanation is that the segments themselves prevent photons from crossing between adjacent gratings. By placing the crystals in one leg of a Mach-Zender interferometer and illuminating them with a uniform beam, we were able to see that there is a distinct index of refraction change at the segments between gratings (see Figure 3.2). Since the segments are unpoled regions, this indicates that electric field poling causes a physical change in the crystal structure that leads to at least a slight change to the index of refraction. Although the images in Figure 3.2 were taken with a segmented multi-grating crystal, similar results were seen with segmented single-grating crystals.

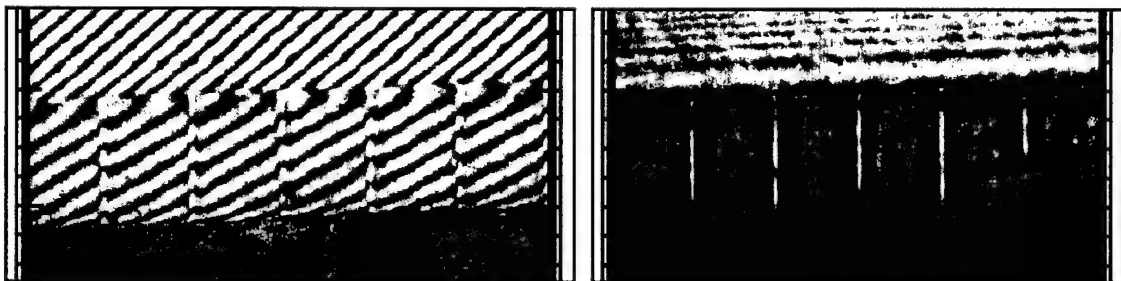


Figure 3.2 - Images of a segmented multi-grating crystal taken with an interferometer (left) and with single-beam illumination.²⁷ Fringe displacement in the left image and bright spots in the right image clearly indicate an index of refraction change at the segments between gratings.

The magnitude of the index difference between grating regions and segments is unknown; however, we can still make some general observations about the effects of the index change. For instance, if the index in the grating regions is higher than the index in the segments, then even an extremely small index change would be enough to cause total internal reflection of all noncollinear signal and idler beams generated by a $\lambda = 1.064 \mu\text{m}$

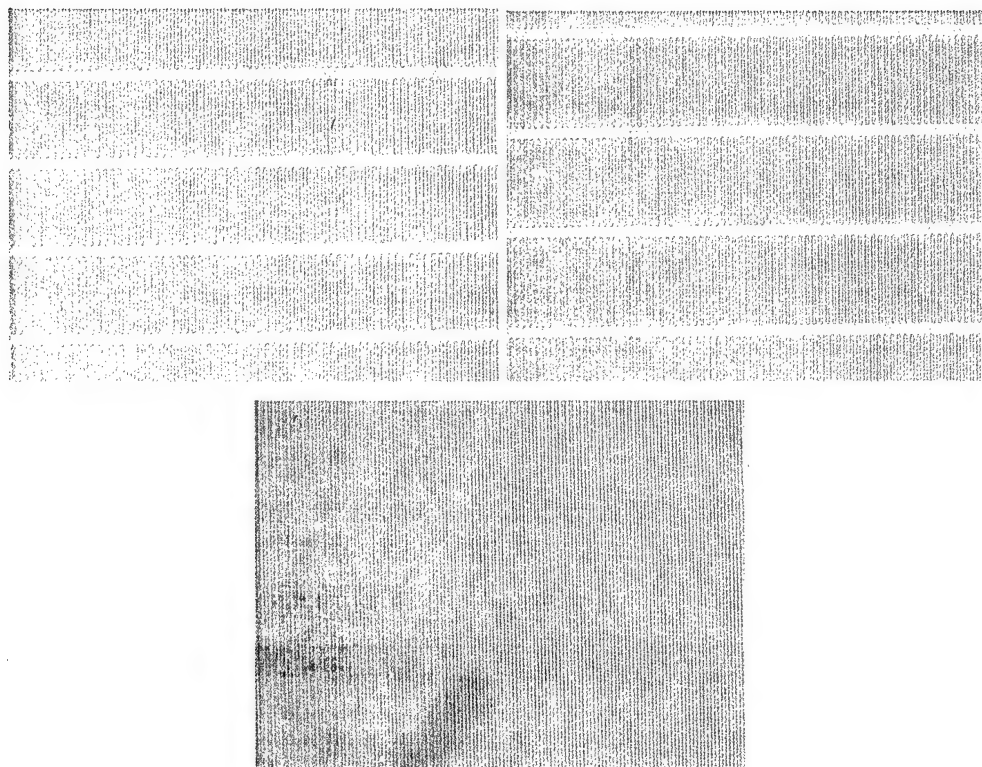


Figure 3.3 - Close-up images of the $+z$ surfaces of a segmented single-grating crystal (top left), segmented multi-grating crystal (top right), and single grating crystal (bottom) after a 10 minute HF etch.

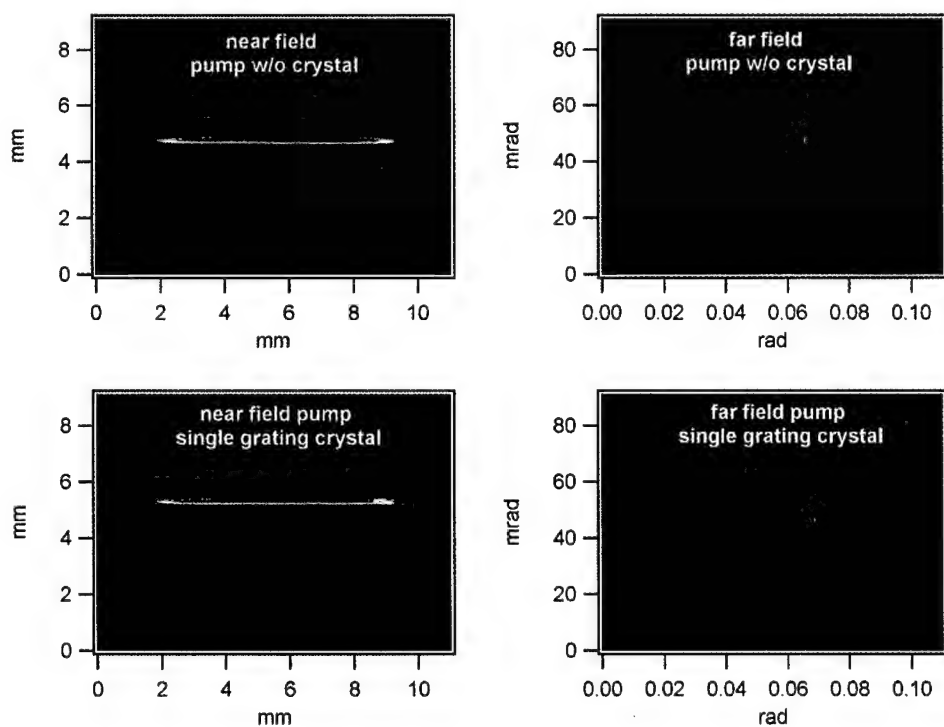


Figure 3.4 - (continued on next page)

internal reflection of all noncollinear signal and idler beams generated by a $\lambda = 1.064 \mu\text{m}$ pump. As an example, an index difference as small as 0.003 would be enough to achieve total internal reflection for all possible signal-idler pairs that can be generated in a 29.75- μm grating period PPLN crystal pumped at $\lambda = 1.064 \mu\text{m}$. Furthermore, since beams undergo a phase shift during total internal reflection, the reflected beams would no longer maintain the relative phase relationship with the pump that is needed to see further gain. If the index is smaller in the grating regions than the index in the segments, the noncollinear beams would not be totally reflected but would still lose some energy to reflection at the interface. The net effect in either case is similar to that described in the first explanation and illustrated in Figure 3.1 - that maximum gain occurs for collinear and slightly noncollinear beams that propagate through the crystal without intersecting the segments. This reduces the maximum far field divergence for beams generated in each grating segment and thus for the overall beam as well.

To experimentally investigate these concepts, we fabricated 0.5-mm x 12-mm x 50-mm (thickness x width x length) uniform grating, segmented multi-grating, and segmented single-grating crystals and pumped them with the elliptical pump setup described in Figure 2.9. Images of the crystals are presented in Figure 3.3. Although the crystals were not specifically polished with monolithic endfaces, measurements made after polishing indicated that the endfaces were indeed close to plane-parallel. The single-grating and segmented single-grating crystals had a 29.75- μm grating period and the segmented multi-grating crystal had 25 grating periods ranging from 25- μm to 31.25- μm in 0.25- μm increments. Individual gratings on the segmented single-grating crystal were 350 μm wide and separated by 50 μm . All gratings were in phase (i.e., poled/unpoled regions in adjacent gratings were aligned) as can be seen from the image in Figure 3.3. The gratings on the segmented multi-grating crystal were 400 μm wide and separated by 50 μm . Since adjacent gratings had different periods, they were not in phase. Figure 3.4 shows images of the pump beam through each of these crystals. It is clear from the images of the segmented crystals that the pump beam is also segmented as it propagates through the crystals due to index of refraction variations at the segments in the grating structure.

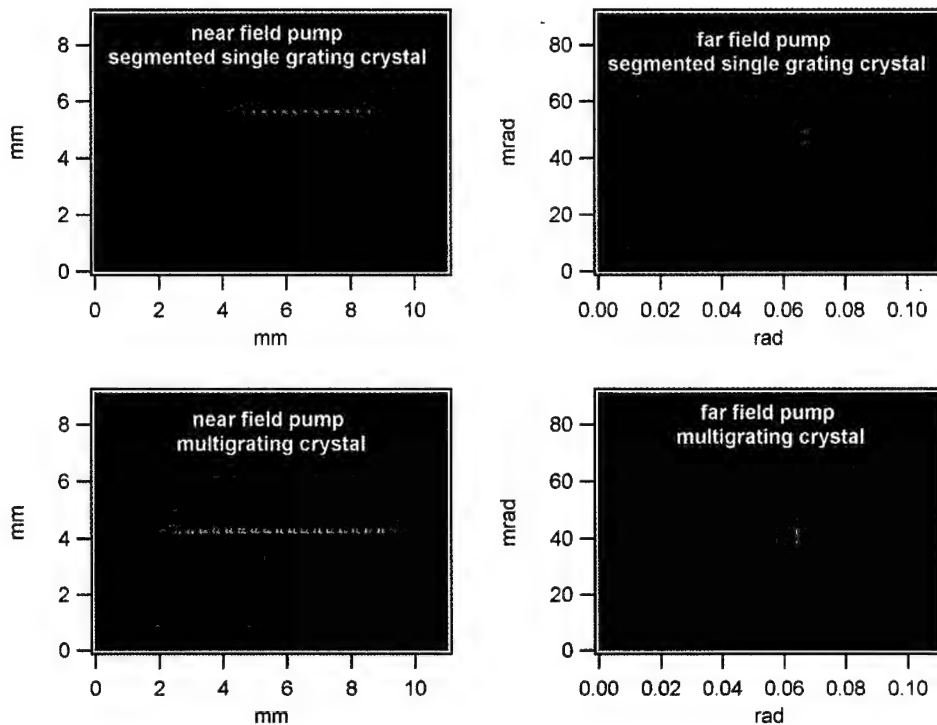


Figure 3.4 - Near field (left) and far field (right) images of the pump beam with no crystal present (top row), through a single grating crystal (second row from top), through a segmented single-grating crystal (third row from top), and through a segmented multi-grating crystal (bottom row).

As shown in Figure 3.5, all three crystals reached threshold at a pump energy of ~ 2 mJ and produced similar signal energy output as pump energy was increased. The slightly lower output energies of the single-grating crystal may be due to noncollinear beams competing for gain at higher pump energies.

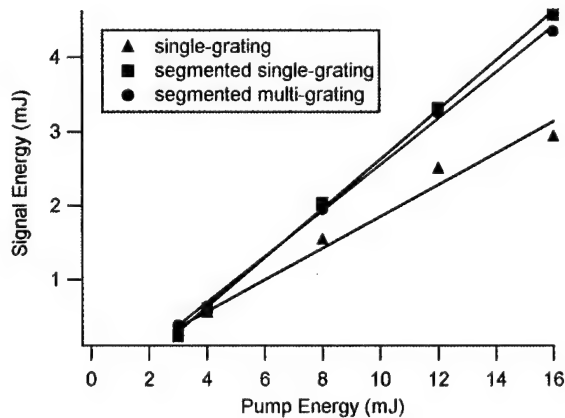


Figure 3.5 - Signal energy vs pump energy for single-grating, segmented single-grating, and segmented multi-grating crystals.

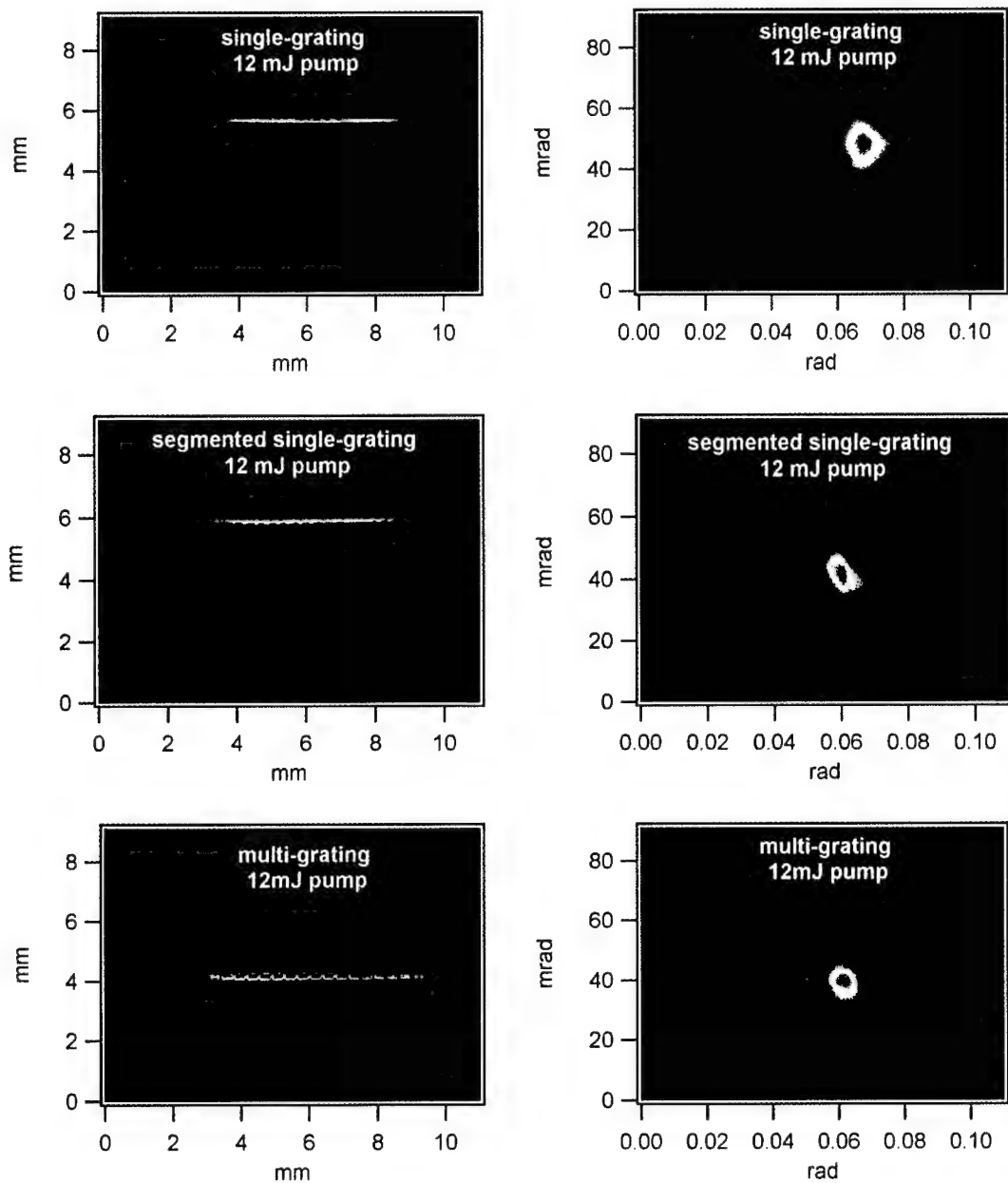


Figure 3.6 - Near field (left column) and far field (right column) images of the signal beam generated by a single-grating crystal (top row), segmented single-grating crystal (middle row), and a segmented multi-grating crystal (bottom row). All images were taken for 12 mJ of pump energy.

Although the far field signal beams for each crystal looked roughly similar, their propagation characteristics revealed that the beam quality produced by the segmented crystals was significantly better than that of the single-grating crystal. At 16 mJ of pump, the M^2 values were measured to be ~ 3.7 for the single-grating crystal, ~ 1.75 for the segmented single-grating crystal, and ~ 1.7 for the multi-grating crystal. It should be noted

that the M^2 improvement for the segmented crystals was not as large as the factor of ~ 5 improvement reported by Missey. However, the endfaces of the crystals used in his experiments were wedged to force OPG operation. Since our crystals were operating in monolithic OPO mode, their M^2 values were already much improved over typical M^2 values for similar OPG devices (and those reported by Missey). Near field and far field images of the signal beams generated by each type of crystal when pumped at 12 mJ are given in Figure 3.6.

As with the elliptical pumping experiments discussed in §2.5, the single grating crystal initially operated in collinear monolithic OPO mode, but began to generate degenerate noncollinear OPG output at a pump energy of ~ 6 mJ. A somewhat unexpected result was that the segmented single-grating and segmented multi-grating crystals also produced degenerate noncollinear beams at higher pump energies of ~ 10 mJ and ~ 16 mJ respectively. The angles for the noncollinear beams were $\pm 2.6^\circ$ with respect to the pump beam. The fact that the noncollinear output occurred at higher pump energies indicates that the noncollinear processes are at least somewhat suppressed in the segmented crystals. However, the fact that any noncollinear output was generated indicates that the beams are not experiencing total internal reflection at the interfaces.

The segmented single-grating crystal presents an interesting question. Since adjacent gratings have identical periods that are in phase (i.e., aligned with) one another, will the beams generated in adjacent gratings be mutually coherent or does each grating act as an independent source that is not coherent with other gratings? A case can be made for either result. On one hand, the same pump beam is driving the parametric generation process in each grating. Since a proper relative phase relationship between the pump, signal, and idler must be maintained for efficient generation, this leads to the conclusion that the beams generated in each grating should be mutually coherent. On the other hand, the parametric generation process starts from noise (i.e., signal and idler photons with random phase and velocity). Thus, the same pump beam could drive multiple, independent parametric processes that were generated from noise with differing initial phase characteristics. These beams would then be mutually incoherent.

To experimentally investigate this question, we compared the near and far field characteristics of signal beams generated when one, two, or many individual gratings on the segmented single-grating crystal were illuminated. We used the same elliptical pumping setup described above, but added an aperture to reduce the transverse size of the pump beam before the crystal. As shown in Figure 3.7, there is no significant difference in the far field signal beam generated by a single grating versus the beam generated by many gratings. There also did not appear to be any interference between beams generated by adjacent gratings when two or more gratings were illuminated. These initial results indicate that each grating acts independently and the beams generated by multiple gratings are not mutually coherent. However, further investigation of this question is certainly warranted.

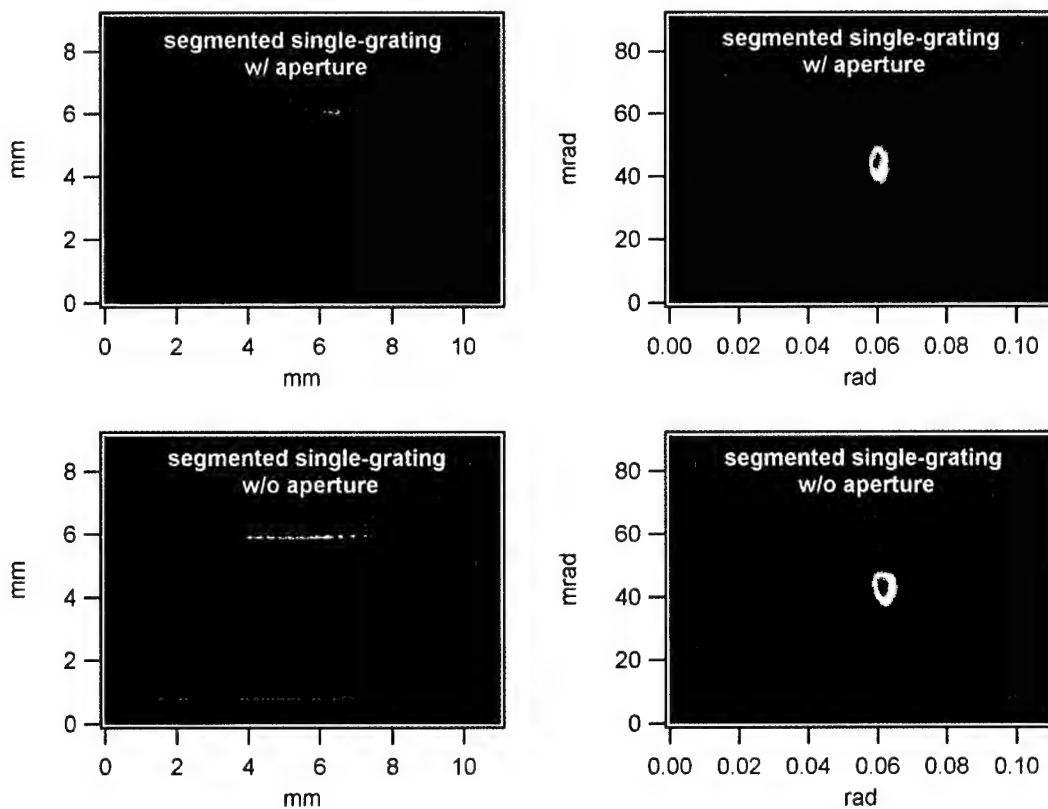


Figure 3.7 - Near field (left column) and far field (right column) images of the signal beam generated by the segmented single-grating crystal with one grating illuminated (top row) and with multiple gratings illuminated (bottom row). For all images the total pump energy was 8 mJ.

3.3 Seeded Grating Crystals

In addition to segmenting of grating structures, we proposed another grating design in hopes of improving the beam quality of large aperture pumped devices. In this design (shown in Figure 3.8), poled regions of extremely small transverse width lead into a uniformly poled region. The idea behind the design is that these narrow regions will generate collinear signal energy with very limited noncollinear components (and thus excellent far field divergence properties). This signal energy would then be used to seed the parametric generation process in the uniform grating region and generate a high quality signal beam. The uniform grating region is necessary because the area between narrow seed regions does not efficiently use the pump. This concept is very similar to a common practice used in semiconductor laser design in which narrow "flare" regions are used to seed the lasing process.

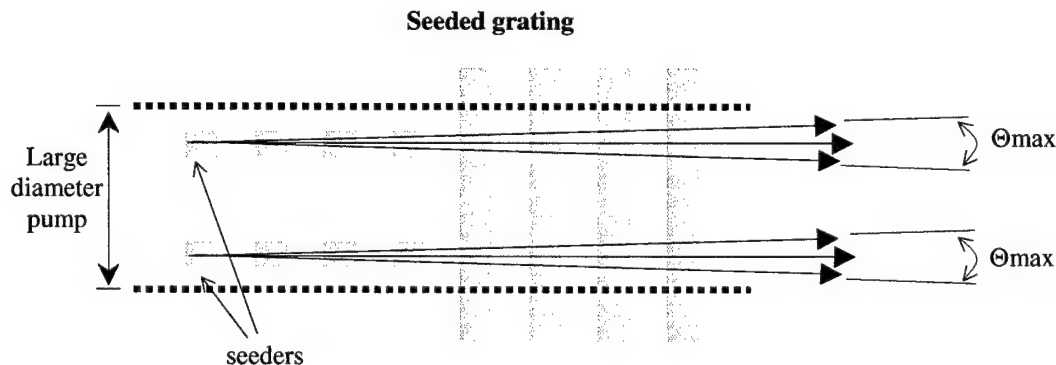


Figure 3.8 - Illustration of signal propagation directions which see gain for a seeded grating crystal. The illustration is for a single-pass OPG configuration.

Using standard electric field poling techniques,¹⁰ we fabricated two 0.5-mm x 10-mm x 50-mm (thickness x width x length) crystals with 50- μ m wide by 25-mm long seed regions feeding into a 25-mm long uniform grating region of the same period. The seed regions were separated by 450 μ m on one crystal and by 50 μ m on the other crystal. As shown in Figure 3.9, both the seed regions and the uniform grating regions showed good poling fidelity.

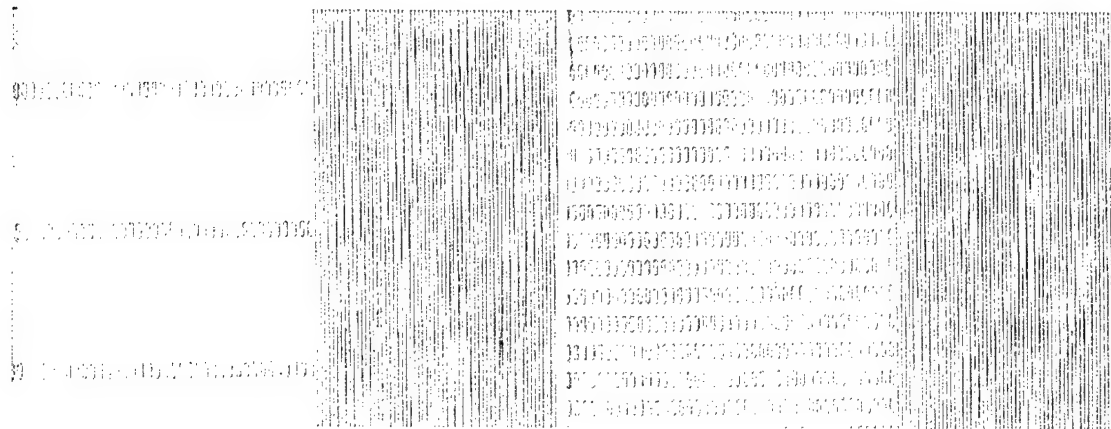


Figure 3.9 - Close-up images of regions of a seeded-grating crystal with 450- μm seeder spacing (left) and seeded-grating crystal (right) with 50- μm seeder spacing after a 10 minute HF etch.

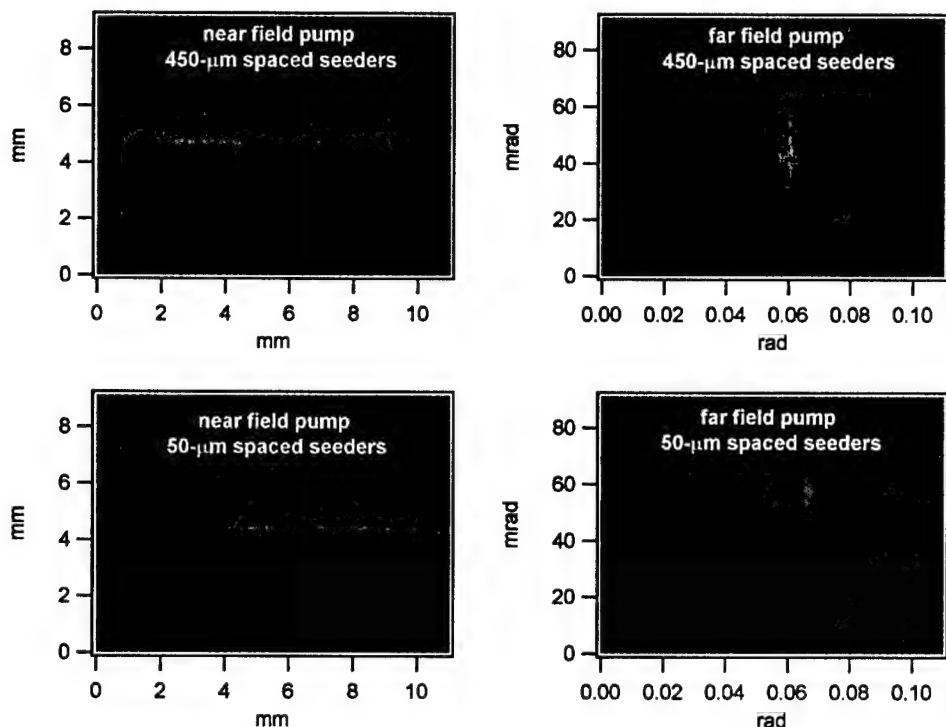


Figure 3.10 - Near field (left column) and far field (right column) images of the pump beam after propagation through a seeded grating crystal with 450- μm spaced seeders (top row) and after propagation through a seeded grating crystal with 50- μm spaced seeders (bottom row).

We again used the experimental setup described in Figure 2.9 to elliptically pump the seeded grating crystals. As with the segmented grating crystals, images of the pump beam after propagation through the seeded grating crystals show that the seeders either guide or segment the pump beam (see Figure 3.10) as it propagates through the crystal.

Although the segmentation is hard to resolve in the image of the 50- μm spaced seeders, it was clearly visible during the experiment.

Both the crystal with the widely spaced seeders and the crystal with the closely spaced seeders reached threshold at ~ 2 mJ of pump energy and produced signal energies of ~ 4.5 mJ when pumped at 16 mJ. These thresholds and signal energies are consistent with those demonstrated by the segmented and single grating crystals of §3.2. However, the far field signal beam quality of both seeded grating crystals was significantly different than that of the segmented grating crystals. Furthermore, the widely spaced seeded grating crystal produced significantly different results than the crystal with closely spaced seeders. For the crystal with 450- μm spaced seeders, Figure 3.11 shows that even at low pump energies there was structure similar to interference fringes in the far field signal beam. As the pump energy was scaled to higher levels, the overall far field divergence increased with increasing energy and the interference structure remained. It is significant to note that there were no noncollinear beams generated even at high pump energies. This indicates that the seeded grating succeeded in encouraging collinear operation.

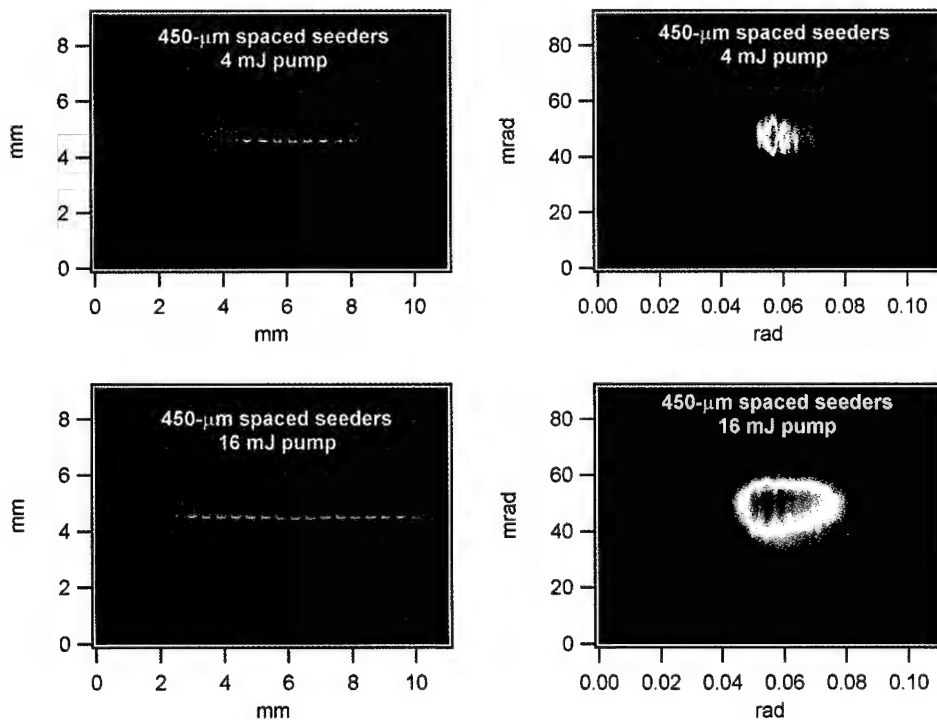


Figure 3.11 - Near (left column) and far field (right column) signal beam images produced by a seeded grating crystal with 450- μm spaced seeders when pumped at 4 mJ (top row) and 16 mJ (bottom row).

To determine if the structure observed in the far field signal beam was truly interference, we placed an aperture in the pump beam before the PPLN crystal. We narrowed the aperture until the pump beam was illuminating only one seeder and looked at the far field signal beam. We then opened the aperture to illuminate two seeders and compared the far field signal to that produced by a single seeder. The results, presented in Figure 3.12, show that there is no interference-like structure on the far field beam generated by one seeder, but the structure does appear on the signal beam generated by two seeders. This indicates that the beams produced by the 450- μm spaced seeders are coherent and interfering with each other in the far field.

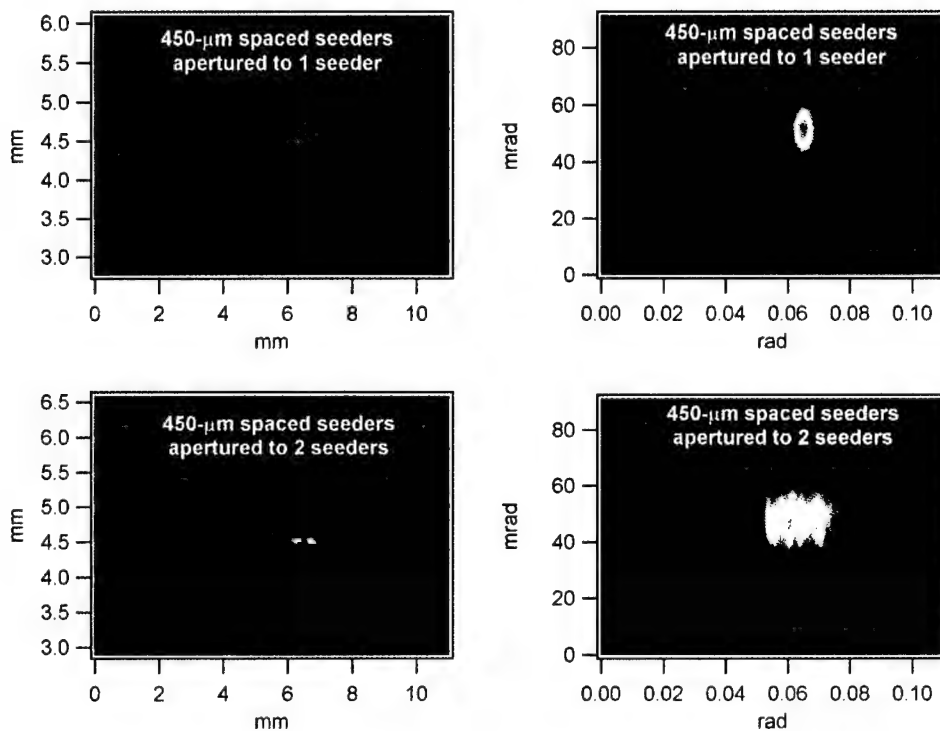


Figure 3.12 - Near field (left column) and far field (right column) images of the signal beam produced by a seeded grating crystal with the pump beam apertured to illuminate one seeder (top row) and two seeders (bottom row). The overall pump energy was ~ 4 mJ for the measurements.

The near and far field signal beams generated by the crystal with 50- μm spaced seeders are shown in Figure 3.13. The images show that the profile of the near field signal beam mirrors that of the near field pump beam, but the far field signal beam was broadly diverging and contained hot spots at seemingly random locations. These hot spots remained at both low and high pump energies. We were unable to perform the same

aperture experiments conducted on the 450- μm spaced seeded grating crystal because the extremely close (50- μm) spacing of adjacent seeders prevented reduction of the pump to an aperture small enough to illuminate a single seeder. Thus, the cause of the strange far field signal beam characteristics is currently unknown.

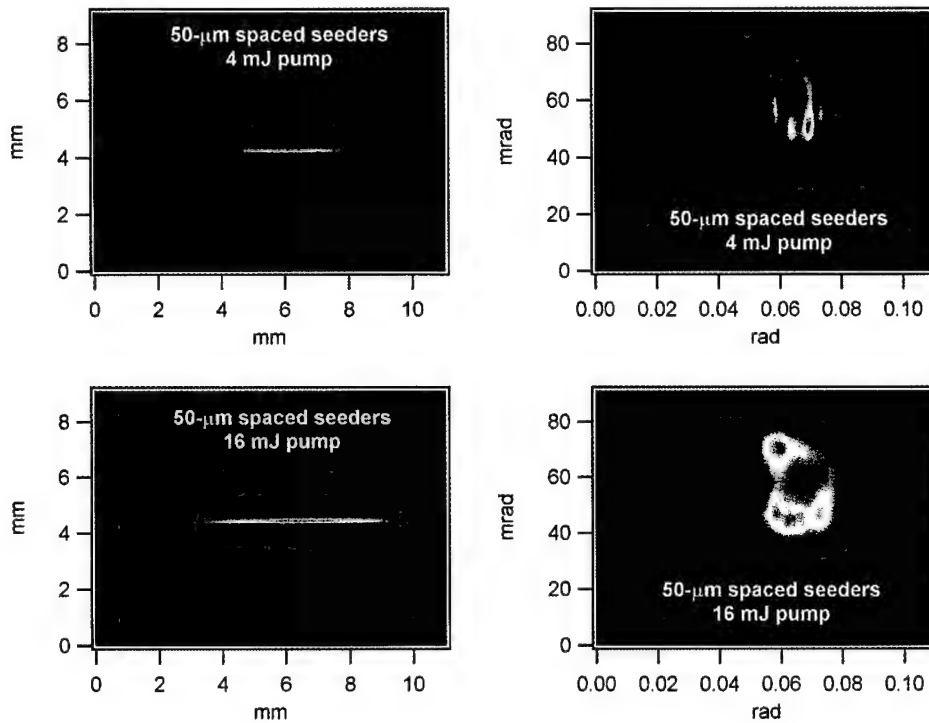


Figure 3.13 - Near (left column) and far field (right column) signal beam images produced by a seeded grating crystal with 50- μm spaced seeders when pumped at 4 mJ (top row) and 16 mJ (bottom row).

It was clear from our initial experiments that the seeded grating crystals we tested did not achieve the good far field signal beam quality we desired, so we did not pursue them further. However, the results indicate that the seeder regions on the crystals do in fact seed the parametric process. As this capability may be useful in other applications, further investigation of seeded grating crystal designs and detailed characterization of their performance is warranted.

3.4 Stacks of Segmented Multi-Grating Crystals

The experiments from §3.2 show that segmenting the grating structure allows aperture scaling, and therefore energy scaling, in the horizontal direction while maintaining good far field signal beam characteristics. However, this does not address the

problem of energy scaling in the vertical dimension. Note that we refer to the transverse width of the crystal as the horizontal dimension and the thickness (direction along which the poling field was applied) of the crystal as the vertical dimension. As mentioned previously, the large coercive field of lithium niobate limits fabrication of PPLN crystals to a maximum thickness of \sim 1 mm, which thereby limits the maximum size of the pump beam in the vertical dimension. Furthermore, even if thicker PPLN samples could be poled they would still suffer beam quality degradation and spectral broadening due to aperture scaling effects in the vertical direction. Stacking together multiple PPLN crystals presents an alternative way to fabricate thicker overall crystal apertures and provide vertical segmentation of the gratings as well.

One of the major problems with stacking PPLN crystals is that while the seams between the crystals provide vertical segmentation, they also corrupt the pump beam and lead to crystal damage at low fluence levels. Since there is inevitably a small air gap in the seams between crystals, this beam corruption is more significant than that caused by segmenting in the horizontal direction due to the large index of refraction change at the air-crystal interface. For example, in one of our early experiments we simply stacked three 1-mm thick PPLN crystals by placing them in optical contact and illuminated them with a large aperture pump beam. Although the crystals reached OPG threshold, they damaged near the crystal seams at pump energies only slightly above threshold and well below typical damage fluence levels. For this reason, we decided to pursue diffusion bonding of segmented grating crystals in hopes of reducing or eliminating the effects of the seams between crystals.

To this end, we diffusion bonded eight 0.5-mm x 10-mm x 25-mm (thickness x width x length) segmented multi-grating crystals to form a single 4-mm thick by 10-mm wide crystal. We chose segmented multi-grating crystals because they exhibited the best far field beam quality in the experiments of §3.2. To diffusion bond the crystals, we chemically cleaned each individual crystal and placed them in optical contact. We then clamped them together and heated the stack at 900 °C for 12 hours. The result was a single 4-mm thick by 10-mm wide crystal with 200 horizontally and vertically segmented gratings.

To investigate the properties of the diffusion-bonded stack prior to experiment, we placed the stack in one arm of a Mach-Zender interferometer and examined its fringe characteristics. The resulting interferogram, shown in Figure 3.14, revealed that the diffusion bonding process imposed severe internal strains on the stack due to lattice mismatch across the seams between individual crystals. We then placed the stack in the experimental setup and pumped it with an ~8-mm (width) by ~3.5-mm (height) pump beam. However, the index of refraction variation due to the internal strain caused significant pump corruption as the beam propagated through the stack. This, in turn, led to hot spots in the pump beam and severe crystal damage before the stack reached OPG threshold.

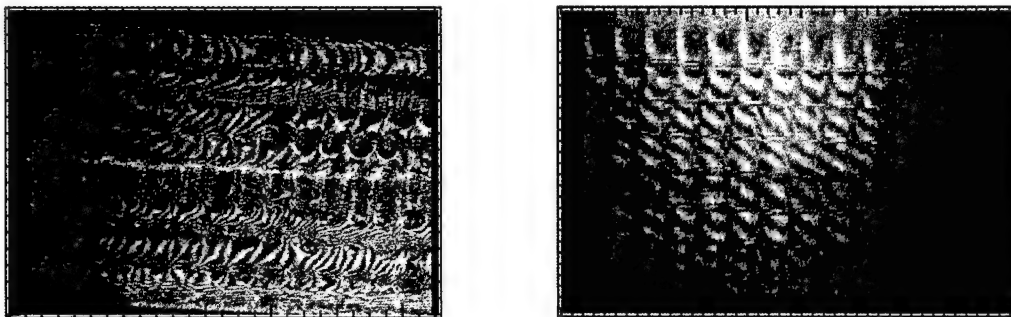


Figure 3.14 - Interferographic images of diffusion bonded (left) and waxed (right) stacks of multi-grating crystals. The distorted fringe patterns in the image of the diffusion bonded stack indicate severe internal strain while parallel fringes in the waxed stack indicate there is little internal strain.

To avoid both the problems caused by internal strain in the diffusion bonded stacks and the negative effects of seams between the optically contacted stacks, we proposed a twofold solution. First, we would stack multiple segmented grating crystals and simply cement them together with an epoxy. Since the crystals would not be atomically bonded, this would eliminate the severe internal strain caused by diffusion bonding. Second, we devised two novel pumping schemes that would simultaneously pump each crystal in the stack with an elliptical beam. Since each elliptical beam can pass cleanly through an individual crystal, this technique avoids the pump beam corruption caused by seams between the crystals.

For the first part of the solution, we fabricated eight 0.5-mm x 10-mm x 25-mm (thickness x width x length) segmented multi-grating crystals and stacked them to form a single 4-mm thick by 10-mm wide crystal. The input and exit faces of the crystals were uncoated (i.e., bare lithium niobate). Instead of diffusion bonding the stack we simply used a high-temperature wax to bond the crystals together. As shown by the interferogram of this stack in Figure 3.14, this method of bonding successfully avoided the severe internal strain caused by diffusion bonding.

For the second part of the solution, we tested two techniques to simultaneously generate multiple elliptical pump beams. One method proposed was to use a reflective variable attenuator to produce multiple copies of an elliptical pump beam (see Figure 3.15 below). The problems with this method were that variable attenuators with the proper intensity distribution and sufficient damage resistance were unavailable and it was also extremely difficult to get the pump beam into the reflector-mirror assembly when it was aligned with the proper spacing. For these reasons, we chose to more aggressively pursue the second pumping scheme. This method consisted of using a cylindrical microlens array to divide the pump beam into multiple elliptical beams of equal intensity (see Figure 3.15). Although this method required the purchase of an expensive custom designed lens array, it was much easier to align and led to a less complicated and more efficient system.

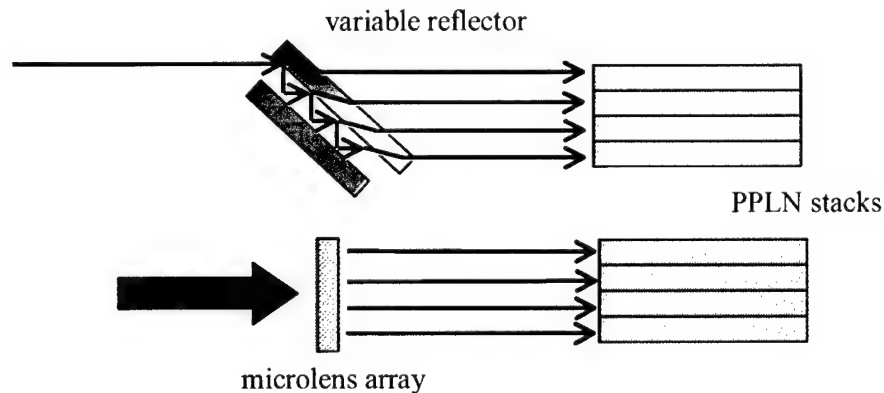


Figure 3.15 - Pumping schemes for PPLN stacks utilizing a variable density filter (top) and a microlens array (bottom) to convert a single pump beam into multiple beams.

To perform our experiments, we acquired a 7-mm x 7-mm (width x height) lens array with 14 cylindrical lenslets separated by 0.5-mm center to center. The focal length of each lenslet was ~50 mm and the front and back surfaces of the array were

antireflection coated for $1.064 \mu\text{m}$. Over the course of our experiments we used two slightly different experimental setups. We initially used the experimental setup described in Figure 3.16 to image a tophat profile pump beam from the Coherent Infinity laser onto the lens array. Actual pictures of the setup are shown in Figure 3.17 and Figure 3.18. The resulting pump beam, shown in Figure 3.19, consisted of multiple $\sim 5\text{-mm} \times 0.350\text{-mm}$ elliptical beams separated by $\sim 0.5 \text{ mm}$. By taking a vertical slice across the intensity profile of the pump (also shown in Figure 3.19), we determined that the eight central beams had roughly equal intensities. Finally, the top right image in Figure 3.19 shows that the pump beam passed cleanly through the crystal stack. Note, however, that since there are only eight crystals in the stack and more than eight pump beams, some pump energy is lost. Future experiments could utilize this pump energy by fabricating larger PPLN stacks with more crystals.

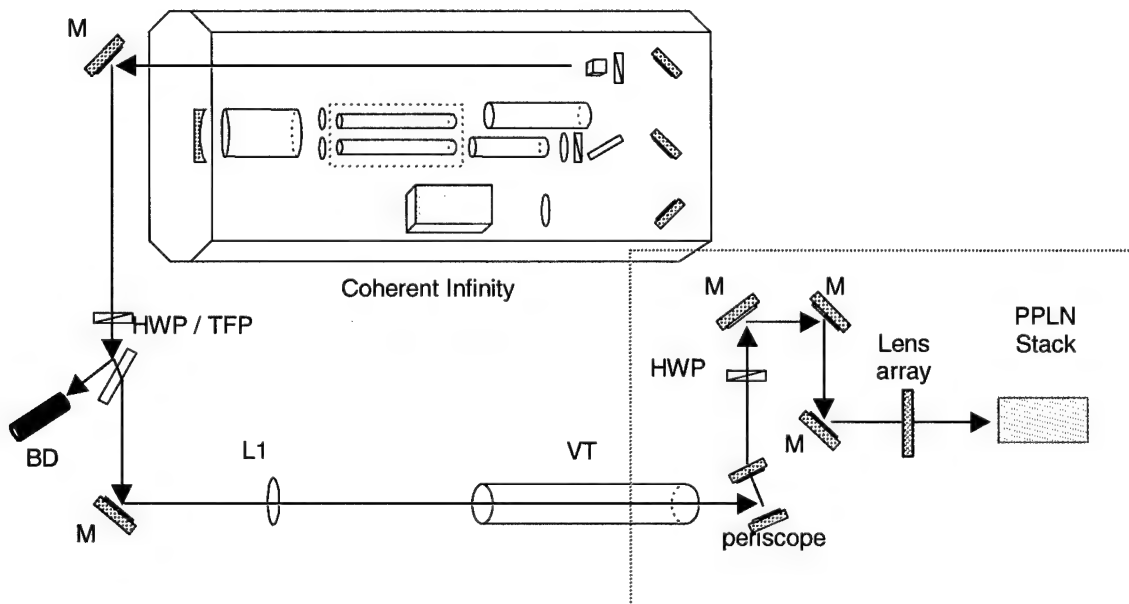


Figure 3.16 - Initial setup for PPLN stack experiments. The dashed blue line denotes the area that is pictured in Figure 3.17. M = high reflectivity mirror coated for $1.064 \mu\text{m}$, HWP = half wave plate, TFP = thin film polarizer, BD = beam dump, VT = vacuum tube, L1 = 1000mm focal length lens.

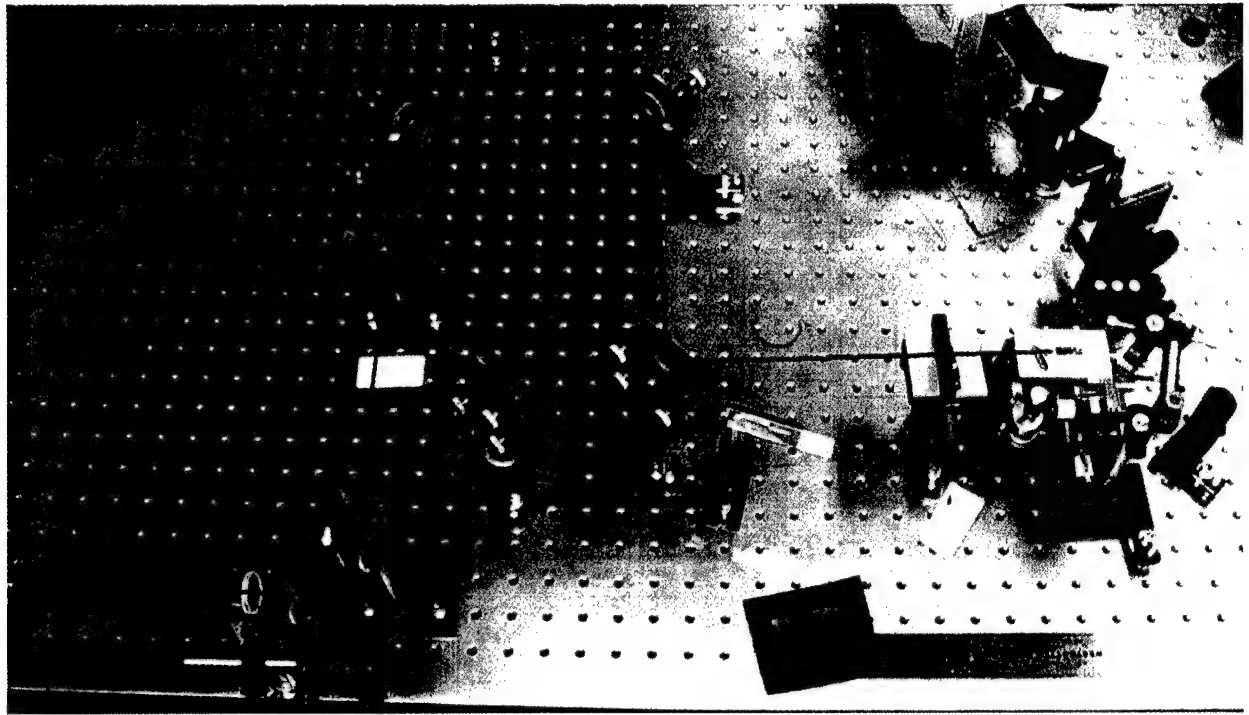


Figure 3.17 - Picture of the initial experimental setup for the PPLN stack experiments. The red line indicates the path of the pump beam.

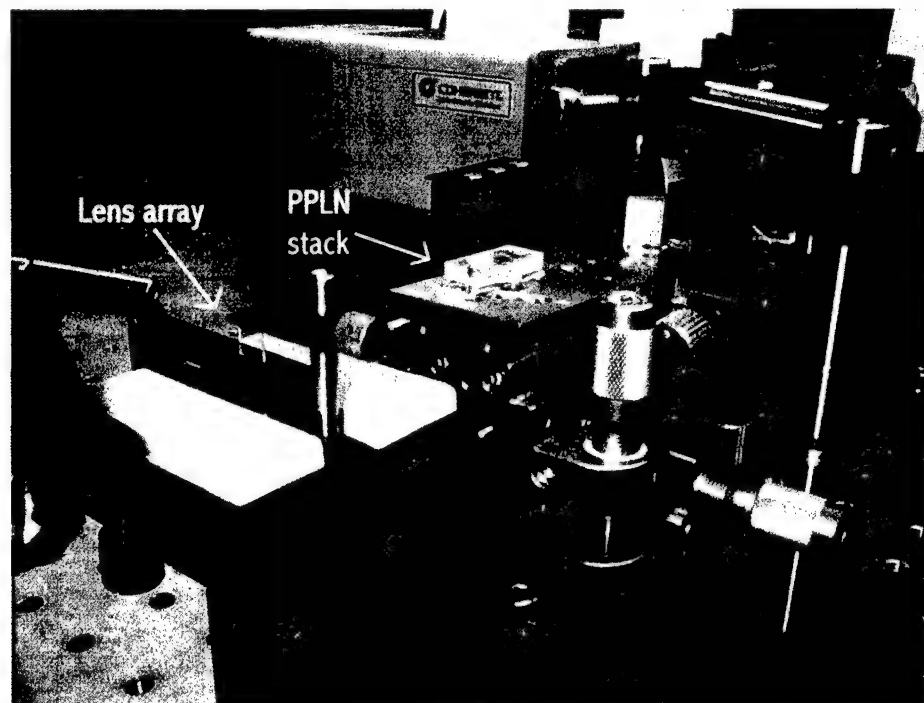


Figure 3.18 - Close-up picture of the lens array and the stack of eight 1/2-mm thick multi-grating crystals.

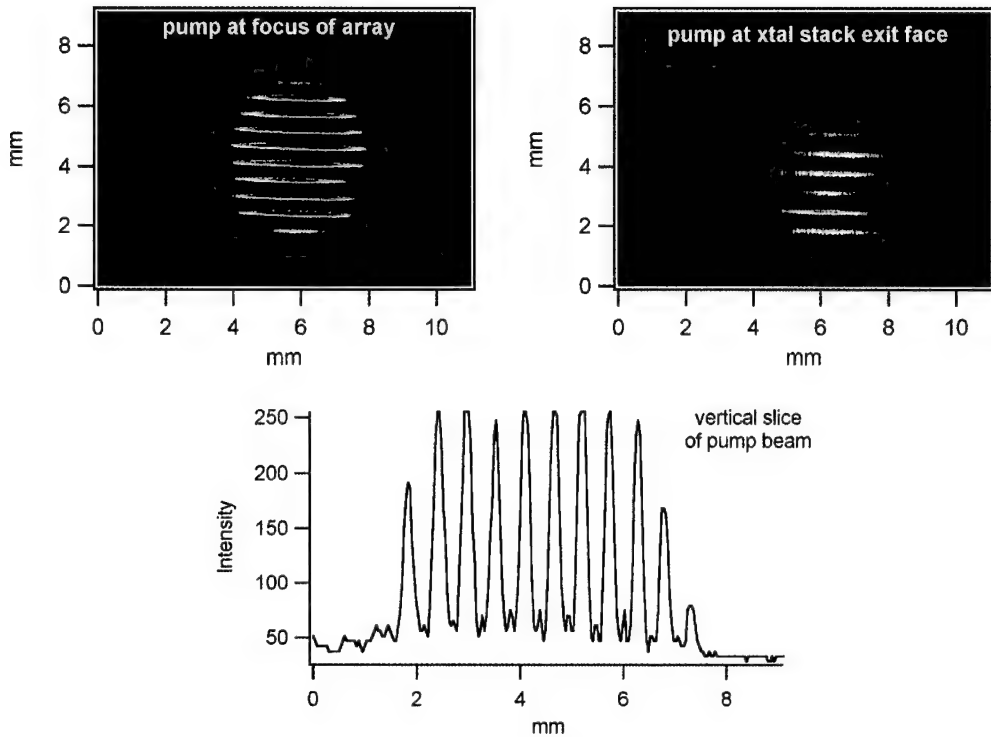


Figure 3.19 - Images of the pump beam at the focal plane of the cylindrical lens array (top left) and after passing through a stack of eight 1/2-mm thick crystals (top right). The bottom plot was produced by taking a vertical slice across the intensity profile in the top left image.

When pumped with the configuration shown in Figure 3.16, the crystals in the stack began to reach OPG threshold at \sim 16 mJ of pump energy. As is obvious from the top left image of Figure 3.22, not all crystals reached threshold at the same time. This was likely caused by a combination of factors, including variation in poling quality and variation in single pass gain for gratings phase-matched at different wavelengths (recall the discussions of §1.3). As pump energy was increased, the rest of the gratings quickly turned on and produced the output spectra shown in Figure 3.20. Note that all of the eight multi-grating crystals were fabricated with the same 25 grating periods, so they produced only the 17 spectral bands shown in the figure (not all gratings were illuminated, thus there are not 25 lines). However, by simply stacking crystals with different grating periods we could generate up to 200 distinct spectral bands with only eight crystals. Conversely, by making all gratings with the same period, it is possible to consolidate all signal energy into a single spectral line.

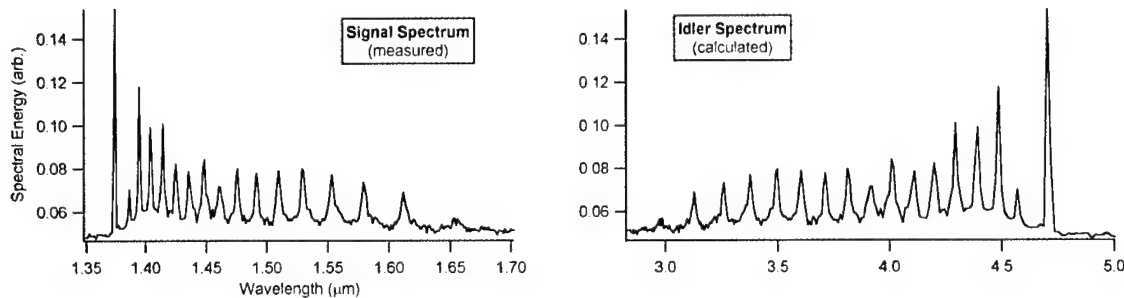


Figure 3.20 - Signal spectrum (left) and idler spectrum (right) generated by the stack of segmented multi-grating crystals. The signal spectrum was measured directly using a monochromator and linear array. The linear array could not detect idler wavelengths, so the idler spectrum was calculated from the signal and pump wavelengths.

We pumped the crystals with pump energies of up to 80 mJ (see Figure 3.21) and generated 19 mJ of signal energy at that pump level. This is extremely high signal output for uncoated lithium niobate and these signal energies correspond to an overall conversion efficiency of ~ 46 percent. Note that this conversion efficiency includes only the pump energy which actually illuminated the crystal stack (i.e., it does not include the extra beams produced by the array). We observed exceptional far field beam quality at all energy levels and measured M^2 values between 1.5 and 1.9. The signal images of Figure 3.22 show the excellent far field beam quality.

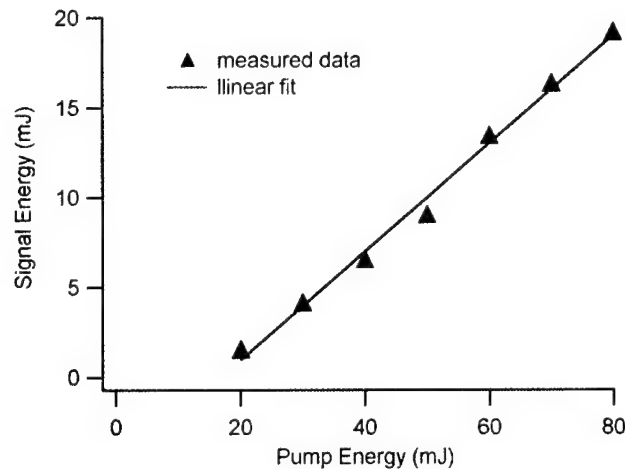


Figure 3.21 - Output signal energy versus pump energy for the PPLN stack in the initial experimental setup.

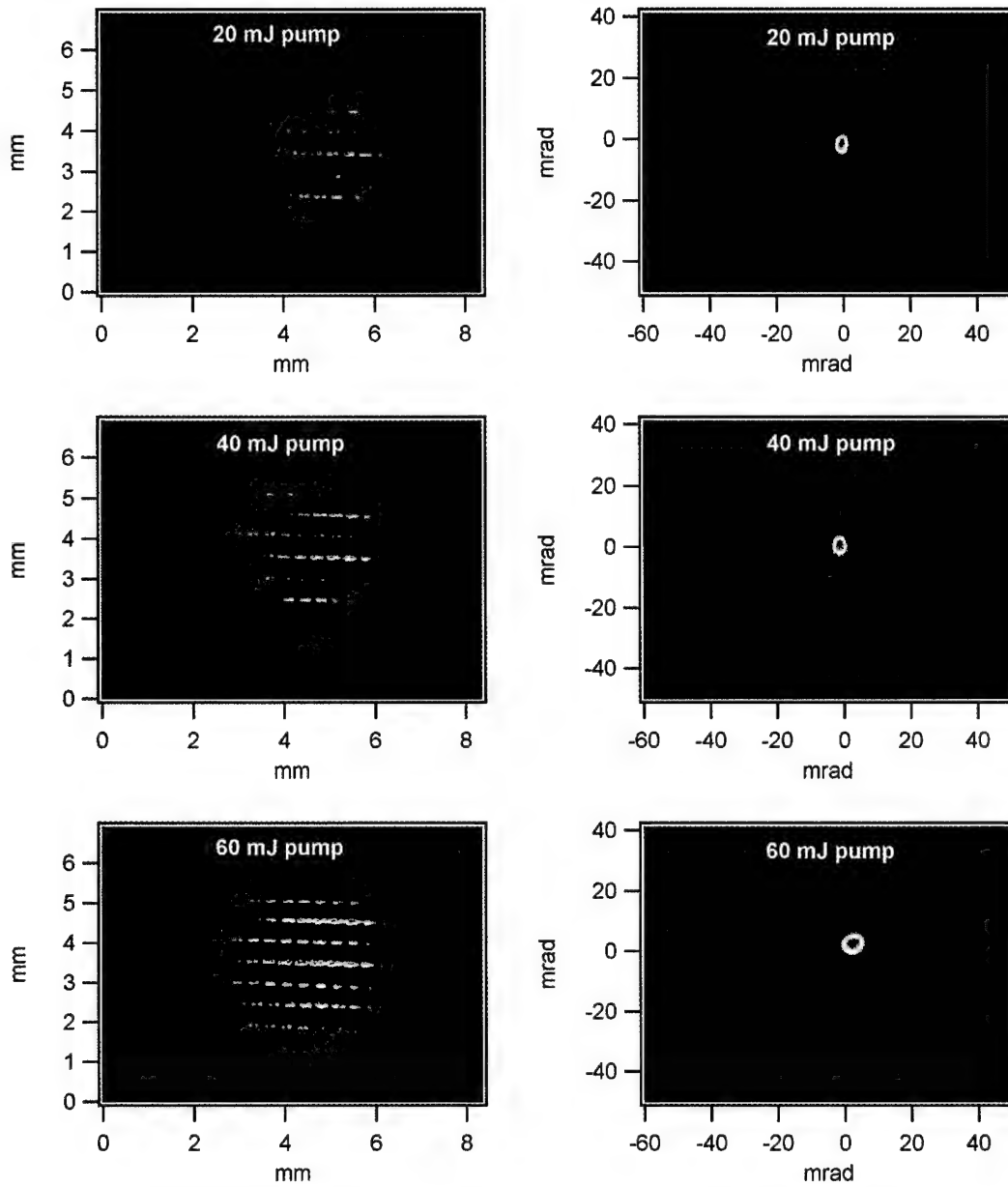


Figure 3.22 - Near field (left column) and far field (right column) signal images produced by the stack of eight 1/2-mm thick PPLN crystals when pumped at 20 mJ, 40 mJ, and 60 mJ.

We did not pump the crystals above 80 mJ in this experimental setup because the windows on the vacuum tube used for relay imaging began to damage at energies above 80 mJ. To overcome this problem, we adjusted the setup and used shorter focal length imaging lenses to increase the diameter of the pump beam at the windows of the vacuum tube. This allowed higher pump energies without reaching damage fluence levels for the windows. The revised experimental setup is shown in Figure 3.23. The pump beam in the

revised setup was similar to that of the initial setup, but the energy distribution among individual elliptical beams was not as equally divided (see Figure 3.24).

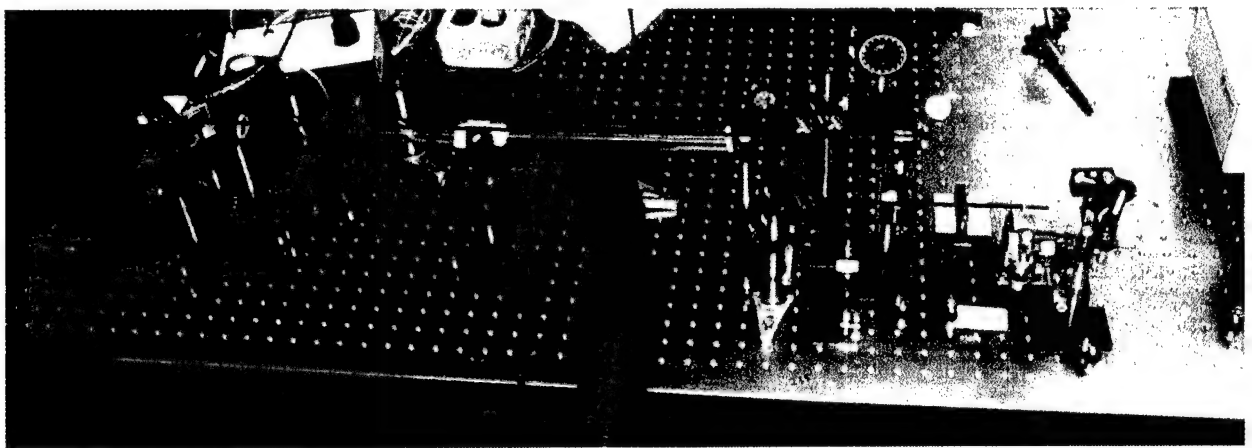
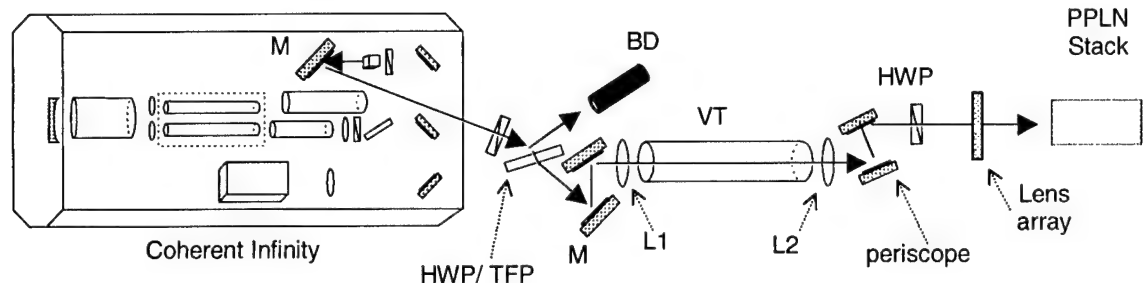


Figure 3.23 - Schematic (top) and picture (bottom) of the revised setup for PPLN stack experiments. The red line in the bottom picture illustrates the path of the pump beam. M = high reflectivity mirror coated for 1.064 μ m, HWP = half wave plate, TFP = thin film polarizer, BD = beam dump, VT = vacuum tube, L1 = 250mm focal length lens, L2 = 280mm focal length lens.

We repeated the signal output versus input pump energy measurements performed with the previous experimental setup and obtained similar results (see Figure 3.25). However, with the revised setup we were able to pump at energies up to 150 mJ without crystal damage. The maximum signal output measured was 33 mJ at 150 mJ of pump energy. To our knowledge, this is by far the highest signal energy ever generated in uncoated PPLN crystals. The picture of Figure 3.26 shows the visible red light output when the crystal was pumped at 140 mJ. The red is generated by a parasitic sum frequency generation (SFG) process between the pump and the signal wavelengths. Although it is a parasitic process, the strength and shape of the SFG beam are often good indicators of the shape and strength of the signal.

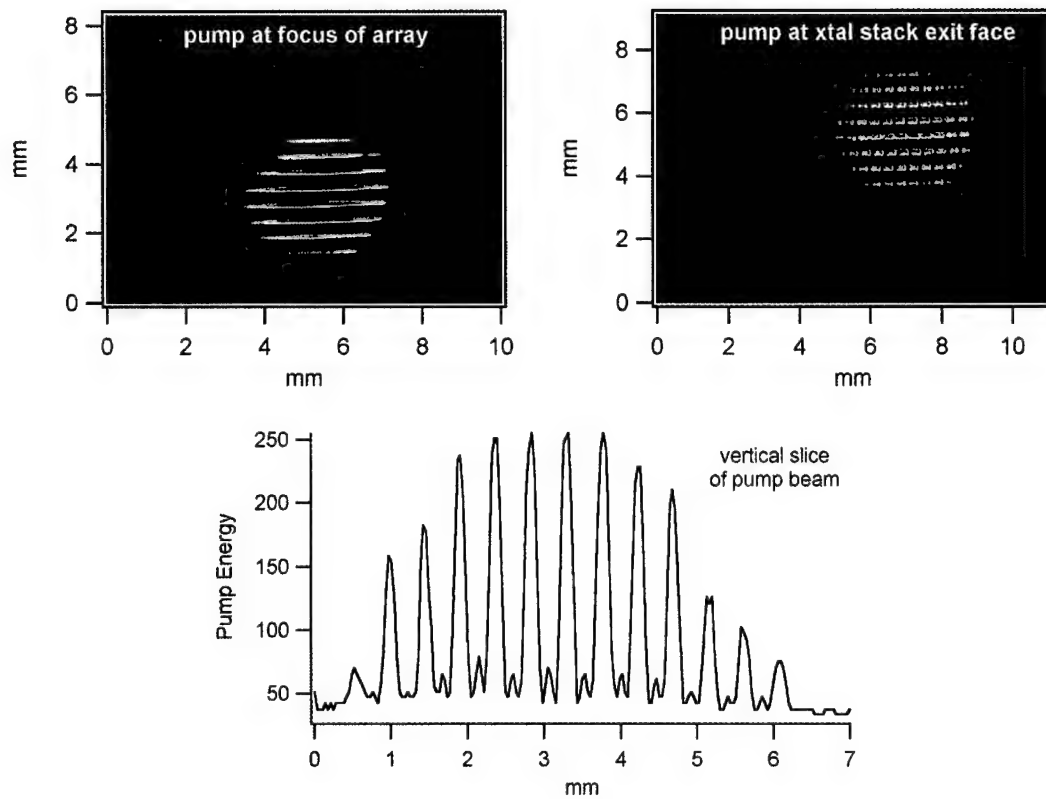


Figure 3.24 - Images from the revised setup of the pump beam at the focal plane of the cylindrical lens array (top left) and after passing through a stack of eight 1/2-mm thick crystals (top right). The bottom plot was produced by taking a vertical slice across the intensity profile in the top left image.

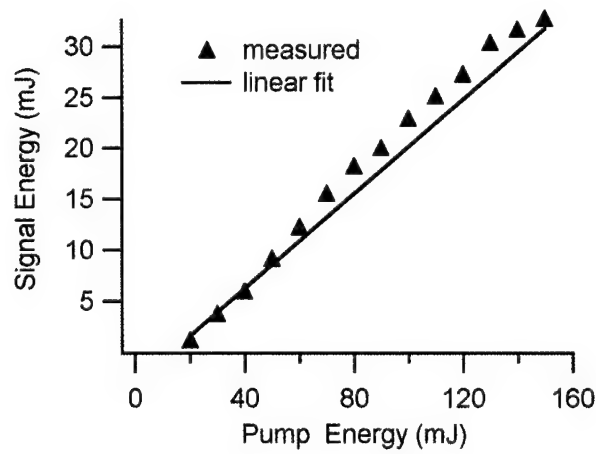


Figure 3.25 - Output signal energy versus pump energy for the PPLN stack in the revised experimental setup.

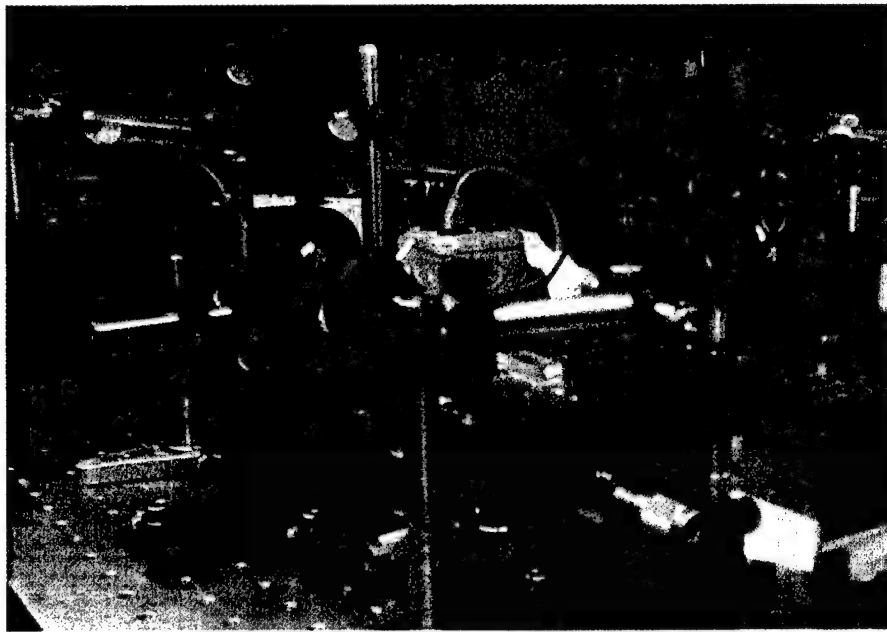


Figure 3.26 - Picture of the SFG beam at the exit face of the crystal stack. The picture was taken through a filter to eliminate green light produced by SHG of the pump.

As the pump energy was increased above 150 mJ, we observed crystal damage on both the input and exit faces of the stack (see Figure 3.27). We initially thought the crystal damage might have been caused by pump beam misalignment with respect to the crystal. However, close examination of the damage pattern on the stack indicates that the pump beam was properly aligned and the damage occurred simply due to exceeding the damage fluence for lithium niobate. We determined that the fluence at the damage point was $\sim 1.46 \text{ J/cm}^2$. Although this is approximately half of the commonly reported damage fluence of 3 J/cm^2 , our experience with previous experiments has shown that a damage fluence of 1.5 J/cm^2 is typical for lithium niobate. Our damage fluence of $\sim 1.46 \text{ J/cm}^2$ is consistent with this value.

The near and far field signal beams generated with the revised experimental setup (before crystal damage) were virtually identical to those generated by the initial setup. Near field signal images at multiple pump energy levels are presented in Figure 3.28. Although far field signal beams were examined visually to confirm that their beam quality was consistent with that observed in the previous setup, the crystal was damaged before images of the far field beams could be taken.

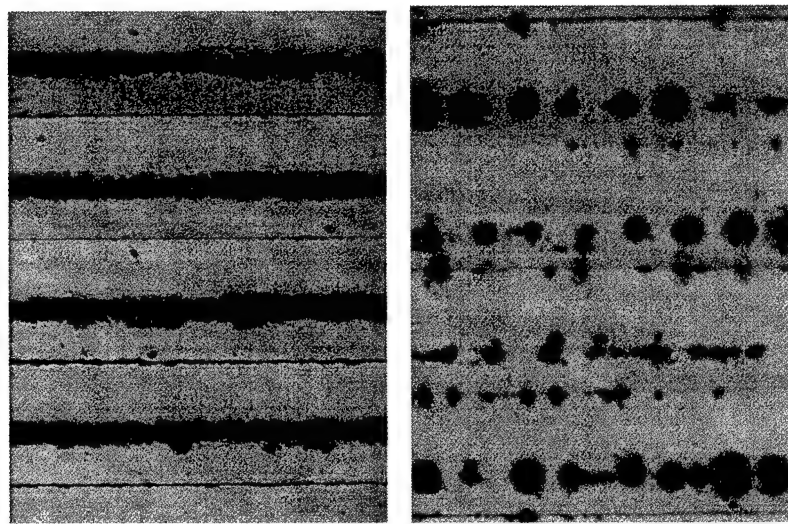


Figure 3.27 - Close-up images of the damage on the input face (left) and exit face (right) of the stack of eight 1/2-mm thick PPLN crystals.

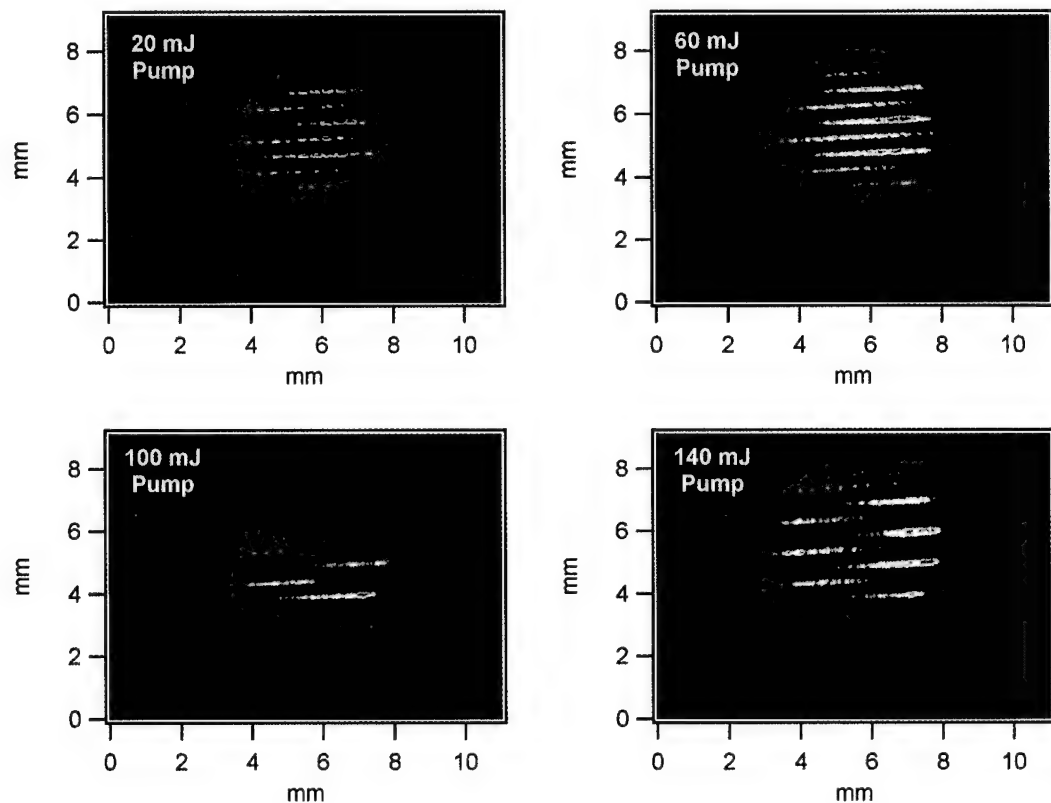


Figure 3.28 - Near field signal images generated by the stack of eight 1/2-mm thick PPLN crystals when pumped in the revised setup at various pump energies.

After the experiments with the stack of eight 0.5-mm thick segmented multi-grating crystals, we fabricated a stack of five 1-mm thick segmented multi-grating

crystals and performed similar experiments. We used the revised setup described in Figure 3.23, but added a 100-mm focal length cylindrical lens after the lens array to magnify and image the focal plane of the lens array into the 1-mm thick crystals. The magnification was 2:1 such that the elliptical beams generated by the array were spaced by 1 mm center to center. An image of the pump beam after magnification is provided in Figure 3.29.

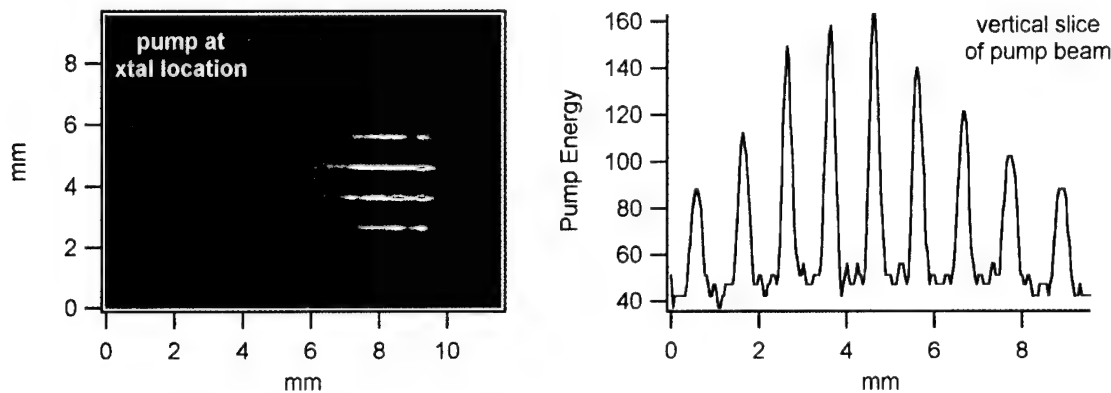


Figure 3.29 - Image of the pump beam (left) at the location in the experimental setup where the crystal stack is placed (no crystal is present in the image), and an intensity profile (right) obtained by taking a vertical slice of the pump image.

We used the pump profile of Figure 3.29 to pump the five crystal stack. The stack reached OPG threshold at \sim 30 mJ of pump energy and signal energies as high as 25 mJ were generated at higher pump energies (see Figure 3.30). We pumped the stack with up to 140 mJ of pump energy without observing crystal damage, but the crystals began to damage at pump energies above 140 mJ. The pump fluence at this energy level was only \sim 1.1 J/cm², so this set of crystals damaged at lower energies than would be expected. A close examination of the crystal endfaces showed that most of the surface damage occurred at or near the seams between crystals (see Figure 3.31). This indicates that we had the stack misaligned such that the elliptical pump beams were not passing cleanly through the crystals. This caused the pump beam to clip on the seams between crystals and led to crystal damage at lower than expected fluence levels. With proper pump beam alignment, much higher signal energies should be achievable with stacks of 1-mm crystals.

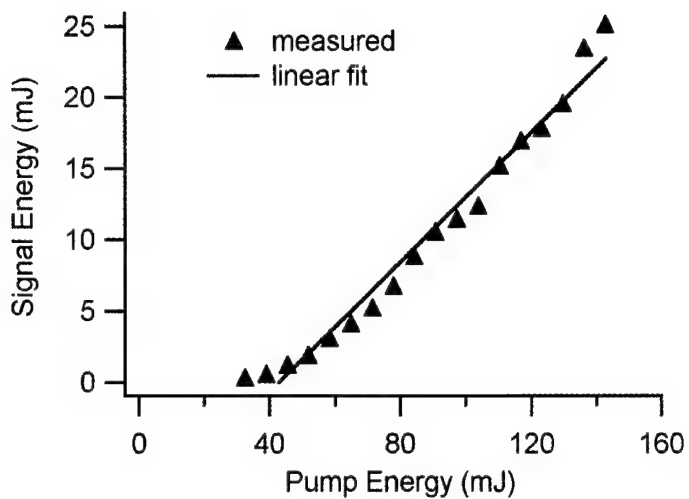


Figure 3.30 - Output signal energy versus pump energy for the stack of five 1-mm multi-grating crystals.

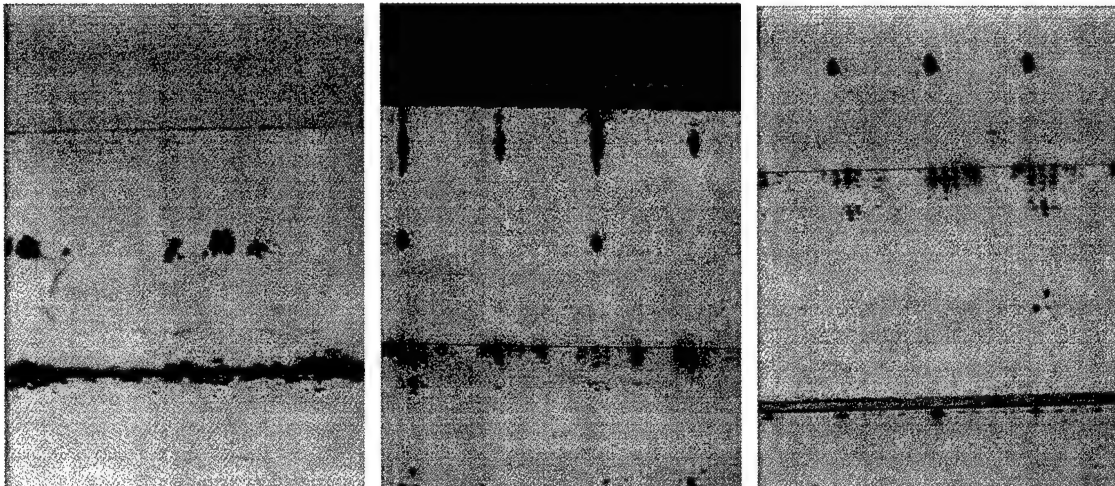


Figure 3.31 - Close-up images of the crystal damage on the input face (left) and exit face (middle and right) of the stack of five 1-mm thick PPLN crystals. The damage on the exit faces indicates that the pump beam was clipping on the seams between crystals.

We visually examined both the near and far field signal beams generated by the stack of 1-mm thick crystals and found them to be similar to those generated by the stack of 1/2-mm thick crystals. The near field beams showed signal generation in all five crystals of the stack while the far field beam quality was extremely good. Images of the near field signal beams at multiple pump energies were acquired and are presented in Figure 3.32; however, premature crystal damage again prevented us from acquiring images of the far field signal beams.

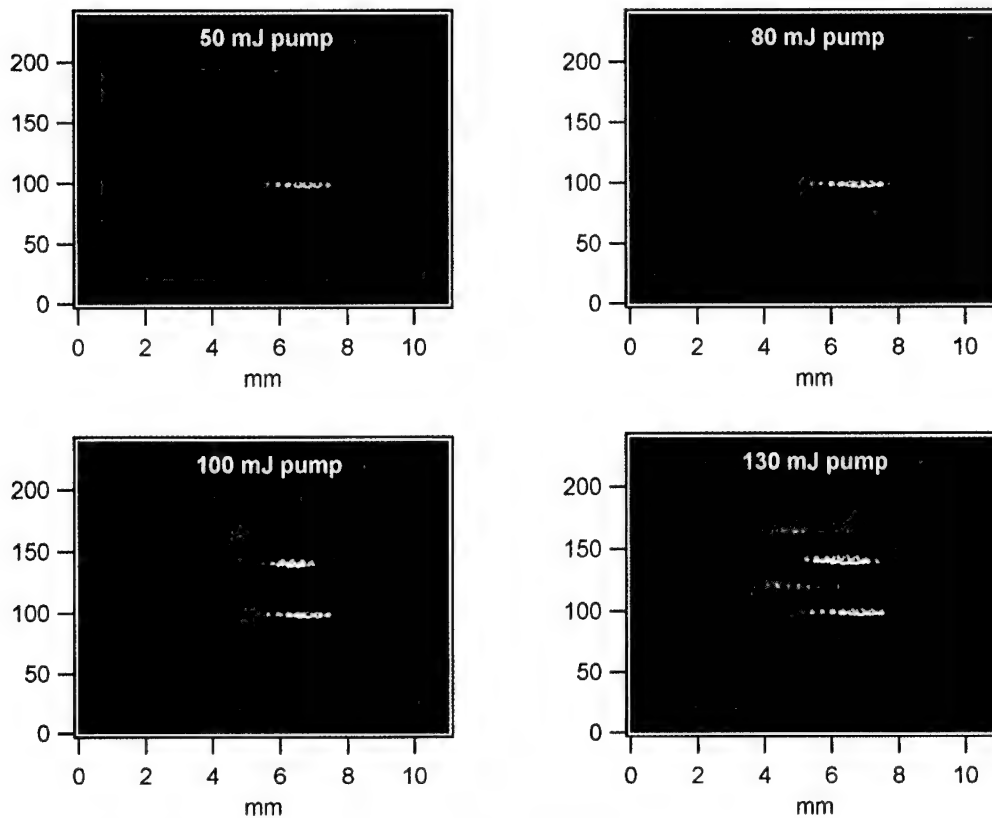


Figure 3.32 - Near field images of the signal output generated by the stack of five 1-mm thick PPLN crystals when pumped at various pump energies.

The high energies and excellent far field beam quality of the signal output generated by both PPLN stacks tested in this section demonstrate the great potential of these devices. Even more exciting is that by making some simple adjustments their performance can be greatly improved. For example, all of our experiments were performed on bare (uncoated) PPLN crystals, yet previous experiments have shown that coating the endfaces of PPLN crystals with a thin layer of SiO_2 can increase their damage threshold by a factor of 3.5.²⁷ Such coatings would theoretically allow our crystal stacks to achieve signal energies of greater than 100 mJ without any further modifications. Furthermore, we performed our experiments on stacks of eight and five crystals, but there is no reason this system can not be scaled up to include more crystals and wider (in the horizontal direction) pump beams. These modifications would also significantly increase the output signal energy without seriously degrading the far field beam quality.

3.5 Summary

In this chapter we demonstrated high-energy PPLN devices with excellent beam quality. In pursuit of the design for these devices, we first demonstrated that segmented grating crystals allow energy scaling in the transverse dimension (typically the horizontal dimension) without significant beam quality degradation or spectral broadening. We then introduced a new grating design that uses narrow poled regions leading into large uniformly poled regions to seed the parametric generation process. We found that these seeded grating crystals successfully seeded the parametric process, but their far field beams appeared to suffer from interference. Although these devices warrant further study, we chose to pursue the segmented grating crystals for our high-energy design.

We then attempted to overcome the aperture limitations of typical PPLN devices by stacking multiple segmented grating crystals and pumping them with large aperture beams. We first investigated two crystal stacking approaches consisting of simply placing them in optical contact and diffusion bonding respectively; however, the stacks produced by both of these methods suffered crystal damage at a relatively low pump energies. We then decided to bond the stacks together using a high-temperature wax and pump each crystal individually by first passing the pump beam through a cylindrical microlens array. With this method we were able to generate signal energies as high as 33 mJ using uncoated PPLN crystals. The maximum conversion efficiency attained was 46 percent and the signal beams had excellent M^2 values of 1.4 to 1.9. This system should be easily scaleable to generate signal energies in the 100 mJ range with good beam quality.

Chapter 4

PPLN-Based Source for Differential Absorption Lidar and Tunable Terahertz-Wave Generation

4.1 *Introduction*

Differential absorption lidar (DIAL) has emerged as a powerful tool for remote detection and analysis of atmospheric pollutants, chemical vapor plumes, and even general atmospheric conditions (e.g., ozone and water vapor levels). DIAL measurements are made by emitting two light beams simultaneously with one tuned to a wavelength that will be absorbed by the target particles and the other tuned to a nearby wavelength that will not be absorbed. Information about both the range and concentration of the target species can then be determined by comparing the amount of light scattered by each beam. If the two light beams are tunable, such systems can also be scanned to search for multiple chemical species. For example, Marinelli *et. al.* recently used a tunable source in the 9.5 μm to 12 μm wavelength range to demonstrate remote detection and imaging of chemical plumes.⁴⁶ The source we present in this chapter generates two narrow-band, independently tunable mid-IR (1.4 μm to 4.7 μm) wavelengths for use in similar DIAL systems.

In addition to DIAL, the source we present can be used to generate terahertz-(THz-) wave radiation. Coherent THz-waves are useful for a variety of scientific, commercial, and military applications. Functions performed by THz radiation sources include THz-wave spectroscopy, THz imaging, wireless communications, and millimeter wave radar, just to name a few. One method for generating THz-waves that has attracted a great deal of attention recently is difference frequency mixing of two laser sources in a nonlinear medium.^{47,48} In such systems, the separation between the frequencies of the two laser sources determines the frequency of the THz radiation. If one (or both) of these laser sources is tunable, then the generated THz radiation will also be tunable.

For example, Kawase *et. al.* demonstrated a tunable THz-wave source by setting up a dual signal-wave PPLN OPO and mixing the two signal output frequencies in a 4-dimethylamino-N-methyl-4-stilbazolium-tosylate (DAST) crystal.⁴⁸ The dual signal-wave OPO used a PPLN crystal with two different grating periods (in series) along the pump path. Since each grating period was phase-matched for a different signal wavelength, the system generated two distinct signal frequencies in the collinear direction. These two frequencies were then difference frequency mixed in the DAST crystal to generate THz radiation. As an added benefit, the THz-wave output could be tuned over a limited range by temperature tuning the output of the PPLN OPO to different signal wavelengths or by illuminating a different set of grating periods on the PPLN crystal (by crystal translation). The source we report in this chapter serves as a replacement for the dual signal-wave OPO discussed above, but with greatly improved tunability in terms of both range and agility.

4.2 Tunable Two-Frequency Injection-Seeded OPG

The source discussed in this section is based on the injection-seeded PPLN OPG initially developed by Powers *et. al.* for high resolution spectroscopic studies.¹⁷ As shown in Figure 4.1, in the injection-seeded OPG design the pump beam is split into two beams and used to pump two separate PPLN stages. The first stage OPG generates a broad spectral bandwidth with high efficiency. The pump and idler outputs from this stage are sent to a beam dump, and the signal is sent through a Fabry-Perot etalon to filter the output spectrum to a narrow spectral linewidth ($\sim 0.1 \text{ cm}^{-1}$). The filtered output is then co-aligned with the second pump beam (which has propagated along a delay line) and used to seed the second stage. An example of seeded versus unseeded output from the second stage is provided in the left plot of Figure 4.2. The seeded output can be tuned across the entire OPG gain bandwidth (i.e., the unseeded bandwidth) of the second stage by simply changing the mirror spacing in the etalon. Since a piezo-electric transducer drives the etalon spacing, this tuning can be accomplished very rapidly. In addition, the entire gain bandwidth, and therefore the seeded tuning range, can be shifted by changing the grating period of the PPLN crystals or by temperature tuning the crystals. However, the gain bandwidths of the first and second stages must overlap to generate seeded output.

To convert this system into a two-frequency injection-seeded OPG, we proposed adding a second tunable seed wavelength by making a simple modification to the scheme shown in Figure 4.1. In the modified system, the OPG output from the first stage was split by a 50/50 beam splitter. The two beams were passed through separate etalons, then co-aligned with a second 50/50 beam splitter before being used to seed the second stage. This provided two wavelength-independent seed sources for the second PPLN crystal, which then generated two narrow spectral lines within the overall OPG gain bandwidth (see the right plot of Figure 4.2). A schematic of this modified system is shown in Figure 4.3. Both etalons in this modified system were tunable, so we were able to rapidly change the wavelengths of, and therefore the spacing between, the two seeded lines.

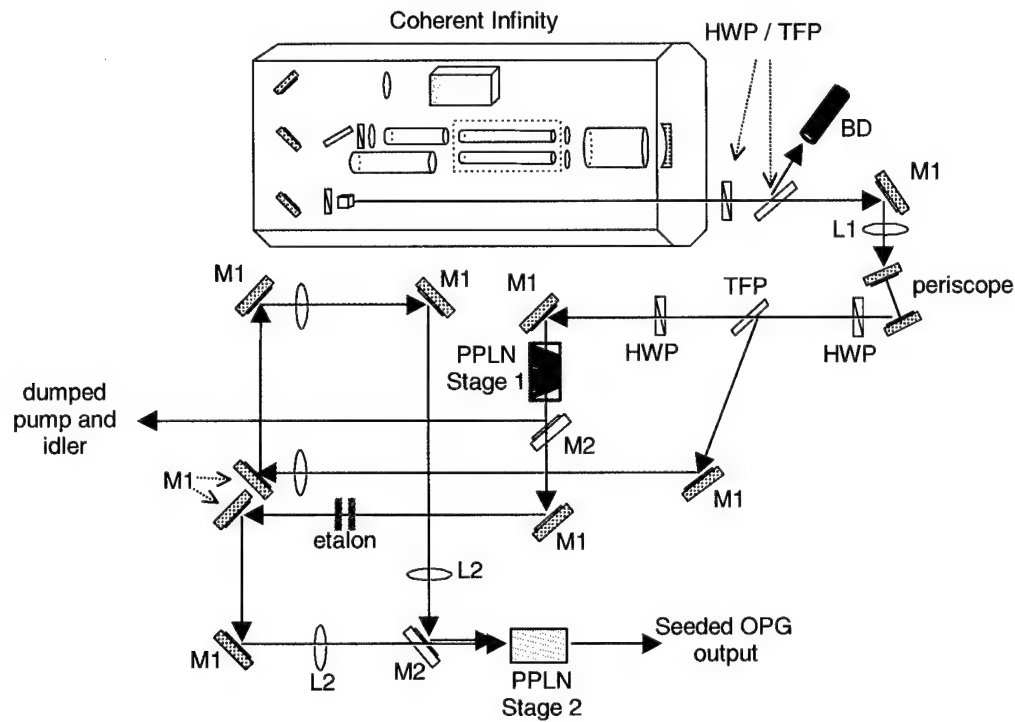


Figure 4.1 - Experimental setup for the two-stage injection-seeded OPG system. The red line denotes the pump path for the first stage and the blue line is the part of the pump beam that is split off to pump the second stage. M1 = aluminum mirror, M2 = mirror that reflects pump and idler and passes signal, HWP = half wave plate, TFP = thin film polarizer, BD = beam dump, L1 = 1000mm focal length lens, L2 = 200 mm focal length lens.

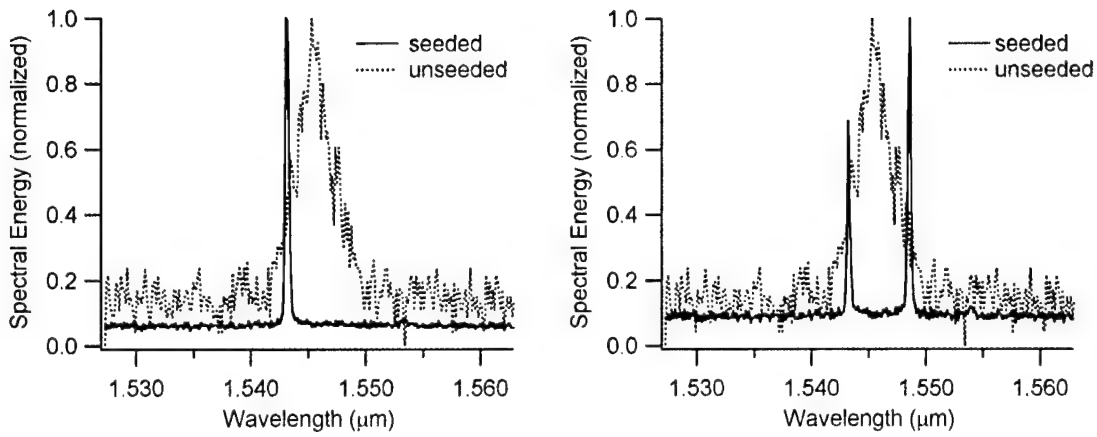


Figure 4.2 - Seeded (solid red line) and unseeded (dotted blue line) OPG output from the two-stage injection-seeded system described in Figure 4.1 (left) and the double-seeded two-stage OPG system described in Figure 4.3 (right).

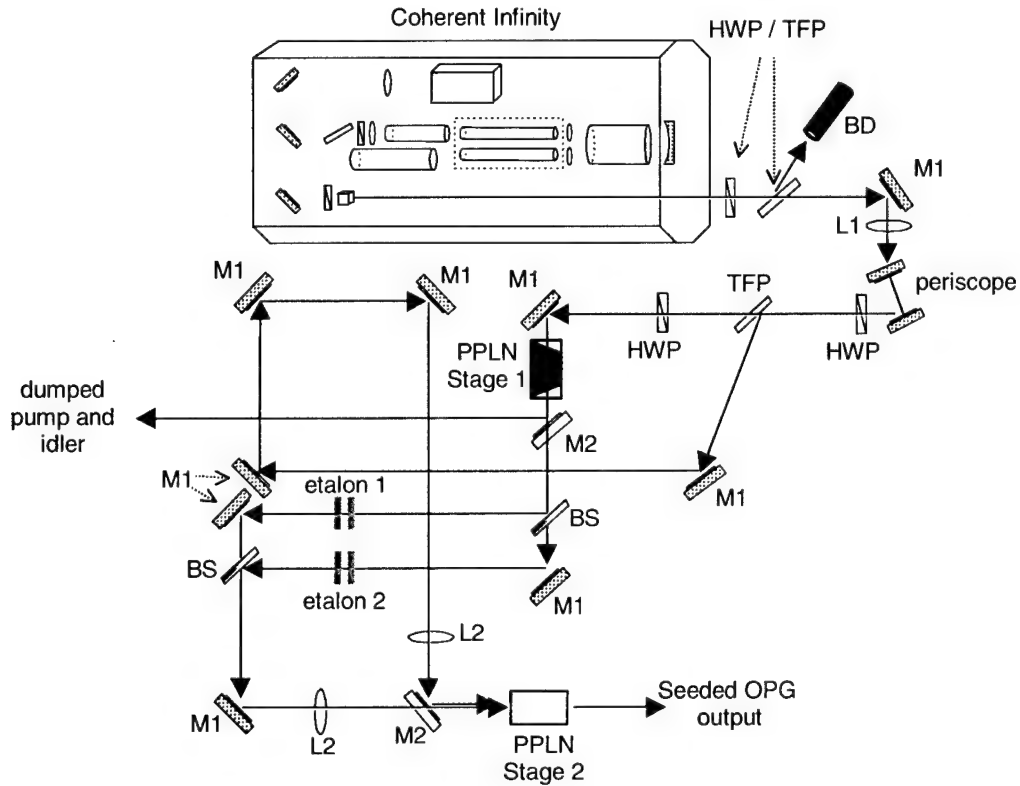


Figure 4.3 - Modified experimental setup for the double-seeded two-stage OPG system. The blue line is the part of the pump beam that is split off to pump the second stage. BS = beam splitter, M1 = aluminum mirror, M2 = mirror that reflects pump and idler and passes signal, HWP = half wave plate, TFP = thin film polarizer, BD = beam dump, L1 = 1000mm focal length lens, L2 = 200 mm focal length lens.

To ensure we could overlap the gain bandwidths of the two stages, we used a continuously tunable fan grating crystal for the first stage OPG. Then by simply translating the crystal we were able to achieve gain overlap for any PPLN OPG crystal placed in the second stage. For our initial experiments, we centered the output signal wavelengths from both stages at $1.545\text{ }\mu\text{m}$. We then demonstrated the tunability of the system by changing the mirror spacing in either etalon, or by changing them both simultaneously. The two seeded lines tuned quickly and continuously across the gain bandwidth as the mirror spacings were adjusted. The results presented in Figure 4.4 are typical of the spectral output we observed.

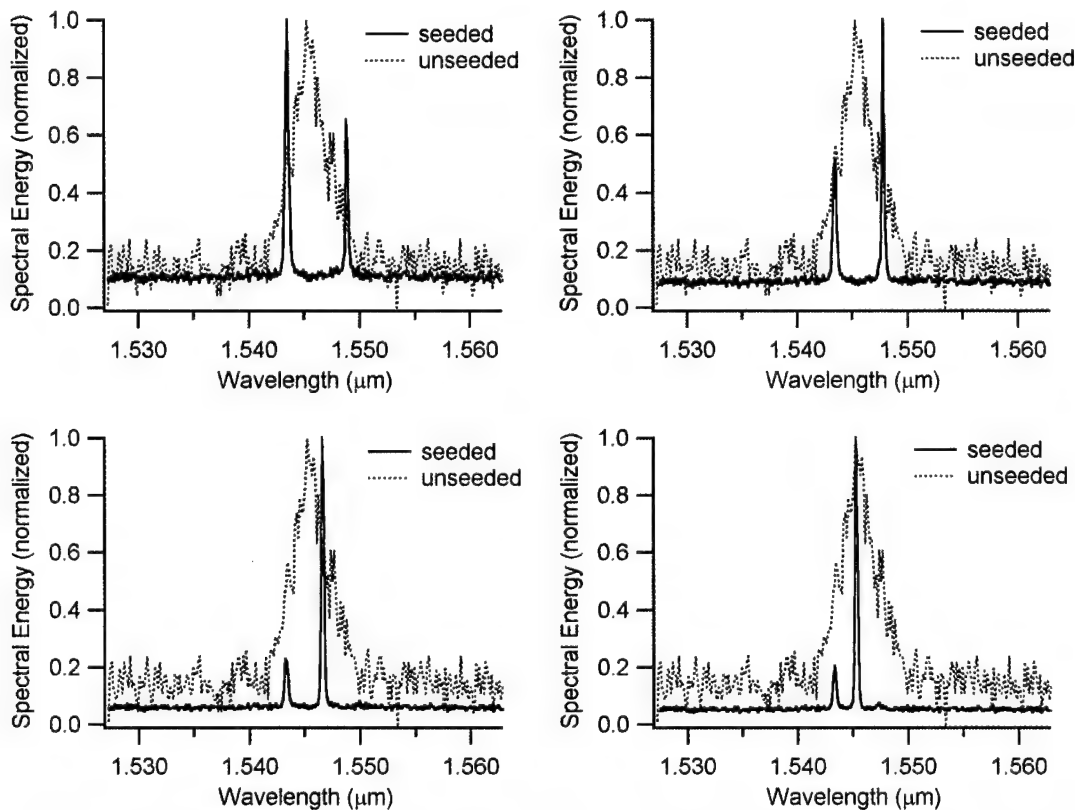


Figure 4.4 - Spectral traces of the signal output from the double-seeded OPG. The traces were taken at several intervals while the mirror spacing in one of the etalons was adjusted.

The results shown in Figure 4.4 confirm the usefulness of the two-frequency injection-seeded OPG as a source for DIAL applications. In addition, by focusing the seeded output into a proper nonlinear mixing medium (e.g., a DAST crystal), the two seeded lines can be mixed to generate tunable THz-wave radiation at their difference

frequency. With the gain bandwidth centered at 1.545 μm as shown above, we were able to tune the frequency separation of the two seeded lines from less than 100 GHz to \sim 1.1 THz. By operating the double-seeded OPG at wavelengths centered closer to degeneracy (2.128 μm for a 1.064 μm pump), the gain bandwidth can be significantly broadened. This will allow much greater frequency separation between the seeded lines, pushing the difference frequency into the higher THz regime. However, as the gain bandwidth is broadened beyond the free spectral range (FSR) of the etalons, multiple etalon orders will seed multiple lines in the second PPLN stage. This problem can be overcome by increasing the FSR of the etalons or by using two diode lasers to seed the system (the latter can be expensive, however).

The nonlinear material of choice for much of the recent work with difference frequency THz-wave generation has been DAST. DAST crystals were unavailable at the time of our experiments, so we looked for evidence of THz generation in the PPLN crystals themselves. Previous experiments have shown THz generation by difference frequency mixing in PPLN,⁴⁷ but lithium niobate strongly absorbs THz frequencies so the THz-waves were generated at a steep noncollinear angle and quickly prism-coupled out of the crystals. Since our seed beams were collinear, any THz radiation generated would be quickly absorbed as it propagated through the crystal. However, light generated by parasitic processes (e.g., poorly phase-matched SFG and DFG interactions) can often be used as an indicator of the frequency mixing processes taking place in a nonlinear medium. For example, when generating mid-IR radiation in a typical PPLN crystal pumped at 1.064 μm , a solid indication of mid-IR generation is the appearance of visible red light. The red light is generated by parasitic sum frequency mixing of the mid-IR and pump wavelengths. Similarly, we looked for parasitic indications of THz generation in our double-seeded system.

By plotting the same four sets of spectral data shown in Figure 4.4 on a log scale (see Figure 4.5), we were immediately able to see a third spectral line centered at longer wavelengths and with energy about an order of magnitude lower than that of the two primary seeder lines. We then observed that, as shown in Figure 4.5, as we tuned the separation of the two seeded lines the center wavelength of the third line tuned

accordingly. A simple calculation revealed that this third spectral line occurred at the difference frequency of the longer-wavelength seeded line and the THz radiation that would be generated by mixing of the two seeded lines. For example, the top left plot of Figure 4.5 shows the two primary seeded lines at $\lambda=1.543 \mu\text{m}$ and $\lambda=1.549 \mu\text{m}$ (frequencies of 194.4 and 193.7 THz respectively). The THz radiation generated by difference frequency mixing of these two lines occurs at a frequency of 0.7 THz. Then a parasitic difference frequency mixing of the 0.7 THz with the 194.4 THz ($\lambda=1.549 \mu\text{m}$) line would generate light at $\lambda=1.555 \mu\text{m}$. This corresponds exactly to the center wavelength of the third line observed in the plot.

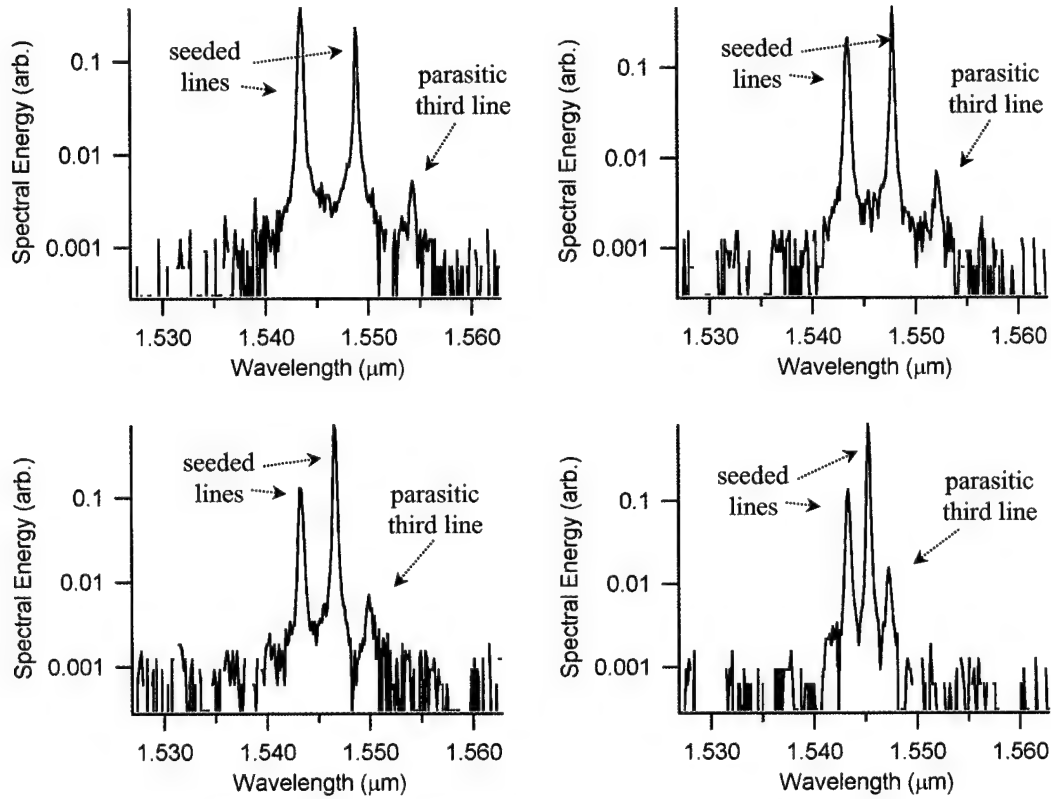


Figure 4.5 - Spectral traces of the same data displayed in Figure 4.4, but re-plotted using a log scale for the spectral energy. By plotting the data on a log scale, a third line generated by a parasitic difference frequency process with the generated THz-wave is clearly visible.

Although this parasitic difference frequency process may be evidence that THz waves were both being generated and frequency tuned in our two-frequency injection-seeded OPG, we should point out that other processes (e.g., four-wave mixing) could also be responsible for the appearance of the third spectral line. Nonetheless, this two-

frequency source is clearly suited for tunable THz-wave generation through difference frequency mixing in a proper nonlinear medium.

4.3 Summary

We have demonstrated a two-frequency injection-seeded OPG as a source for DIAL and the generation of tunable THz-wave radiation. This two-stage system divides the OPG output from the first stage into two beams, then passes each beam through a separate Fabry-Perot etalon to filter the broad OPG bandwidth to narrow spectral lines. These lines are then used to seed the OPG process in the second stage. The resulting output is two narrow spectral lines that are suitable for DIAL applications and can be difference frequency mixed in a nonlinear medium to generate THz-waves. Although an optimal nonlinear medium was unavailable for our experiments, we were able to detect possible evidence of THz-wave generation in the second PPLN stage by closely examining parasitic frequency mixing processes.

Chapter 5

Conclusions and Future Directions

This thesis has reported the design, fabrication, and demonstration of several novel quasi-phase-matched devices in periodically poled lithium niobate. In creating these devices, we addressed and overcame many of the problems that typically limit the usefulness of single-pass QPM systems. In addition, this work opens the door for a number of new research efforts.

In Chapter 1, we presented a brief review of basic QPM theory and expanded the theory to include the effects of pumping single-pass OPG devices with large aperture beams. We predicted that, when pumped with large aperture beams, such devices prefer to operate at wavelengths near degeneracy. Since typical PPLN crystals are not designed to phase-match at degeneracy in a collinear geometry, this results in preferred noncollinear signal and idler propagation directions. We also presented a theoretical method to analyze the phase-matching characteristics of 2-D QPM structures by taking the 2-D Fourier transform of the variation in the nonlinear coefficient traced out by the grating pattern. The Fourier transform generates a 2-D map of available grating vectors in Δk (wave vector mismatch) space, which can then be used to determine the phase-matching properties of signal and idler pairs for a given pump beam. The phase-matching conditions predicted by this method agree with those predicted by other techniques and are consistent with experimental results reported in the literature. Future efforts should utilize this technique to determine phase-matching characteristics for complicated 2-D structures (e.g., nonlinear photonic structures and aperiodic structures) that would be difficult to analyze using other techniques.

Chapter 2 reported the development of a high-energy, broadband mid-IR source. We used highly elliptical pump beams to pump PPLN crystals with a fan-out grating structure in both OPG and monolithic OPO configurations. The signal and idler beams generated by the monolithic fan crystals were spatially chirped in the near field and

angularly chirped in the far field. By simply placing an etalon in the beam path, we also generated broadband optical frequency combs across the signal and idler spectral bands while maintaining the same spatial and angular chirp. The devices were both simple, with no external cavity mirrors to align, and robust, able to withstand large pump energies. We also fabricated uniform grating crystals and verified that, as we predicted in Chapter 1, the phase-matching and gain characteristics of the crystals prefer noncollinear OPG operation for large aperture pump beams.

The broadband OPG source from Chapter 2 drives a number of potential future research efforts. The broad spectral bandwidth of the signal and idler beams offer the potential to explore pulse compression with such devices. The spatial chirp also offers a method to improve the M^2 values of the beam by using a diffraction grating or set of prism pairs to eliminate the chirp. In addition, the broadband OPG could be adapted for use as a source for Fourier Transform Infrared (FTIR) spectroscopy. By using the techniques presented in Chapter 3 to scale up the energy of the broadband device, it could also find use in remote sensing applications that require broadband illumination. Finally, a simple extension of this work would be investigation of seeding the device with large aperture beams at multiple wavelengths (i.e., investigation of use as a broadband amplifier).

In Chapter 3 we demonstrated high-energy PPLN devices with excellent beam quality. We overcame the traditional barriers to energy scaling in PPLN in two steps. We first demonstrated that segmented grating crystals allow aperture scaling in the transverse dimension without significant beam quality degradation or spectral broadening. We then stacked multiple crystals and used a cylindrical lens array to elliptically pump each crystal simultaneously. With this method we were able to generate extremely high signal energies with bare (uncoated) lithium niobate while maintaining good beam quality. In this chapter we also introduced a new grating design that uses narrow poled regions leading into large uniformly poled regions to seed the parametric generation process. We found that these seeded grating crystals successfully seeded the parametric process, but their far field beams appeared to suffer from interference.

The results presented in Chapter 3 drive multiple future research directions. Obvious next steps in the effort to scale to even higher signal energies include adding more crystals to the stacks, coating PPLN stacks with SiO_2 to increase the damage threshold, and pumping stacks of other periodically poled materials (e.g., PPRTA). Other pumping schemes could also be explored. For example, instead of illuminating stacked segmented grating crystals with elliptical beams, a stack of uniform grating crystals could be illuminated by a 2-D grid of circular pump beams. Finally, a detailed study of the properties of the seeded grating and segmented grating crystals is warranted. Questions to be answered include: what is the optimal spacing between seeders or segmented gratings; do the segmented single-grating crystals truly generate multiple incoherent beams and if so, why; can seeded grating crystals be designed such that the generated beams don't interfere?

In Chapter 4, we demonstrated a two-frequency injection-seeded OPG as a source for DIAL and generation of tunable THz-wave radiation. This two-stage system filters the output from the first stage to generate two narrow spectral lines, then uses these lines to seed the OPG process in the second stage. The resulting output is two narrow spectral lines that can be difference frequency mixed in a nonlinear medium to generate THz-waves. An optimal nonlinear mixing medium was unavailable for our experiments, but we were able to see evidence of THz-wave generation in the second PPLN stage by closely examining parasitic frequency mixing processes. The future direction for this setup is to acquire an appropriate nonlinear medium (e.g., a DAST crystal) and mix the two-frequency output in the medium. This system should be capable of efficiently generating narrow band, tunable coherent THz radiation.

REFERENCES

- 1 J. A. Armstrong, N. Bloembergen, J. Ducuing, and P. S. Pershan, "Interactions between light waves in a nonlinear dielectric," *Phys. Rev.* **127**, 1918 (1962).
- 2 P. A. Franken and J. F. Ward, "Optical harmonics and nonlinear phenomena," *Rev. Mod. Phys.* **35**, 23 (1963).
- 3 M. S. Piltch, C. D. Cantrell, and R. C. Sze, "Infrared second-harmonic generation in nonbirefringent cadmium telluride," *J. Appl. Phys.* **47**, 3514-3517 (1976).
- 4 A. Szilagyi, A. Hordvik, and H. Schlossberg, "A quasi-phase-matching technique for efficient optical mixing and frequency doubling," *J. Appl. Phys.* **47**, 2025-2032 (1976).
- 5 D. E. Thompson, J. D. McMullen, and D. B. Anderson, "Second-harmonic generation in GaAs 'stack of plates' using high-power CO₂ laser radiation," *Appl. Phys. Lett.* **29**, 113-115 (1976).
- 6 M. Okada, K. Takizawa, and S. Ieiri, "Second harmonic generation by periodic laminar structure of nonlinear optical crystal," *Opt. Commun.* **18**, 331 (1976).
- 7 F. Zernike and J. E. Midwinter, *Applied Nonlinear Optics*, Wiley, New York, 1973.
- 8 M. Yamada, N. Nada, M. Saitoh, and K. Watanabe, "First-order quasi-phase matched LiNbO₃ waveguide periodically poled by applying an external field for efficient blue second-harmonic generation," *Appl. Phys. Lett.* **62**, 435 (1994).
- 9 W. K. Burns, W. McElhanon, and L. Goldberg, "Second harmonic generation in field poled, quasi-phase-matched, bulk LiNbO₃," *IEEE Phot. Tech. Lett.* **6**, 252 (1994).
- 10 L. E. Myers, R. C. Eckardt, M. M. Fejer, R. L. Byer, W. R. Bosenberg, and J. W. Pierce, "Quasi-phase-matched optical parametric oscillators in bulk periodically poled LiNbO₃," *J. Opt. Soc. Am. B* **12**, 2102-2116 (1995).

¹¹ L. E. Myers, R. C. Eckardt, M. M. Fejer, R. L. Byer, and W. R. Bosenberg, "Multigrating quasi-phase-matched optical parametric oscillator in periodically poled lithium niobate," *Opt. Lett.* **21** (8), 591-593 (1996).

¹² S. Russell, M. J. Missey, P. Powers, and K. Schepler, "Periodically poled lithium niobate with a 20° fan angle for continuous OPG tuning," in Conference on Lasers and Electro-Optics, *OSA Technical Digest Series* (Optical Society of America, Washington DC, 2000), 632-633.

¹³ G. D. Miller, R. G. Batchko, W. M. Tulloch, D. R. Weise, M. M. Fejer, and R. L. Byer, "42%-efficient single-pass cw second-harmonic generation in periodically poled lithium niobate," *Opt. Lett.* **22**, 1834-1836 (1997).

¹⁴ G. W. Ross, M. Pollnau, P. G. R. Smith, W. A. Clarkson, P. E. Britton, and D. C. Hanna, "Generation of high-power blue light in periodically poled LiNbO_3 ," *Opt. Lett.* **23**, 171-173 (1998).

¹⁵ M. A. Arbore, O. Marco, and M. M. Fejer, "Pulse compression during second-harmonic generation in aperiodic quasi-phase-matching gratings," *Opt. Lett.* **22**, 865-867 (1997).

¹⁶ M. A. Arbore, A. Galvanauskas, D. Harter, M. H. Chou, and M. M. Fejer, "Engineerable compression of ultrashort pulses by use of second-harmonic generation in chirped-period-poled lithium niobate," *Opt. Lett.* **22**, 1341-1343 (1997).

¹⁷ P. E. Powers, K. W. Anolek, T. J. Kulp, B. A. Richman, and S. E. Bisson, "Periodically poled lithium niobate optical parametric amplifier seeded with the narrow-band filtered output of an optical parametric generator," *Opt. Lett.* **23**, 1886-1888 (1998).

¹⁸ A. Harada and Y. Nihei, "Bulk poled MgO-LiNbO_3 by corona discharge method," *Appl. Phys. Lett.* **69**, 2629-2631 (1996).

¹⁹ Shi-ning Zhu, Yong-yuan Zhu, Zhi-yong Zhang, Hong Shu, Hai-feng Wang, Jing-Fen Hong, Chuan-zhen Ge, and Nai-ben Ming, " LiTaO_3 crystal periodically poled by applying an external pulsed field," *J. Appl. Phys.* **77**, 5481 (1995).

²⁰ R. Stolzenberger and M. Scripsick, "Recent advancements in the periodic poling and characterization of RTA and its isomorphs," *SPIE Conference on Laser Material Crystal Growth and Nonlinear Materials and Devices*, January 1999.

²¹ H. Karlsson, F. Laurell, P. Henriksson, and G. Arvidsson, "Frequency doubling in periodically poled RbTiOAsO₄," *Electron. Lett.* **32**, 556 (1996).

²² Q. Chen and W. P. Risk, "Periodic poling of KTiOpO₄ using an applied electric field," *Electron. Lett.* **30**, 1516 (1994).

²³ S. Wang, V. Pasiskevicius, J. Hellstrom, F. Laurell, and H. Karlsson, "First-order type II quasi-phase-matched UV generation in periodically poled KTP," *Opt. Lett.* **24**, 978-980 (1999).

²⁴ J.-P. Meyn, M. E. Klein, D. Woll, and R. Wallenstein, "Periodically poled potassium niobate for second-harmonic generation at 463 nm," *Opt. Lett.* **24**, 1154-1156 (1999).

²⁵ L. A. Eyres, P. J. Tourreau, T. J. Pinguet, C. B. Ebert, J. S. Harris, M. M. Fejer, B. Gerard, L. Becouarn, and E. Lallier, "Thick (200-μm) orientation-patterned GaAs for bulk quasi-phasematched nonlinear frequency conversion," in Conference on Lasers and Electro-Optics, *OSA Technical Digest Series* (Optical Society of America, Washington DC, 2000), 630-631.

²⁶ W. R. Bosenberg, A. Drobshoff, J. I. Alexander, L. E. Myers, R. L. Byer, "93% pump depletion, 3.5-W continuous wave, singly resonant optical parametric oscillator," *Opt. Lett.* **21**, 1336-1338 (1996).

²⁷ M. J. Missey, "Characterization of periodically poled lithium niobate monolithic optical parametric oscillators and generators," Ph.D. Dissertation, University of Dayton, December 1999.

²⁸ M. M. Fejer, G. A. Magel, D. H. Jundt, and R. L. Byer, "Quasi-phase-matched second harmonic generation: tuning and tolerances," *IEEE J. Quantum Electron.* **20**, 2631-2654 (1992).

²⁹ N. G. R. Broderick, G. W. Ross, H. L. Offerhaus, D. J. Richardson, and D. C. Hanna, "Hexagonally poled lithium niobate: a two-dimensional nonlinear photonic crystal," *Phys. Rev. Lett.* **84**, 4345-4348 (2000).

³⁰ V. Berger, "Nonlinear photonic crystals," *Phys. Rev. Lett.* **81**, 4136-4139 (1998).

³¹ A. Chowdhury, S. C. Hagness, and L. McCaughan, "Simultaneous optical wavelength interchange with a two-dimensional second-order nonlinear photonic crystal," *Opt. Lett.* **25**, 832-834 (2000).

³² S. Saltiel and Y. S. Kivshar, "Phase matching in nonlinear $X^{(2)}$ photonic crystals," *Opt. Lett.* **25**, 1204-1206 (2000).

³³ R. L. Byer, "Optical parametric oscillators," in *Quantum Electronics: A Treatise*, H. Rabin and C. L. Tang, eds. (Academic, New York, 1975), 587-702.

³⁴ N. O'Brien, M. J. Missey, P. E. Powers, V. Dominic, and K. L. Schepler, "Electro-optic spectral tuning in a continuous-wave, asymmetric-duty-cycle, periodically poled LiNbO_3 optical parametric oscillator," *Opt. Lett.* **24**, 1750-1752 (1999).

³⁵ P. E. Powers, T. J. Kulp, and S. E. Bisson, "Continuous tuning of a continuous-wave periodically poled lithium niobate optical parametric oscillator by use of a fan-out grating design," *Opt. Lett.* **23**, 159-161 (1998).

³⁶ M. Missey, S. Russell, V. Dominic, R. Batchko, and K. L. Schepler. (2000, May 8) "Real-time visualization of domain formation in periodically poled lithium niobate." *Optics Express* [Online]. **6**(10), 186-195. Available: www.opticsexpress.org

³⁷ P. E. Powers, T. J. Kulp, and S. E. Bisson, "Continuous tuning of a continuous-wave periodically poled lithium niobate optical parametric oscillator by use of a fan-out grating design," *Opt. Lett.* **23**, 159-161 (1998).

³⁸ L. E. Myers, "Quasi-phased matched optical parametric oscillators in bulk periodically poled lithium niobate," Ph.D. Dissertation, Stanford University, December 1995, 64-74.

³⁹ R. Urschel, U. Bäder, A. Borsutzky, and R. Wallenstein, "Spectral properties and conversion efficiency of 355-nm-pumped pulsed optical parametric oscillators of β -barium borate with noncollinear phase matching," *J. Opt. Soc. Am. B* **16**, 565 (1999).

⁴⁰ The high-resolution transmission (HITRAN) molecular absorption database, Available: www.hitran.com.

⁴¹ M. J. Missey, V. G. Dominic, P. E. Powers, K. L. Schepler, "Elliptical energy scaling with monolithic PPLN OPOs," *Proc. SPIE* Vol. 3928, 16-24 (2000).

⁴² M. Missey, V. Dominic, L. E. Myers, and R. C. Eckardt, "Diffusion-bonded stacks of periodically poled lithium niobate," *Opt. Lett.* **23**, 664-666 (1998).

43 H. Karlsson, M. Olson, G. Arvidsson, F. Laurell, U. Bäder, A. Borsutzky, R. Wallenstein, S. Wickström, and M. Gustafsson, "Nanosecond optical parametric oscillator based on large-aperture periodically poled RbTiOAsO₄," *Opt. Lett.* **24**, 330-332 (1999).

44 J. Hellstrom, V. Pasiskevicius, H. Karlsson, and F. Laurell, "High-power optical parametric oscillation in large-aperture periodically poled KTiOPO₄," *Opt. Lett.* **25**, 174-176 (2000).

45 M. J. Missey, V. Dominic, P. E. Powers, K. L. Schepler, "Aperture scaling effects in periodically poled lithium niobate monolithic optical parametric oscillators and generators," *Opt. Lett.* **24**, 1227-1229 (1999).

46 W. J. Marinelli, C. M. Gittins, A. H. Gelb, B. D. Green, "A Tunable Fabry-Perot Etalon-Based Long-Wavelength Infrared Imaging Spectroradiometer," *Applied Optics* **38**, 2594-2604 (2000).

47 J. Shikata, K. Kawase, K. Karino, T. Taniuchi, and H. Ito, "Tunable Terahertz-wave Parametric Oscillators Using LiNbO₃ and MgO: LiNbO₃ Crystals," *IEEE Transactions on Microwave Theory and Techniques* **48**, 653-661 (2000).

48 K. Kawase, T. Hatanaka, H. Takahashi, K. Nakamura, T. Taniuchi, and H. Ito, "Tunable terahertz-wave generation from DAST crystal by dual signal-wave parametric oscillation of periodically poled lithium niobate," *Opt. Lett.* **25**, 1714-1716 (2000).